ISSN 0021-3438 (Print)
ISSN 2412-8783 (Online)

IZVESTIYA
NON-FERROUS METALLURGY

Vol. 29, No. 3, 2023

Scientific and Technical Journal
Founded in 1958
6 Issues per year

ИЗВЕСТИЯ ВУЗОВ
ЦВЕТНАЯ МЕТАЛЛУРГИЯ

Том 29, № 3, 2023

Научно-технический журнал
Основан в 1958 г.
Выходит 6 раз в год

ISSN 0021-3438 (Print)
ISSN 2412-8783 (Online)

IZVESTIYA NON-FERROUS METALLURGY

Vol. 29, No. 3
2023

Scientific and Technical Journal Founded in 1958 6 Issues per year http://cvmet.misis.ru

Journal is included into the List of the peer-reviewed scientific publications recommended by the Highest Attestation Commission of the Ministry of Education and Science of the Russian Federation for publishing the results of doctoral and candidate dissertations

Abstracting/Indexing: Russian Science Citation Index (RSCI), Chemical Abstracts (Online), INIS, OCLC ArticleFirst, Ulrich's Periodicals Directory, VINITI Database (Abstract Journal)

Founder

National University of Science and Technology "MISIS"
Address: 4 build. 1 Leninskiy Prosp., Moscow 119049, Russia
http://www.misis.ru

Editor-in-Chief

Evgeny A. Levashov
Prof., Dr. Sci. (Eng.), Acad. of the RANS, NUST MISIS, Moscow, Russia

Deputy Editor

Vladislava A. Ignatkina
Prof., Dr. Sci., NUST MISIS, Moscow, Russia

Editorial Board

Abhilash – Dr., Ph.D., CSIR – National Metallurgical Laboratory, Jamshedpur, India
E.V. Ageev – Prof., Dr. Sci. (Eng.), SouthWest State University, Kursk, Russia
M.V. Ananyev – Prof., Dr. Sci. (Chem.), Federal State Research and Development Institute of Rare Metal Industry (JSC "Giredmet"), Moscow, Russia
N.A. Belov – Prof., Dr. Sci. (Eng.), NUST MISIS, Moscow, Russia
E.V. Bogatyreva – Prof., Dr. Sci. (Eng.), NUST MISIS, Moscow, Russia
V.B. Deev – Prof., Dr. Sci. (Eng.), NUST MISIS, Moscow, Russia
V.M. Denisov – Prof., Dr. Sci. (Chem.), Siberian Federal University, Krasnoyarsk, Russia
D.V. Drobot – Prof., Dr. Sci. (Chem.), Russian Technological University (MITHT), Moscow, Russia
F.V. Grechnikov – Prof., Dr. Sci. (Eng.), Acad. of RAS, Samara National Research University n.a. S.P. Korolev (Samara University), Samara, Russia
D.V. Gunderov – Dr. Sci. (Phys.-Math.), Institute of Molecule and Crystal Physics Ufa Research Center of the RAS, Ufa, Russia
B.B. Khina – Dr. Sci. (Phys.-Math.), The Physical-Techical Institute of NAS of Belarus, Minsk, Belarus
D.V. Louzguine – Prof., Dr. Sci., Tohoku University, Japan
S.V. Mamyachenkov – Prof., Dr. Sci. (Eng.), Ural Federal University, Yekaterinburg, Russia
Z.A. Mansurov – Dr. Sci. (Chem.), Prof., Institute of Combustion Problems, Almaty, Kazakhstan
N.V. Nemchinova – Prof., Dr. Sci. (Eng.), Irkutsk National Research Technical University, Irkutsk, Russia
K.V. Nikitin – Prof., Dr. Sci. (Eng.), Samara State Technical University, Samara, Russia
H.A. Oye – Prof., Dr., Norwegian University of Science and Technology, Trondheim, Norway
P.V. Polyakov – Prof., Dr. Sci. (Chem.), Siberian Federal University, Krasnoyarsk, Russia
E.S. Prusov – Cand. Sci. (Eng.), Vladimir State University, Vladimir, Russia
V.N. Richkov – Prof., Dr. Sci. (Chem.), Ural Federal University, Ekaterinburg, Russia
D. Sadoway – Prof., Dr., Massachusetts Institute of Technology, Boston, USA
G.A. Salishchev – Prof., Dr. Sci. (Eng.), Belgorod National Research University, Belgorod, Russia
D.V. Shtansky – Prof., Dr. Sci. (Phys.-Math.), NUST MISIS, Moscow, Russia
V.M. Sizyakov – Prof., Dr. Sci. (Eng.), Saint-Petersburg Mining University, St. Petersburg, Russia
Stopic Srecko – Dr.-Ing. habil., RWTH Aachen University, Aachen, Germany
B.B. Straumal – Prof., Dr. Sci. (Phys.-Math.), Institute of Solid State Physics of the RAS, Chernogolovka, Moscow region
O.Yu. Tkacheva – Dr. Sci. (Chem.), Institute of High Temperature Electrochemistry of the Ural Branch of the RAS, Yekaterinburg, Russia
M. Verhaege – Prof., Dr., University of Gent, Belgium
G.M. Vol'dman – Prof., Dr. Sci. (Chem.), Russian Technological University (MITHT), Moscow, Russia
G. Xanthopoulou – Dr., National Center for Scientific Research "Demokritos", Agia Paraskevi, Attica, Greece
A.L. Yerokhin – Prof., Dr., University of Manchester, United Kingdom
Onuralp Yücel – Prof., Dr., Istanbul Technical University, Maslak, Istanbul, Turkey
Yu.P. Zaikov – Prof., Dr. Sci. (Chem.), Institute of High Temperature Electrochemistry of the Ural Branch of the RAS, Yekaterinburg, Russia
R.Kh. Zalavutdinov – Cand. Sci. (Phys.-Math.), A.N. Frumkin Institute of Physical Chemistry and Electrochemistry of the RAS, Moscow, Russia
M. Zinigrad – Prof., Dr., Ariel University, Ariel, Israel
A.I. Zouboulis – Prof., Dr., Aristotle University of Thessaloniki, Greece

Editorial Staff

Address: NUST MISIS, 4 build. 1 Leninskiy Prosp.,
Moscow 119049, Russia
Phone: +7 (495) 638-45-35
E-mail: izv.vuz@misis.ru

Certificate of registration No. 015842 (13.03.1997)
Re-registration PI No. ФС77-79229 (25.09.2020)

Subscription: Ural-Press Agency

© NUST MISIS, Moscow, 2023
© Izvestiya. Non-Ferrous Metallurgy, 2023

Leading Editor – A.A. Kudinova
Executive Editor – O.V. Sosnina
Layout Designer – E.A. Legkaya

Signed print 14.06.2023. Format 60×90 1/8.
Offset paper No. 1. Digital printing. Quires 11
Order 17588. Free price

Printed in the printing house of the MISIS Publish House
4 build. 1 Leninskiy Prosp., Moscow 119049, Russia. Phone/fax: +7 (499) 236-76-17

Articles are available under Creative Commons Attribution Non-Commercial No Derivatives

ИЗВЕСТИЯ ВУЗОВ

ISSN 0021-3438 (Print)
ISSN 2412-8783 (Online)

ЦВЕТНАЯ МЕТАЛЛУРГИЯ

Том 29, № 3
2023

Научно-технический журнал   Основан в 1958 г.   Выходит 6 раз в год   http://cvmet.misis.ru

Журнал включен в Перечень рецензируемых научных изданий, рекомендованных ВАК Минобрнауки РФ
для публикации результатов диссертаций на соискание ученых степеней

Журнал включен в базы данных: Russian Science Citation Index (RSCI), Chemical Abstracts (Online), INIS, OCLC ArticleFirst,
Ulrich's Periodicals Directory, РИНЦ, БД/РЖ ВИНИТИ

Учредитель

ФГАОУ ВО Национальный исследовательский технологический университет «МИСИС»
Адрес: 119049, г. Москва, Ленинский пр-т, 4, стр. 1
http://www.misis.ru

Главный редактор

Евгений Александрович Левашов
д.т.н., академик РАЕН, профессор, НИТУ МИСИС, г. Москва

Заместитель главного редактора

Владислава Анатольевна Игнаткина
д.т.н., профессор, НИТУ МИСИС, г. Москва

Редакционная коллегия

Е.В. Агеев – д.т.н., ЮЗГУ, г. Курск
М.В. Ананьев – д.х.н., АО «Гиредмет», г. Москва
Н.А. Белов – д.т.н., проф., НИТУ МИСИС, г. Москва
Е.В. Богатырева – д.т.н., НИТУ МИСИС, г. Москва
Г.М. Вольдман – д.х.н., проф., РТУ (МИТХТ), г. Москва
Ф.В. Гречников – д.т.н., акад. РАН, проф., СНИУ, г. Самара
Д.В. Гундеров – д.ф.-м.н., ИФМК УНЦ РАН, г. Уфа
В.Б. Деев – д.т.н., проф., НИТУ МИСИС, г. Москва
В.М. Денисов – д.х.н., проф., СФУ, г. Красноярск
Д.В. Дробот – д.х.н., проф., РТУ (МИТХТ), г. Москва
Ю.П. Зайков – д.х.н., проф., ИВТЭ УрО РАН, г. Екатеринбург
Р.Х. Залавутдинов – к.ф.-м.н., ИФХЭ РАН, г. Москва
С.В. Мамяченков – д.т.н., проф., УрФУ, г. Екатеринбург
З.А. Мансуров – д.х.н., проф., Институт проблем горения, г. Алматы, Казахстан
Н.В. Немчинова – д.т.н., проф., ИРНИТУ, г. Иркутск
К.В. Никитин – д.т.н., проф., СамГТУ, г. Самара
П.В. Поляков – д.х.н., проф., СФУ, г. Красноярск
Е.С. Прусов – к.т.н., доцент, ВлГУ, г. Владимир
В.Н. Рычков – д.х.н., проф., УрФУ, г. Екатеринбург
Г.А. Салищев – д.т.н., проф., НИУ «БелГУ», г. Белгород
В.М. Сизяков – д.т.н., проф., СПГУ, г. Санкт-Петербург
Б.Б. Страумал – д.ф.-м.н., проф., ИФТТ РАН, г. Черноголовка
О.Ю. Ткачева – д.х.н., ИВТЭ УрО РАН, г. Екатеринбург
Б.Б. Хина – д.ф.-м.н., доц., ФТИ НАН Беларуси, г. Минск, Беларусь
Д.В. Штанский – д.ф.-м.н., проф., НИТУ МИСИС, г. Москва
Abhilash – Dr., Ph.D., CSIR – National Metallurgical Laboratory, Jamshedpur, India
D.V. Louzguine – Prof., Dr., Tohoku University, Japan
H.A. Oye – Prof., Dr., Norwegian University of Science and Technology, Trondheim, Norway
D. Sadoway – Prof., Dr., Massachusetts Institute of Technology, Boston, USA
Stopic Srecko – Dr.-Ing. habil., RWTH Aachen University, Aachen, Germany
M. Verhaege – Prof., Dr., University of Gent, Belgium
G. Xanthopoulou – Dr., National Center for Scientific Research «Demokritos», Agia Paraskevi, Attica, Greece
A.L. Yerokhin – Prof., Dr., University of Manchester, United Kingdom
Yücel Onuralp – Prof., Dr., Istanbul Technical University, Maslak, Istanbul, Turkey
M. Zinigrad – Prof., Dr., Ariel University, Ariel, Israel
A.I. Zouboulis – Prof., Dr., Aristotle University of Thessaloniki, Greece

Редакция журнала

Адрес: 119049, г. Москва, Ленинский пр-т, 4, стр. 1,
НИТУ МИСИС
Тел.: +7 (495) 638-45-35
E-mail: izv.vuz@misis.ru

Свидетельство о регистрации № 015842 от 13.03.1997 г.
Перерегистрация ПИ № ФС77-79229 от 25.09.2020 г.

Подписка: Агентство «Урал-пресс»

Ведущий редактор – А.А. Кудинова
Выпускающий редактор – О.В. Соснина
Дизайн и верстка – Е.А. Легкая

Подписано в печать 14.06.2023. Формат 60×90 1/8.
Бум. офсетная № 1. Печать цифровая. Усл. печ. л. 11
Заказ 17588. Цена свободная

Отпечатано в типографии Издательского Дома МИСИС
119049, г. Москва, Ленинский пр-т, 4, стр. 1. Тел./факс: +7 (499) 236-76-17

© НИТУ МИСИС, Москва, 2023
© «Известия вузов. Цветная металлургия», 2023

Статьи доступны под лицензией Creative Commons
Attribution Non-Commercial No Derivatives

CONTENTS

Metallurgy of Nonferrous Metals

Metallurgy of Rare and Precious Metals

Foundry

Pressure Treatment of Metals

СОДЕРЖАНИЕ

Металлургия цветных металлов

Металлургия редких и благородных металлов

Литейное производство

Обработка металлов давлением

METALLURGY OF NONFERROUS METALS / МЕТАЛЛУРГИЯ ЦВЕТНЫХ МЕТАЛЛОВ

UDC 54.084
https://doi.org/10.17073/0021-3438-2023-3-5-16

Research article
Научная статья

Improvement of monitoring and control system for copper electrolytic refining parameters

Nguyen Huy Hoang, V.Yu. Bazhin

Saint Petersburg Mining University
2, 21st Line, St. Petersburg, 199106, Russia

✉ Vladimir Yu. Bazhin (bazhin-alfoil@mail.ru)

Abstract: The utilization of modern automated control systems in copper cathode production offers the opportunity for remote access to control and regulate the electrolytic process parameters. This, in turn, enhances production efficiency while reducing energy costs. The significant parameters in copper electrolytic refining encompass the temperature and composition of the electrolyte, the circulation rate of the electrolyte, the level of sludge, and the frequency of short circuits occurring between the electrodes and the current density. These parameters directly impact the quantity and volume of cathode sludge. The occurrence of short circuits within the bath arises from the growth of dendrites, necessitating the monitoring of voltage, composition, and temperature of the electrolyte. Regular analysis of the electrolyte's composition and the accumulation of sludge volume at the bottom of the electrolyzer is also necessary. The intensification of the electrolysis process primarily involves increasing the current density, reducing the electrode spacing, enhancing the quality of electrodes, improving the electrolyte circulation system, and further mechanizing and automating the process and its auxiliary operations. These efforts contribute to increased productivity. The objective of this study is to expand the capabilities of automated process control systems by incorporating sludge level control sensors. This aims to mitigate irrecoverable losses resulting from dendritic sludge short circuits on the electrodes located in the lower section of the electrolyzer, utilizing new software. A sludge level control method to prevent short circuits has been investigated, and control software employing float-type level sensors has been developed. This measure is projected to decrease energy consumption by 15—20 % and can be effectively implemented in the production of electrolytic copper at the copper smelting plant in Lao Cai, Vietnam.

Key words: copper cathode, sludge sediment, electrodes, short circuit, sensor, electrolyte, control system, electrolytic refining.

For citation: Nguyen Huy Hoang, Bazhin V.Yu. Improvement of monitoring and control system for copper electrolytic refining parameters. *Izvestiya. Non-Ferrous Metallurgy.* 2023;29(3):5—16. https://doi.org/10.17073/0021-3438-2023-3-5-16

Совершенствование системы контроля и управления параметрами электролитического рафинирования меди

Нгуен Хю Хоанг, В.Ю. Бажин

Санкт-Петербургский горный университет
199106, Россия, г. Санкт-Петербург, Васильевский остров, 21 линия, 2

✉ Владимир Юрьевич Бажин (bazhin-alfoil@mail.ru)

Аннотация: Использование современных автоматизированных систем управления в производстве катодной меди обеспечивает возможность удаленного доступа к ресурсам для контроля и регулирования параметрами электролитического процесса, что определяет показатели эффективности производства при снижении энергетических затрат. Важными параметрами в электролитическом рафинировании меди являются температура и состав электролита, скорость его циркуляции, уровень шлама, частота замыканий между электродами и плотность тока, которые напрямую влияют на количество и объем катодного осадка. Наличие коротких замыканий на ванне обуславливается ростом дендритов, что влечет за собой необходимость контролировать напряжение, состав и температуру электролита и периодически анализировать состав и накопление объема шламового осадка на дне электролизера. Интенсификация процесса электролиза происходит в основном за счет повышения плотности тока, снижения межэлектродного расстояния, улучшения качества электродов, совершенствования системы циркуляции электролита при дальнейшей механизации и автоматизации самого процесса и его вспомогательных операций, ведущих к повышению производительности. Целью данной работы являлось расширение функций автоматизированных систем управления технологическими процессами (АСУ ТП) за счет внедрения датчиков контроля уровня шламового осадка для снижения безвозвратных потерь при наличии замыканий дендритного осадка на электроды в нижней донной части электролизера с использованием нового программного обеспечения. Рассмотрен способ контроля уровня шламового осадка для предотвращения коротких замыканий и разработана программа контроля при помощи датчиков уровня поплавкового типа. Данное мероприятие при внедрении позволит снизить расход электроэнергии на 15–20 %, что может быть полезным для внедрения в цехах электролитического производства меди на предприятии «Медеплавильный завод» (г. Лаокай, Социалистическая Республика Вьетнам).

Ключевые слова: катодная медь, шламовый осадок, электроды, замыкание, датчик, электролит, система контроля, электролитическое рафинирование.

Для цитирования: Нгуен Хю Хоанг, Бажин В.Ю. Совершенствование системы контроля и управления параметрами электролитического рафинирования меди. *Известия вузов. Цветная металлургия*. 2023;29(3):5–16.
https://doi.org/10.17073/0021-3438-2023-3-5-16

Introduction

Improving the efficiency of energy-intensive metallurgical production is of paramount importance for the further development of sustainable mineral resource operation. On the other hand, excessive fascination with new digital transformation techniques can only complicate the objectives of energy efficiency of large-capacity production [1; 2].

An analysis of the existing monitoring and control systems used at copper cathode production facilities indicates the insufficiency of the number of adjustable parameters for the stable operation of electrolyzers [3—5]. In order to achieve more effective control of the production process, new functional control points with additional sensors must be introduced. To some extent, this applies to the existing copper cathode production facilities, such as copper electrolytic production at the copper smelting plant (Lao Cai, Socialist Republic of Vietnam) [6; 7].

As part of the work performed, the problems of expanding the functional properties of the automated process control system (APCS) need to be addressed, and appropriate adjustments made to the database (DB) blocks. These blocks are produced by mathematical models to control and optimize processes associated with the formation of sludge in the lower part of an electrolytic cell. In this case, unit for matching indicators of the temperature sensor, electrolyte level controller and float regulator needs to be installed, taking into account their mutual influence. The objective is to compare the data obtained with standard parameters, in order to identify anomalies in the process. The aim of the solution is to adjust additional devices within the existing parameterization, in order to achieve optimum process conditions. In particular, a function for early detection of electrode short-circuiting due to various types of disturbances is needed, in order to warn the operator of any deviation in time. It will also facilitate faster data processing for a subsequent control action aimed at the destruction and elimination of local dendrite accretion places, taking into account their volume and number in the lower part of the bath. As the sludge level increases due to the sludge particles infiltrating the interelectrode distance, the electrolyte concentration changes.

This work will address the problems of expanding APCS functions by installing sludge level control sensors, in order to reduce irretrievable losses by reducing the number of dendritic sludge short-circuits on electrodes in the bottom part of the electrolyzer, as well as installing an additional electrolyte composition control sensor.

Adjustable process parameters of copper electrolytic refining

Copper electrolytic production is a physicochemical process functioning at a large array of adjustable parameters which the process depends on. It can be characterized by a significant number of hidden parameters which affect the course of electrochemical processes with the existing problems of adequate identification of different process stages [8—10]. The main input parameters of this process include primarily: the content of copper ions in the electrolyte; concentration of sulfuric acid; and their correspondence to the output parameters — determining productivity and current efficiency [11—13]. Thus, the efficiency of electrolytic refining of copper largely depends on the condition of electrolyzers (baths) with respect to sludge formation in the upper and lower parts of the electrodes. While dendritic short-circuits in the upper part of the cell can be seen and recorded through a thermal imaging camera, deposits on electrodes in the lower part of the bath represent a kind of "blackbox".

During the process, the current changes of the following parameters need to be monitored and analyzed (taking into account additional control conditions in the standard APCS) in the whole volume of the electrolytic cell [14—16]:

1) chemical analysis of the copper content in the electrolyte and sulfuric acid;

2) current electrolyte temperature;

3) electrolyte circulation rate;

4) current intensity on the series;

5) current density on the electrodes;

6) voltage of the electrolysis cell;

7) sludge level under control through a float-type submersible sensor;

8) concentration of chloride-ion in the electrolyte;

9) steam pressure and flow rate;

10) transfer and transportation of a part of the working electrolyte to the drain;

11) mixing of electrolyte after several circulation periods via feed and reserve tanks;

12) continuous estimated dosing of sulfuric acid and copper sulfate additives through batchers;

13) dilution and change of electrolyte concentration with spent flushing water and condensate when sulfuric acid is added to electrolyte;

14) cathodic current density;

15) loading and setting of anodes after a given period and time of their dissolution as a result of electrolysis.

In addition, the analysis of the interrelation between all operating parameters is necessary, in order to establish the necessity to specify and enter additional data such as the copper ions content and electrolyte and sludge level.

All production control and monitoring systems need to take into account the input process parameters which provide a high quality and purity of the output product — copper cathode. During electrolytic refining of copper, there are no functional relations between the amount of the formed sludge on electrodes and the sludge on the bottom of the bath — with the amount and volume of dendritic accretions and short-circuits on the electrodes, especially after their destruction. This can lead to a change in the electrolyte concentration in the bath. Known works [17—19] suggest many ways of determining he input parameter values for sustainable control of the electrolysis process, but mostly using current plant data (DB) [20—22].

In the course of the work, mathematical models were obtained for several process scenarios at different stages of the process during sludge formation at the bottom of the electrolysis cell.

Scenario 1 — formation of accretion in the lower part of the electrodes. This mechanism is related to the ingress of individual sludge particles to the lower part of the electrode surface at the uncontrolled height of the sludge when the dendritic accretion in the upper part of the cathode is destroyed. The "roiling" of the electrolyte causes changes in the electrolyte content, especially in the lower part of the bath.

Scenario 2 — rise of the upper layers of the sludge to the anode and cathode surface with the formation of accretions between the electrodes. The reason lies in the high turbulence of the electrolyte and the sludge itself.

Scenario 3 — complete short circuit between the electrodes when the sludge touches their lower parts. The reason is that the height of the sludge layer in the electrolysis cell is not controlled, and the amplitude of the electrolyte and sludge movement is not taken into account.

As a rule, according to the statistical data, at plants producing cathode copper by the electrolytic method for 24 hours, there can be up to 15—20 cases with different scenarios. Most frequent is the 1st scenario (up to 10 cases per day). Figures 1 and 2 show models for all three scenarios.

The parametric analysis of the electrolysis process helps to determine the relationship between electrolysis process input data (DB) (electrode spacing, current intensity, current density, electrolyte resistance with regard to copper ion concentration) and their influence on electrolytic refining output indicators, such as current efficiency and productivity [23; 24]. However, additional control parameters of the process need to be taken into account, for example, the sludge level on the bottom of the bath and the pH index [25].

The construction of a mathematical model of the parametrical analysis of the copper electrolytic refining process (processes 1.1, 1.2 and 2 in Figure 3) was used [26—28] as an auxiliary method to evaluate and analyze control actions in the case of a production situation which may arise (according to the scenario) as per the obtained block diagram.

The following designations were adopted for the block diagram and calculated mathematical model of the process: input parameters of the electrolyte composition — sulfuric acid content $C_{H_2SO_4} = 150$ g/L; concentration

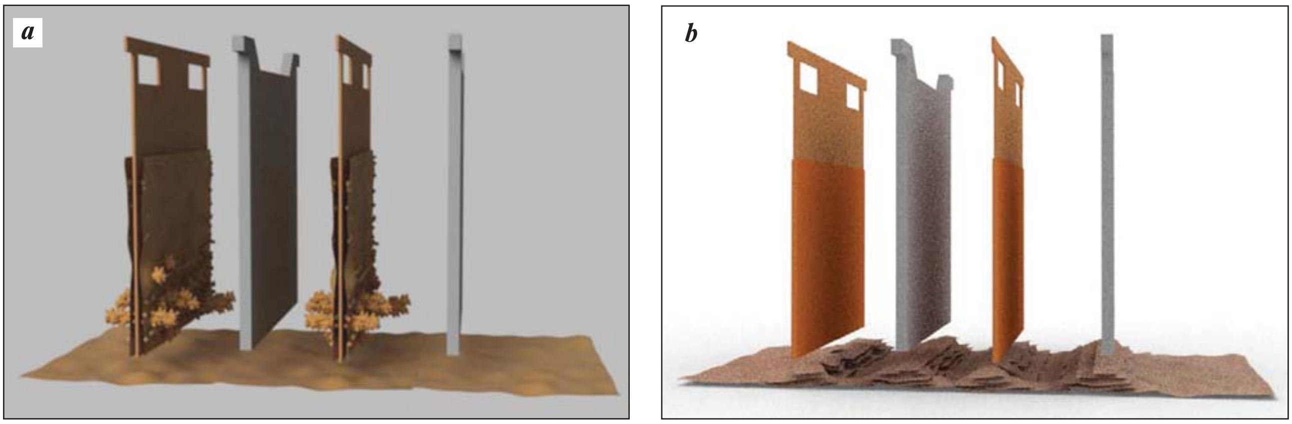

Fig. 1. Model of sludge formation and level change at medium (***a***) and high (***b***) electrolyte turbulence

Рис. 1. Модель образования и изменения уровня шламового осадка при средней (***a***) и высокой (***b***) турбулентности электролита

Fig. 2. Model of complete short-circuiting of the electrodes when the sludge touches the lower part of the electrodes

Рис. 2. Модель полного замыкания электродов при касании осадка нижней части электродов

of copper sulfate $C_{\mathrm{CuSO_4}}$ = 279.78 g/L; copper content C_{Cu} = 50 g/L. At a given electrolyte composition the following were obtained: current efficiency $\eta^*_{\mathrm{Cu}} = 96$ % and productivity $\mathrm{Pr}^*_{\mathrm{Cu}}$ = 50 t/day; d_{Pr}, d_{Cu} — process efficiency and current efficiency for electrolytic processes 1.1 and 1.2 respectively, which differ in value. In this case the controls are current density (D) and circulation rate (V).

There is a known mathematical model of the copper electrolytic refining process [3] Within its framework, multi-parameter mathematical models using multiple regression analysis can be obtained [29—31]. Equation (1) can be applied to the adjustment of the APCS and control of sludge, taking into account the current efficiency value. Equation (2) can be applied to productivity:

$$\eta_{\mathrm{Cu}} = 885.52052 + 0.01869V + 0.01048D^2 - 5.79232D + 1.43\cdot10^{-4}(C_{\mathrm{H_2SO_4}})^2 - 0.01231C_{\mathrm{H_2SO_4}} + 0.09\cdot10^{-5}(C_{\mathrm{Cu}})^2 - 4.98\cdot10^{-3}C_{\mathrm{Cu}} + 3.5\cdot10^{-4}(C_{\mathrm{H_2SO_4}})^2 - 0.07688C_{\mathrm{CuSO_4}}, \quad (1)$$

$$\mathrm{Pr}_{\mathrm{Cu}} = -122.6664 + 0.0145V - 2.4\cdot10^{-3}D^2 + 1.30096D + 3.6\cdot10^{-4}(C_{\mathrm{H_2SO_4}})^2 - 0.09653C_{\mathrm{H_2SO_4}} + 4.4\cdot10^{-5}(C_{\mathrm{Cu}})^2 - 2.7\cdot10^{-3}C_{\mathrm{Cu}} + 2.1\cdot10^{-4}(C_{\mathrm{CuSO_4}})^2 - 0.0436C_{\mathrm{CuSO_4}}. \quad (2)$$

Additional parameterization reflects the true values of the current efficiency and productivity, taking into account the detected deviations with further correction of the process mode through control (see block diagram in Figure 3). The block diagram is based on the mathematical model of the electrolytic refining process, and on the model of functional relations of the current values of control variables (current density D and circulation rate V). This is achieved by a comparison of productivity values ($\mathrm{Pr}_{\mathrm{Cu}}$) and the current efficiency (η_{Cu}), with preset parameters of processes 1.1 and 1.2 with a delay factor. In contrast to the existing model, adjustments were made according to the three assumed mechanisms of sludge formation and dendritic accretions on the electrodes.

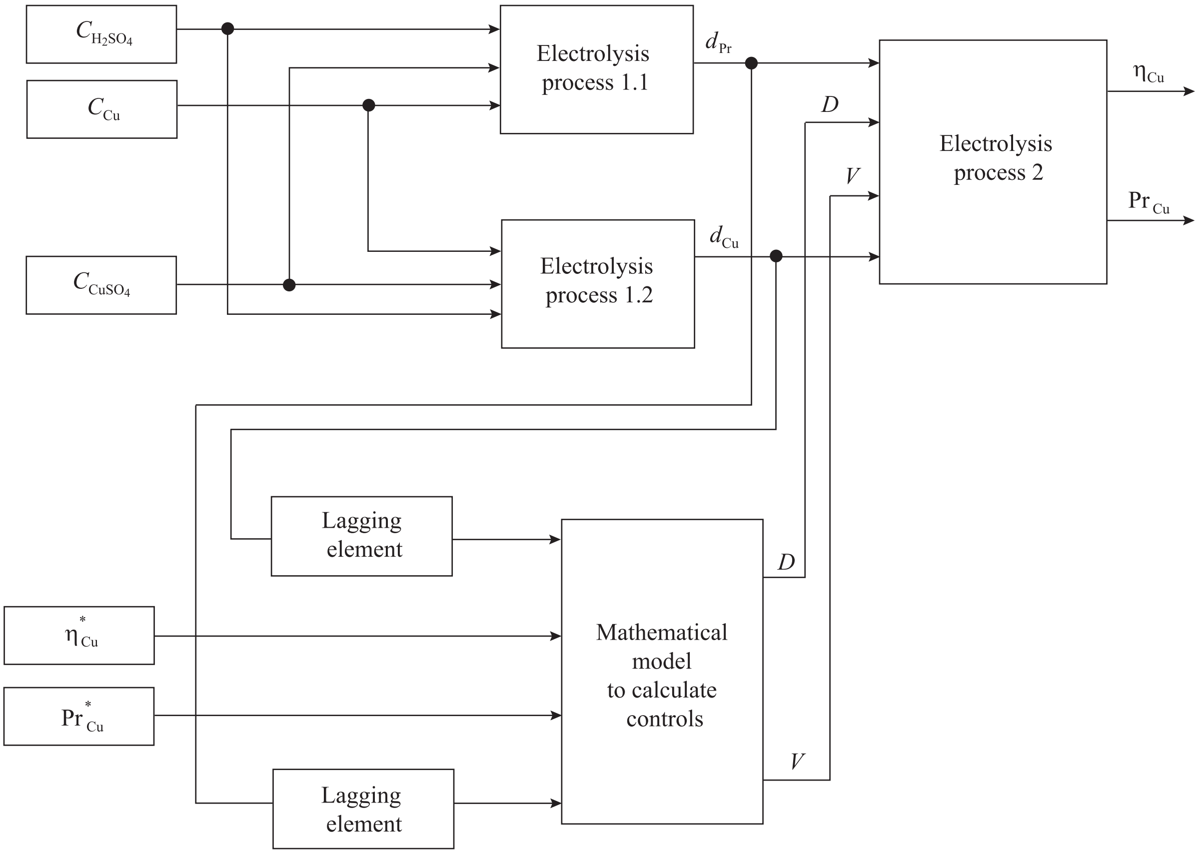

Fig. 3. Block diagram of the mathematical model for the parametric analysis of cathode copper electrolytic production

Рис. 3. Блок-схема математической модели параметрического анализа электролитического производства катодной меди

The dependence of the current density and resistance on the electrode spacing can be obtained with the help of the preset regime of control and monitoring under conditions (1), and also (2) on the basis of the completed mathematical model of the electrolytic copper refining process and the block diagram (Fig. 4). Data shows that the current density variation range is within the rational limits $D = 250÷300$ A/m^2, and the inter-electrode distance varies in the range of 0.045—0.055 m.

When evaluating the effect of current density, it was found that the rated productivity reaches an optimum value when the control D is in the range of 260—280 A/m^2 (Figure 5).

The introduction of additional input parameters for the electrolysis process can be justified, based on the performed parametric analysis.

The value of the copper ion content is also a very important factor. As the Cu^{2+} concentration increases, the current efficiency increases and the bath voltage decreases as the precipitation level decreases. A high copper concentration can increase current efficiency. The copper concentration is usually maintained at a level of 40—60 g/L in terms of the divalent copper cation.

It should be noted that the content of sulfuric acid significantly affects the current efficiency and power consumption. As a rule, its level is maintained in the range of $C_{H_2SO_4} = 100÷150$ g/L.

Temperature growth affects current efficiency growth. However, with decreasing voltage in the bath, the conductivity of the electrolyte increases. In the temperature range of 20—70 °C there is a general tendency towards an increase in dispersity. On the other hand, the physical properties of the electrolyte deteriorate and the cathodic precipitate begins to dissolve. Therefore, the temperature of the electrolyte is maintained at 50—60 °C, and its circulation in the baths is carried out, in order to maintain a given temperature therein. A further objective is to reduce the stratification of the electrolyte due to different densities of the $CuSO_4$ and H_2SO_4 solutions and its components,

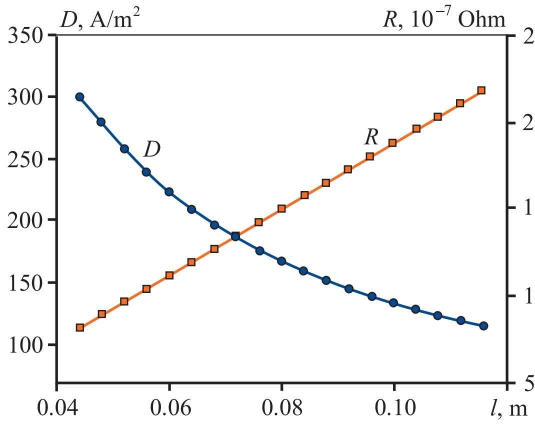

Fig. 4. Influence of inter-electrode distance on current density and resistance

Рис. 4. Влияние межэлектродного расстояния на плотность тока и сопротивление

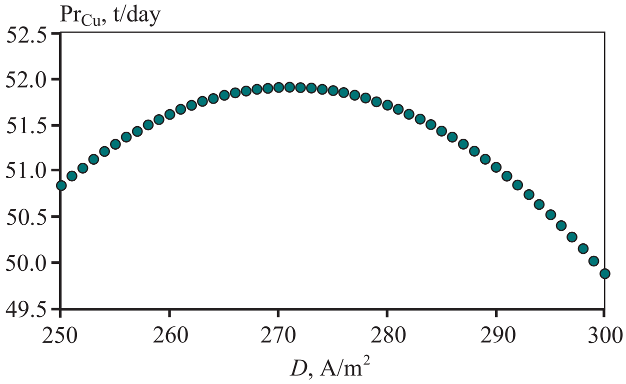

Fig. 5. Dependence of the process productivity on the current density

Рис. 5. Зависимость производительности процесса от плотности тока

while stabilizing the process of electrolyte mixing to saturate the cathode layer with copper ions [4]. It follows from the data obtained that the rate of electrolyte circulation should be kept constant at a level of 20 L/min.

Improving the monitoring and control system for the electrolysis process by introduction of additional parameters

During copper electrolytic refining, the weights of anodes and cathodes, anode residues, cathode scrap, initial cathodes, and used reagents are controlled. The volume of electrolyte removed from circulation and the introduced volume of sulfuric acid are calculated. The electrolyte level in the tank equipment is also determined, inter alia. It is most important that the composition and temperature of the electrolyte be controlled, as well as the process of detecting short circuits between the anodes and cathodes at the calculated values of the electrolyte circulation rate. There also needs to be additional control of the electrolyte content and the sludge level on the bottom of the bath.

Small-size analyzers (types MAK-1 and MAK-2) are used to control the content of copper and acid in the electrolyte. In order to determine the flow rate of steam, water, and electrolyte, differential pressure gauges with recorders are used, and the temperature is measured with resistance thermometers. The use of temperature sensors with remote control allows for electrolyte temperature control [32; 33] to be fully automated.

Various methods are used to detect and eliminate short circuits resulting in a disturbance of normal electrode current supply and a decrease in the current efficiency. Gaussmeters, thermal sensitive paints, and infrared sensors are used. Of great interest is the method of short-circuit detection by means of a camera with an infrared radiation sensor (thermal imager) installed on an overhead crane serving electrolysis baths [34—37]. Using modern methods, labor costs for short-circuit monitoring are reduced up to 30 %, when compared to traditional monitoring systems. Current efficiency is increased by 2 %.

Based on the above factors, software has been created that allows for a more effective control of the process characteristics of copper electrolysis. The working algorithm of the software is shown in Figure 6.

The block diagram includes the following designations for the input data and controls transfer:

1 — process start (input of parameters to the database);

2 — process duration check (τ, min) and final timing (when 48 hours are reached, the process is considered to be completed);

3 — collection of the following current data from sensors:

- — electrolyte temperature (t, °C);
- — voltage (U, V);
- — sludge level (H_{sl}, m);
- — electrolyte level (H_{e}, m);
- — concentration of sulfuric acid in the electrolyte ($C_{\text{H}_2\text{SO}_4}$, kg/m^3);

4 — check of electrolyte temperature in the permissible range $t_{\text{e}} < 85$ °C;

5 — check of voltage between the electrodes with the necessary value of $U = 0.314$ V; voltage has the

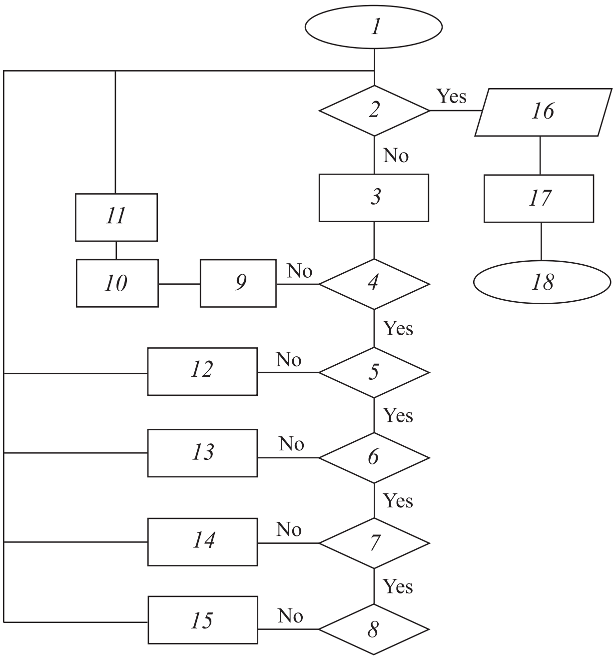

Fig. 6. Block diagram of the software algorithm

Рис. 6. Блок-схема алгоритма работы программы ЭВМ

function of response, which in practice is not regulated;

6 — check of the slurry level within the permissible limits $H_{\text{sl}} < 0.4$ m (no short circuit in the lower part of the electrode);

7 — check of the electrolyte level;

8 — check of the concentration of sulfuric acid in the electrolyte;

9 — beginning of scanning the cell surface (in the bath) with a thermal imaging camera;

10 — detection of the zones of electrolyte overheating (with short circuits); indicate the numbers of the cathode and anode on the screen;

11 — elimination of short circuit and fixing the time (timing);

12 — direct sludge to drain to the receiver;

13 — add electrolyte up to the set target level;

14 — add sulfuric acid to the electrolyte up to the target concentration value;

15 — displaying on the screen of the report about the electrolysis parameters change process;

16 — completion of the electrolysis parameters adjustment process;

17 — stabilization of the process and reaching the normal process mode;

18 — regulator of the overflow system for sludge removal.

Figure 7 shows the diagram of digital automation of the electrolysis bath for copper refining.

Figure 8 shows the screen shot of the developed software for sludge and dendritic accretions control.

The electrode spacing, and therefore the voltage setpoint, can be varied according to the changes occurring on the electrolyzer. Additionally, if significant deviations are detected, the ampere load can also be changed.

As a result, in the course of studying the problems of the stable operation of electrolysis cells, a system for monitoring and controlling the main parameters of the cathode copper production process was created. The software consists of the following products:

— BMXCPS3500 power supply unit;

— Modicon M580 P58 2040 processor module;

— BMXDDI 1602 digital input module, number of digital inputs 16;

— BMXAMM0600 analog input-output module, number of digital inputs 8 in accordance with the algorithm actions;

— BMXDDO 1602 digital output module, number of analog inputs 16.

The software was developed in the Unity XL Pro environment of Schneider Electric and is localized for Russian use in the SE (System Electric) environment.

Additional process control functions via an APCS allow for more efficient and timely elimination of process deviations. The increased frequency of cathode change and sludge removal result in the reduction of economic indicators of the process.

Conclusion

The intensification of the electrolysis process occurs mainly due to an increase in current density value and an improvement in the electrolyte circulation system operation for maintaining the constant copper ions concentration at electrolyte stabilizing temperature.

The introduction of sludge level sensors for the additional monitoring of the process will reduce irretrievable losses of cathode copper in the absence of short circuits of dendritic sludge on electrodes in the lower part of the electrolyzer. Models of cathode sludge formation and dendritic short-circuits on electrodes have been built. An analysis of possible problems and deviations associated with sludge formation allowed for a number of possible process scenarios to be simulated.

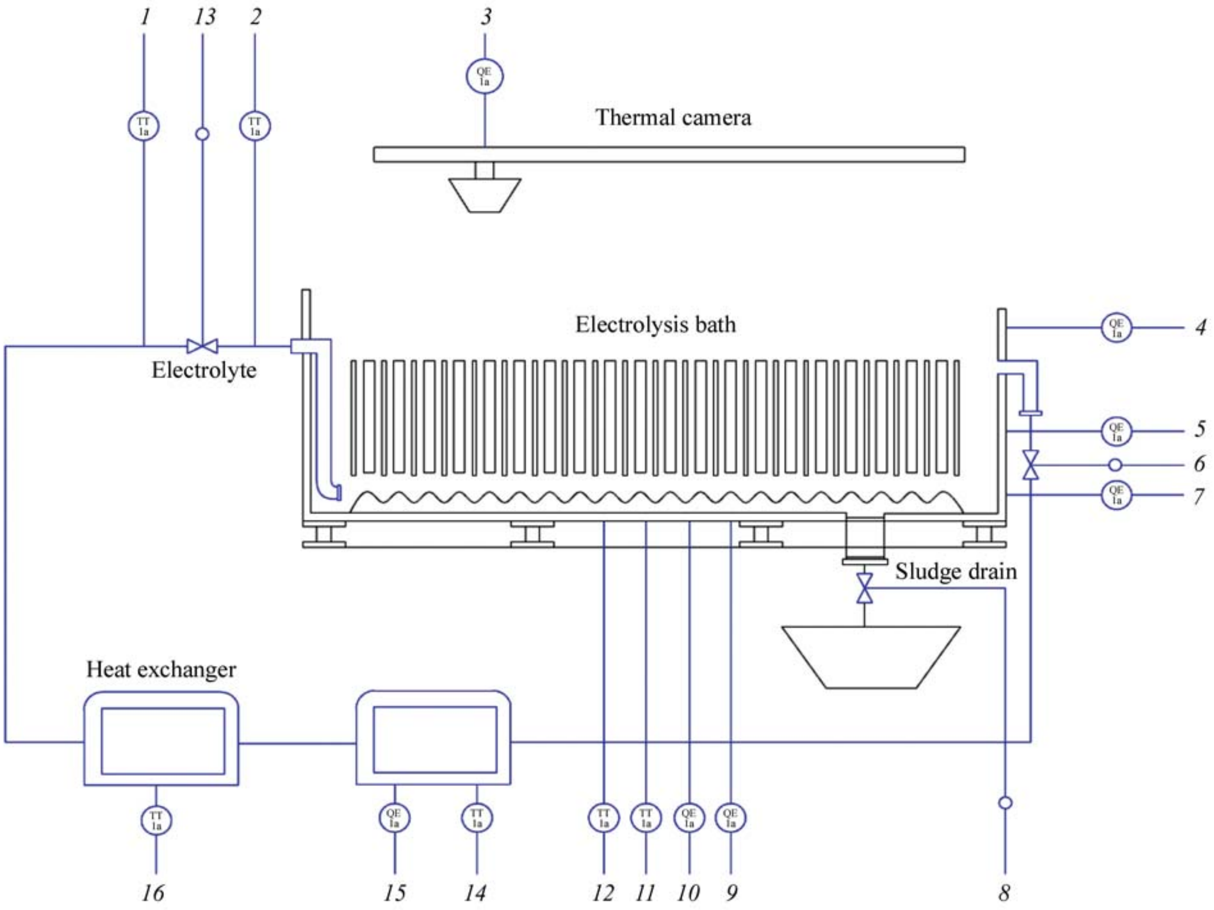

Fig. 7. Diagram of digital automation of the electrolysis bath for copper refining

Рис. 7. Схема цифровой автоматизации электролитической ванны для рафинирования меди

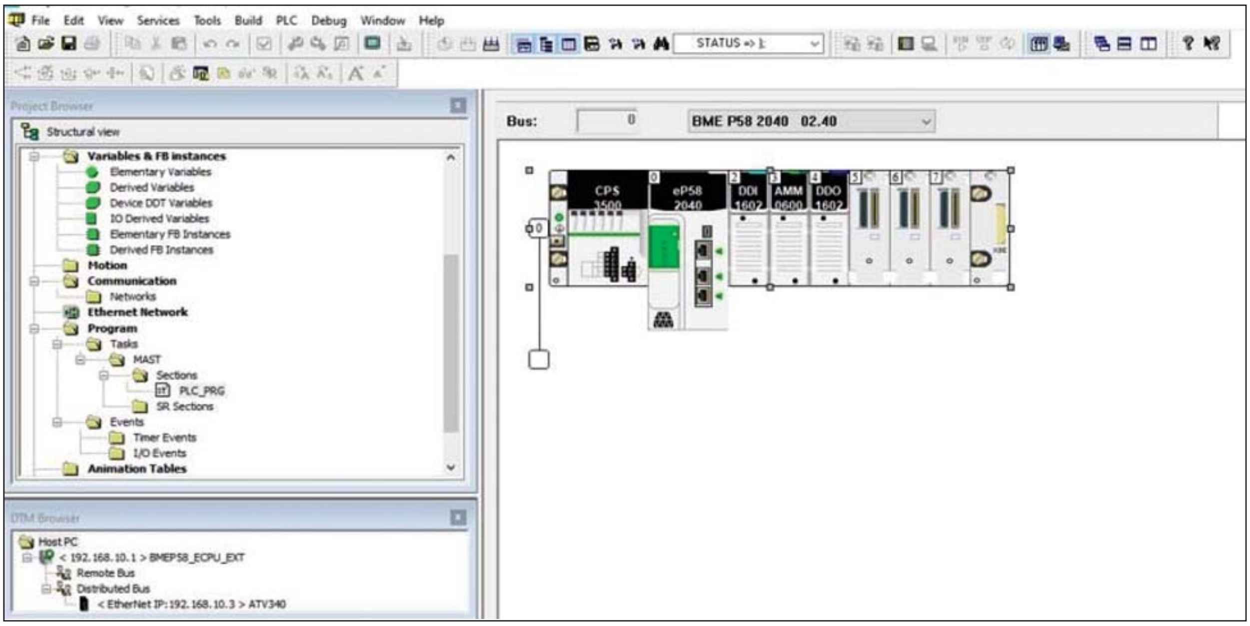

Bus: 0 BME P58 2040 02.40

Fig. 8. Screen shot of the developed software for sludge and dendritic accretions control

Рис. 8. Скриншот разработанной программы контроля шламового осадка и дендритных срастаний

The control algorithm and software developed for additional actions in the APCS system help energy losses to be reduced (by 10—15 %) and current efficiency to be increased (by 2 %).

This work can be usefully implemented in existing APCS of copper electrolytic refining for the copper smelting plant (Lao Cai, Socialist Republic of Vietnam).

References

1. Litvinenko V., Bowbrick I., Naumov I., Zaitseva Z. Global guidelines and requirements for professional competencies of natural resource extraction engineers: Implications for ESG principles and sustainable development goals. *Journal of Cleaner Production*. 2022;338:130530. https://doi.org/10.1016/j.jclepro.2022.130530
2. Litvinenko V.S. Digital economy as a factor in the technological development of the mineral sector. *Natural Resources Research*. 2020;29:1521—1541. https://doi.org/10.1007%2Fs11053-019-09568-4
3. Potekhin D.V., Galkin S.V. Use of machine learning technology to model the distribution of lithotypes in the permo-carboniferous oil deposit of the usinskoye field. *Journal of Mining Institute*. 2023;259:41—51. https://doi.org/10.31897/PMI.2022.101
4. Qingyu Zeng, Chun Li, Yi Meng, Jun Tie, Rentao Zhao, Zhifang Zhang. Analysis of interelectrode short-circuit current in industrial copper electrorefining cells. *Measurement*. 2020;164:108015. https://doi.org/10.1016/j.measurement.2020.108015
5. Mansouri N., Khayati G.R., Mohammad Hasani Zade, Mohammad Javad Khorasani S., Kafi Hernashki R. A new feature extraction technique based on improved owl search algorithm: a case study in copper electrorefining plant. *Neural Computing and Applications*. 2022;34:7749—7814. https://doi.org/10.1007/s00521-021-06881-z
6. Tarantseva K., Fayustova Yu. Efficiency of wastewater treatment from iron, copper and nickel ions by sorbent from water purification sludge. *Ecology and Industry of Russia*. 2023;27(2):22—25. (In Russ.). https://doi.org/10.18412/1816-0395-2023-2-22-25

   Таранцева К.Р., Фаюстова Ю.А. Эффективность очистки сточных вод от ионов железа, меди и никеля сорбентом из шлама водоочистки. *Экология и промышленность России*. 2023;27(2):22—25. https://doi.org/10.18412/1816-0395-2023-2-22-25
7. Mansurova O.K., Chitkova Ya.V. Research of processes in electrolytic refining of copper. In: *Innovative scientific research: theory, methodology, practice*: Materials of the XX Intern. scientific and practical conference (Penza, 23 February 2020). Penza: Nauka i Prosveshchenie, 2020. P. 47–52. (In Russ.).

   Мансурова О.К., Читкова Я.В. Исследование процессов при электролитическом рафинировании меди. В сб.: *Инновационные научные исследования: теория, методология, практика:* Материалы XX Междунар. науч.-практ. конференции (Пенза, 23 февраля 2020 г.). Пенза: Наука и Просвещение, 2020. С. 47—52.
8. Shestakov A.K., Petrov P.A., Nikolaev M.Yu. Automatic system for detecting visible emissions in a potroom of aluminum plant based on technical vision and a neural network. *Metallurgist*. 2023;66:1308—1319. https://doi.org/10.1007/s11015-023-01445-z
9. Mastyugin S.A., Volkova N.A., Naboichenko S.S., Lastochkina M.A. Sludge from electrolytic refining of copper and nickel. Ekaterinburg: UrFU, 2013. 256 p. (In Russ.).

   Мастюгин С.А., Волкова Н.А., Набойченко С.С., Ласточкина М.А. Шламы электролитического рафинирования меди и никеля. Екатеринбург: УрФУ, 2013. 256 с.
10. Khudyakov P.Yu., Fedorova S.V., Simonov A.Yu., Startsev I.M., Laptev V.A. Automatic short circuit identification system in electrolysis baths. *Datchiki i Sistemy (Sensors and Systems)*. 2020;(9-10(251)):61—66. (In Russ.). https://doi.org/10.25728/datsys.2020.9-10.11

    Худяков П.Ю., Федорова С.В., Симонов А.Ю., Старцев И.М., Лаптев В.А. Автоматическая система идентификации коротких замыканий в электролизных ваннах. *Датчики и системы*. 2020;(9-10(251)):61—66. https://doi.org/10.25728/datsys.2020.9-10.11
11. Volkhin A.I., Chukhlantsev N.M., Plekhanov I.D., Spirin V.E., Serikova V.V., Sizov V.A., Vinnik V.I. Device for detecting short circuits in copper electrolysis baths: Patent 55779 (RF). 2006. (In Russ.).

    Вольхин А.И., Чухланцев Н.М., Плеханов И.Д., Спирин В.Е., Серикова В.В., Сизов В.А., Винник В.И.. Устройство для обнаружения коротких замыканий в ваннах электролиза меди: Патент 55779 (РФ). 2006.
12. Goronko V.A. Device for determining the short circuit current in electrolysis baths: Patent 140216 (USSR). 1960. (In Russ.).

    Горонько В.А. Устройство для определения тока короткого замыкания в электролизных ваннах: Патент 140216 (СССР). 1960.

13. Zakharov L., Martyushev D., Ponomareva I.N. Predicting dynamic formation pressure using artificial intelligence methods. *Journal of Mining Institute*. 2022;253:23—32. (In Russ.).
https://doi.org/10.31897/PMI.2022.11
Захаров Л.А., Мартюшев Д.А., Пономарева И.Н. Прогнозирование динамического пластового давления методами искусственного интеллекта. *Записки Горного института*. 2022;253:23—32.
https://doi.org/10.31897/PMI.2022.11
14. Salimzhanova E.V., Devochkin A.I., Yudin E.V., Karpushova D.D. Development and indtroduction of technical solutions to bring the quality of polar division cathode copper to conformity with London Metal Exchange standard. *Tsvetnye Metally*. 2018;6:44—51. (In Russ.). https://doi.org/10.17580/tsm.2018.06.06
Салимжанова Е.В., Девочкин А.И., Юдин Е.В., Карпушова Д.Д. Разработка и внедрение технических решений по приведению качества катодной меди полярного деления в соответствие со стандартом Лондонской биржи металлов. *Цветные металлы*. 2018;6:44—51. https://doi.org/10.17580/tsm.2018.06.06
15. Mohammad Reza Shojaei, Gholam Reza Khayati, Seyed Mohammad Javad Korasani, Roya Kafi Harnashki. Investigating the nodulation mechanism of copper cathode based on microscopic approach: As a punch failure factor. *Engineering Failure Analysis*. 2022;133:105970.
https://doi.org/10.1016/j.engfailanal.2021.105970
16. Zakaev D., Nikolaichuk L., Irina F. Problems of oil refining industry development in Russia. *International Journal of Engineering Research and Technology*. 2020;13(2):267—270.
https://doi.org/10.37624/IJERT/13.2.2020.267-270
17. Jingya Zhao, Yi Meng, Chun Li, Jun Tie. The effect of nodulation on the distribution of concentration and current density during copper electrolytic refining. *Journal of Physics: Conference Series*. 2022;2285:012015.
https://doi.org/10.1088/1742-6596/2285/1/012015
18. Gazaleeva G.I., Nazarenko L.N., Shigaeva V.N. Process flow design for upgrading rough concentrates containing fine slimes of tin and copper minerals. *Obogashchenie Rud*. 2018;(6(378)):20—26. (In Russ.).
https://doi.org/10.17580/or.2018.06.04
Газалеева Г.И., Назаренко Л.Н., Шигаева В.Н. Схема технологического процесса обогащения черновых концентратов, содержащих мелкие шламы оловянных и медных минералов. *Обогащение руд*. 2018;(6(378)):20—26. https://doi.org/10.17580/or.2018.06.04
19. Ding L., Li Q., Yuan J., Dong X., Peng D., Li B., Li H., Xue Y., Niu Y. Characteristic and control of electrochemical oscillation at the anode during electrolytic refining copper. *International Journal of Electrochemical Science*. 2020;15(9):9532—9542.
https://doi.org/10.20964/2020.09.85
20. Selivanov E.N., Sergeeva S.V., Korolev A.A., Timofeev K.L., Krayukhin S.A., Pikulin K.V. Impurity distribution during electrolytic refining of antimony. *Metallurgist*. 2021;64:1198—1207.
https://doi.org/10.1007/s11015-021-01105-0
21. Boikov A.V., Payor V.A., Savelev R.V. Technical vision system for analyzing the mechanical characteristics of bilk materials. *Journal of Physics: Conference Series*. 2018;944:012021.
https://doi.org/10.1088/1742-6596/944/1/012021
22. Shklyarskiy Y.E., Batueva D.E., Operation mode selection algorithm development of a wind-diesel power plant supply complex. *Journal of Mining Institute*. 2022;253:115—126. (In Russ.). https://doi.org/10.31897/PMI.2022.7
Шклярский Я.Э., Батуева Д.Е. Разработка алгоритма выбора режимов работы комплекса электроснабжения с ветродизельной электростанцией. *Записки Горного института*. 2022;253:115—126.
https://doi.org/10.31897/PMI.2022.7
23. Ding L., Cheng J., Wang T., Zhao J., Chen C., Niu Y. Continuous electrolytic refining process of cathode copper with non-dissolving anode. *Minerals Engineering*. 2019;135:21—28.
https://doi.org/10.1016/j.mineng.2019.02.032
24. McNulty B.A., Jowitt S.M., Belousov I. The importance of geology in assessing by- and coproduct metal supply potential; a case study of antimony, bismuth, selenium, and tellurium within the copper production stream. *Economic Geology*. 2022;117(6):1367—1385.
https://doi.org/10.5382/econgeo.4919
25. Correa P.P., Cipriano A., Nunez F., Salas J.C., Lobel H. Forecasting copper electrorefining cathode rejection by means of recurrent neural networks with attention mechanism. *IEEE Access*. 2021;9:79080—79088.
https://doi.org/10.1109/ACCESS.2021.3074780
26. Zhang J., Chen H., Fan B., Shan H., Chen Q., Jiang C., Hou G., Tang Y. Study on the relationship between crystal plane orientation and strength of electrolytic copper foil. *Journal of Alloys and Compounds*. 2021;884:10—16.
https://doi.org/10.1016/j.jallcom.2021.161044
27. Ostanin N.I., Rudoy V.M., Demin I.P., Ostanina T.N., Nikitin V.S. Statistical analysis of the distribution of im-

purities during copper electrorefining. *Russian Journal of Non-Ferrous Metals.* 2021;62(5):501—507.
https://doi.org/10.3103/S1067821221050102

28. Boikov A.V., Savelev R.V., Payor V.A., Potapov A.V. Evaluation of bulk material behavior control method in technological units using DEM. Part 2. *CIS Iron and Steel Review.* 2020;20:3—6.
https://doi.org/10.17580/cisisr.2020.02.01
29. Vasilyeva N.V., Boikov A.V., Erokhina O.O., Trifonov A.Yu. Automated digitization of radial charts. *Journal of Mining Institute.* 2021;247:82—87. (In Russ.).
https://doi.org/10.31897/PMI.2021.1.9
Васильева Н.В., Бойков А.В., Ерохина О.О., Трифонов А.Ю. Автоматизированная оцифровка круговых диаграмм. *Записки Горного института.* 2021;247:82—87. https://doi.org/10.31897/PMI.2021.1.9
30. Kashin D.A., Kulchitskiy A.A. Image-based quality monitoring of metallurgical briquettes. *Tsvetnye Metally.* 2022;9(957):92—98. (In Russ.).
https://doi.org/10.17580/tsm.2022.09.13
Кашин Д.А., Кульчицкий А.А. Контроль качества металлургических брикетов на основе изображений брикетированной металлошихты. *Цветные металлы.* 2022;9(957):92—98.
https://doi.org/10.17580/tsm.2022.09.13
31. Sharikov Y.V., Cabascando V.E.Q. Mathematical modeling of mass, heat and fluid flow in a reverberatory furnace for melting nickel-containing raw materials. *Journal of Physics: Conference Series.* 2021;1753:1—8.
https://doi.org/10.1088/1742-6596/1753/1/012064
32. Bian Y., Su L., Yu Z., Lv Z., Chen H., Zhou Y., Lin M. Graphite/copper phthalocyanine composite cathode for overcharge protection and gas evolution suppression in aluminum-ion batteries at room temperature. *Electrochimica Acta*. 2019;332:1—23.
https://doi.org/10.1016/j.electacta.2019.135188
33. Sonawane J.M., Pant D., Ghosh P.C., Adeloju S.B. Polyaniline—copper composite: A non-precious metal cathode catalyst for low-temperature fuel cells. *Energy Fuels*. 2021;35(4):3385—3395.
https://doi.org/10.1021/acs.energyfuels.0c04152
34. Van Doremalen R.F.M., Van Netten J.J., Van Baal J.G., Vollenbroek-Hutten M.M.R., Van der Heijden F. Validation of low-cost smartphone-based thermal camera for diabetic foot assessment. *Diabetes Research and Clinical Practice.* 2019;149:132—139.
https://doi.org/10.1016/j.diabres.2019.01.032
35. Han Ji-H., Khoo E., Bai P., Bazant M.Z. Over-limiting current and control of dendritic growth by surface conduction in nanopores. *Scientific Reports.* 2014;4(7056):1—8.
https://doi.org/10.1038./srep07056
36. Zubov V.P., Than Van Duy, Fedorov A.C. Technology of underground mining of thick coal seams with low strength properties. *Ugol'.* 2023;(5):37—45. (In Russ.).
http://dx.doi.org/10.18796/0041-5790-2023-5-37-45
Зубов В.П., Тхан Ван Зуи, Федоров А.С. Технология подземной разработки мощных пластов угля с низкими прочностными характеристиками. *Уголь.* 2023;(5):37—45.
http://dx.doi.org/10.18796/0041-5790-2023-5-37-45
37. Pryakhin E.I., Troshina E.Yu. Study of technological and operational features of high-temperature-resistant composite films for laser marking of parts made of ferrous alloys. *Chernye metally.* 2023;(4):74—80. (In Russ.).
https://doi.org/10.17580/chm.2023.04.12
Пряхин Е.И., Трошина Е.Ю. Изучение технологических и эксплуатационных особенностей высокотемпературостойких композитных пленок для лазерной маркировки деталей из черных сплавов. *Черные металлы.* 2023;(4):74—80.
https://doi.org/10.17580/chm.2023.04.12

Information about the authors

Nguyen Huy Hoang – Postgraduate Student of the Department of automation of technological processes and production, Saint Petersburg Mining University.
https://orcid.org/0000-0001-7025-8654
E-mail: huyhoangmta45@gmail.com

Vladimir Yu. Bazhin – Dr. Sci. (Eng.), Prof., Head of the Department of metallurgy, Saint Petersburg Mining University.
https://orcid.org/0000-0001-8231-3833
E-mail: bazhin-alfoil@mail.ru

Информация об авторах

Нгуен Хю Хоанг – аспирант кафедры автоматизации технологических процессов и производств Санкт-Петербургского горного университета.
https://orcid.org/0000-0001-7025-8654
E-mail: huyhoangmta45@gmail.com

Владимир Юрьевич Бажин – д.т.н., проф., заведующий кафедрой металлургии Санкт-Петербургского горного университета.
https://orcid.org/0000-0001-8231-3833
E-mail: bazhin-alfoil@mail.ru

Contribution of the authors

Nguyen Huy Hoang – conducting experiments, writing the software and part of the article.

V.Yu. Bazhin – determination of the purpose of the work, writing part of the article, participation in the discussion of the results.

Вклад авторов

Нгуен Хю Хоанг – проведение экспериментов, написание программы и части статьи.

В.Ю. Бажин – определение цели работы, написание части статьи, участие в обсуждении результатов.

The article was submitted 30.03.2023, revised 14.04.2023, accepted for publication 20.04.2023

Статья поступила в редакцию 30.03.2023, доработана 14.04.2023, подписана в печать 20.04.2023

METALLURGY OF NONFERROUS METALS / МЕТАЛЛУРГИЯ ЦВЕТНЫХ МЕТАЛЛОВ

UDC 544.654; 546.831
https://doi.org/10.17073/0021-3438-2023-3-17-26

Research article
Научная статья

Silicon electrodeposition from the KF–KCl–K_2SiF_6 and KF–KCl–KI–K_2SiF_6 melts

S.I. Zhuk[1,2], **L.M. Minchenko**[1], **A.V. Suzdaltsev**[1,2], **A.V. Isakov**[1], **Yu.P. Zaikov**[1,2]

[1] **Institute of High-Temperature Electrochemistry of Ural Branch of the Russian Academy of Sciences**
20 Akademicheskaya str., Ekaterinburg, 620137, Russia

[2] **Ural Federal University n.a. the First President of Russia B.N. Eltsin**
19 Mira str., Ekaterinburg, 620002, Russia

✉ Andrey V. Suzdaltsev (suzdaltsev_av@ihte.uran.ru, a.v.suzdaltsev@urfu.ru)

Abstract: Silicon and silicon-based materials find extensive applications in metallurgy, microelectronics, and other emerging industries. The field of use of synthesized silicon varies based on its morphology and purity. This study employs voltammetry, galvanostatic electrolysis, and scanning electron microscopy to examine the impact of KI surfactant (in mol.%) to 66.5KF–33.3KCl–0.23K_2SiF_6 melt at 750 °C on the electrowinning kinetics of silicon ions and the morphology of silicon deposits formed on a glassy carbon electrode. The findings demonstrate that the addition of potassium iodide to the KF–KCl–K_2SiF_6 melt at a concentration of 2 mol.% induces changes in interfacial tension at the boundary between the glassy carbon, melt, and atmosphere. Consequently, the wetting of the glassy carbon with the melt decreases, leading to a reduction in the actual working surface area and, consequently, a decrease in cathode current while maintaining current density. Taking into account this effect and employing an algebraic estimation of the influence of the melt meniscus shape, it is postulated that the addition of KI does not significantly affect the kinetics of the cathode process. Nevertheless, the impact of KI addition on the morphology of electrodeposited silicon is mentioned. During the electrolysis of the KF–KCl–K_2SiF_6 melt, fibrous silicon deposits with arbitrary shapes are formed on the glassy carbon electrode, whereas the addition of 2 and 4 mol.% of potassium iodide to the melt leads to the agglomeration and smoothing of silicon deposits under the same electrolysis conditions (cathode current density: 0.02 A/cm^2, electrolysis duration: 2 h). The obtained results indicate the potential to manipulate the morphology of electrodeposited silicon for specific applications in various fields..

Keywords: silicon, voltammetry, electrodeposition, morphology, KF–KCl melt.

Acknowledgments: The analysis of silicon deposits was conducted using the equipment available at the “Substance composition” Core facilities center, Institute of High Temperature Electrochemistry, Ural Branch, Russian Academy of Sciences.

For citation: Zhuk S.I., Minchenko L.M., Suzdaltsev A.V., Isakov A.V., Zaikov Yu.P. Silicon electrodeposition from the KF–KCl–K_2SiF_6 and KF–KCl–KI–K_2SiF_6 melts. Izvestiya. Non-Ferrous Metallurgy. 2023;29(3):17–26.
https://doi.org/10.17073/0021-3438-2023-3-17-26

Электроосаждение кремния из расплавов KF–KCl–K_2SiF_6 и KF–KCl–KI–K_2SiF_6

С.И. Жук[1,2], **Л.М. Минченко**[1], **А.В. Суздальцев**[1,2], **А.В. Исаков**[1], **Ю.П. Зайков**[1,2]

[1] **Институт высокотемпературной электрохимии УрО РАН**
620137, Россия, г. Екатеринбург, ул. Академическая, 20

[2] **Уральский федеральный университет им. первого Президента России Б.Н. Ельцина**
620002, Россия, г. Екатеринбург, ул. Мира, 19

✉ Андрей Викторович Суздальцев (suzdaltsev_av@ihte.uran.ru, a.v.suzdaltsev@urfu.ru)

Аннотация: Кремний и материалы на его основе широко используются в металлургии, микроэлектронике и других развивающихся отраслях промышленности. Области применения синтезируемого кремния зависят от его морфологии и чистоты.

В данной работе методами вольтамперометрии, гальваностатического электролиза и сканирующей электронной микроскопии изучено влияние поверхностно-активной добавки KI в расплав (мол.%) 66,5KF–33,3KCl–0,23K_2SiF_6 при температуре 750 °C на кинетику электровосстановления ионов кремния и морфологию получаемых на стеклоуглеродном катоде кремниевых осадков. Показано, что введение в расплав KF–KCl–K_2SiF_6 йодида калия в количестве 2 мол.% приводит к изменению межфазного натяжения на границе стеклоуглерод–расплав–атмосфера, а именно к снижению смачиваемости стеклоуглерода расплавом, в результате чего реальная рабочая поверхность, а соответственно, и катодный ток уменьшаются при сохранении плотности тока. С учетом подобного воздействия и алгебраической оценки влияния формы мениска расплава сделано предположение, что добавка KI практически не сказывается на кинетике катодного процесса. При этом отмечено заметное влияние добавок KI на морфологию электроосаждаемого кремния. При электролизе расплава KF–KCl–K_2SiF_6 на стеклоуглероде формируются волокнистые осадки кремния произвольной формы, в то время как добавление 2 и 4 мол.% йодида калия в расплав приводит к агломерации и сглаживанию осадков кремния при прочих равных условиях электролиза (катодная плотность тока – 0,02 А/см^2, время электролиза – 2 ч). Полученные результаты указывают на возможность регулирования морфологии электроосаждаемого кремния с целью дальнейшего его применения в той или иной сфере.

Ключевые слова: кремний, вольтамперометрия, электроосаждение, морфология, расплав KF–KCl.

Благодарности: Анализы осадков кремния были выполнены на оборудовании Центра коллективного пользования «Состав вещества» Института высокотемпературной электрохимии УрО РАН.

Для цитирования: Жук С.И., Минченко Л.М., Суздальцев А.В., Исаков А.В., Зайков Ю.П. Электроосаждение кремния из расплавов KF–KCl–K_2SiF_6 и KF–KCl–KI–K_2SiF_6. *Известия вузов. Цветная металлургия.* 2023;29(3):17–26.
https://doi.org/10.17073/0021-3438-2023-3-17-26

Introduction

In contemporary industry, silicon and silicon-based materials hold substantial significance. Silicon finds extensive application in the manufacturing of alloys comprised of ferrous and non-ferrous metals, functional powdered materials, photoelectric converters, and electronics [1—3]. The considerable lithium capacity of silicon enables the utilization of composite materials derived from it as anode materials in lithium-ion power sources [4].

Silicon with specific properties and morphologies such as solid deposits, nano- and micro-sized wires, fibers, and tubes can be obtained through the electrochemical deposition of silicon from molten salts and ionic liquids [5—14]. Electrochemical techniques are well studied for production and refinement of various materials in molten salts [15—20]. In this context, herewith, it is feasible to regulate the electrodeposition process by adjusting factors such as cathode current density, cathode overvoltage, process temperature, and melt composition [21—23].

The commonly used electrolytes in laboratory settings for silicon production are water-soluble KF—KCl based melts [8—12]. These electrolytes facilitate electrolysis within a temperature range of 650—750 °C. Currently, the kinetics of the cathode process has been extensively investigated in relation to temperature, concentration of silicon-containing electroactive ions, substrate material, and polarization conditions. Experimental batches of silicon deposits were obtained under various electrolysis parameters, and a diagram was proposed to illustrate the impact of these parameters on the morphology of silicon deposits [12]. In the examined melt with K_2SiF_6 concentrations up to 5 wt.% on graphite, it is possible to produce solid, porous, and well-developed silicon deposits in the form of fibers with arbitrary shapes and ordered submicron particles. The formation of a solid deposit is favored by a low cathode current density, while an increase in current density results in a deposit with higher specific area. This phenomenon can be attributed to several factors:

— an excess growth rate of existing nuclei compared to the growth rate of new nuclei;

— silicon primarily deposition on the surface of nuclei due to diffusion limitations concerning the supply of electroactive ions to the cathode surface;

— co-deposition of potassium and its intercalations into graphite.

The likelihood of potassium co-deposition is supported by the observation that solid silicon deposits were formed on a silver cathode at elevated cathode current densities [12]. This further validates the previously mentioned ability to manipulate the morphology of deposited silicon during the electrolysis of molten salts by modifying the process parameters.

Furthermore, the morphology of silicon deposits can be regulated by incorporating additives that affect the physicochemical properties of the electrolyte. Particularly, this pertains to modifications in the electrical conductivity and surface tension of the molten medium. As such, in previous studies [24—26], the use of molten electrolytes based on iodides (KF—KCl—KI—K_2SiF_6, NaI—KI—K_2SiF_6) has been proposed for silicon electrodeposition. However, it should be noted that the iodide concentrations in these systems are 75 mol.% and higher, which complicates the comprehensive understanding of iodide's influence on both the kinetics and mechanisms of silicon recovery from electroactive ions, as well as the resulting deposit morphology during electrolysis.

The present work focuses on investigating the impact of KI on the kinetics of the cathode process on glass carbon in a KF—KCl melt, as well as the morphology of deposits formed during electrolysis.

Experimental

The measurements and electrodeposition tests were conducted using salts of chemical purity grade (Vekton, Russia), which were subjected to precleaning procedures. The salts were purified by hydrofluorination (KF, K_2SiF_6) [9], iodination (KI) [20], and preliminary potentiostatic cleaning electrolysis in molten salts [27]. The electrochemical measurements and silicon electrodeposition were performed under an argon atmosphere using a sealed stainless-steel retort (Fig. 1), which was placed inside a vertical resistance furnace. The electrolyte was contained in a glassy carbon crucible within a graphite beaker. In order to maintain the argon atmosphere upon the addition of KI to the melt, the cell design was equipped with a gateway. A glassy carbon electrode served as the working electrode, while monocrystalline silicon was utilized as a reference quasi-electrode and auxiliary electrode. Tungsten rods were used as current leads for the electrodes. The melt temperature was set and controlled at 750±2 °C using Pt/Pt—Rh thermocouples and a TP703 thermoregulator (Varta, Russia).

Current voltage dependencies were recorded using a glassy carbon electrode immersed in a melt consisting of 66.5KF—33.3KCl—0.23K_2SiF_6 (mol.%) at a temperature of 750 °C. The measurements were conducted using an AutoLab 302N potentiostat—galvanostat (Metrohm, Netherlands). In order to assess the impact of KI on wetting behavior of the glassy carbon electrode with the KF—KCl—K_2SiF_6 melt, the experiments were performed with a partially immersed electrode. The depth of immersion was varied from 5 to 15 mm. Electrolysis of the 66.5KF—33.3KCl—0.23K_2SiF_6 (mol.%) melt, with the addition of 2 and 4 mol.% KI, was carried out under the same condition of cathode current density (0.02 A/cm^2) and glassy carbon cathode immersion (15 mm).

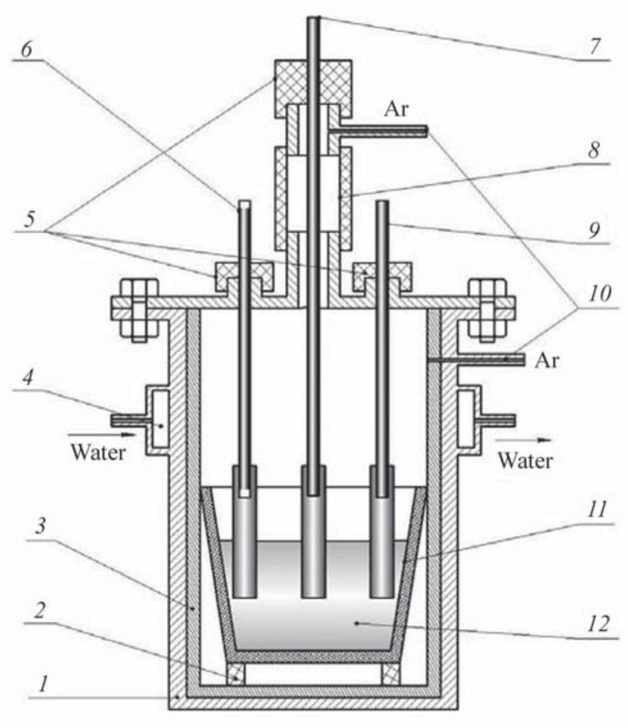

Fig. 1. Schematic view of experimental cell

1 – stainless-steel retort; ***2*** – graphite stand; ***3*** – nickel screen; ***4*** – cooling shell; ***5*** – rubber seals; ***6*** – quasi-reference electrode; ***7*** – working electrode; ***8*** – gateway; ***9*** – auxiliary electrode; ***10*** – inlet/outlet channels of inert gas; ***11*** – glassy carbon crucible; ***12*** – melt

Рис. 1. Схема экспериментальной ячейки

1 – реторта из нержавеющей стали; ***2*** – графитовая подставка; ***3*** – никелевый стакан; ***4*** – кожух охлаждения; ***5*** – уплотнения из вакуумной резины; ***6*** – электрод сравнения; ***7*** – рабочий электрод; ***8*** – шлюз; ***9*** – вспомогательный электрод; ***10*** – каналы подвода/отвода инертного газа; ***11*** – стеклоуглеродный тигель; ***12*** – расплав

The concentration of silicon in the melt before and after electrolysis was determined through atomic emission spectroscopy with inductively coupled plasma, employing an iCAP 6300 Duo Spectrometer (Thermo Scientific, USA). The morphology of the silicon deposits was examined utilizing a JMS-5900LV scanning electron microscope (JEOL, Great Britain), while the phase composition was assessed using a Rigaku D/MAX-2200VL/PC diffractometer (Rigaku, Japan).

Results and discussion

Electrochemical measurements. Figure 2 illustrates the current voltage dependencies acquired at a glassy carbon cathode immersed in a KF—KCl—K_2SiF_6 melt at a temperature of 750 °C, both with and without the addition of 2 mol.% KI.

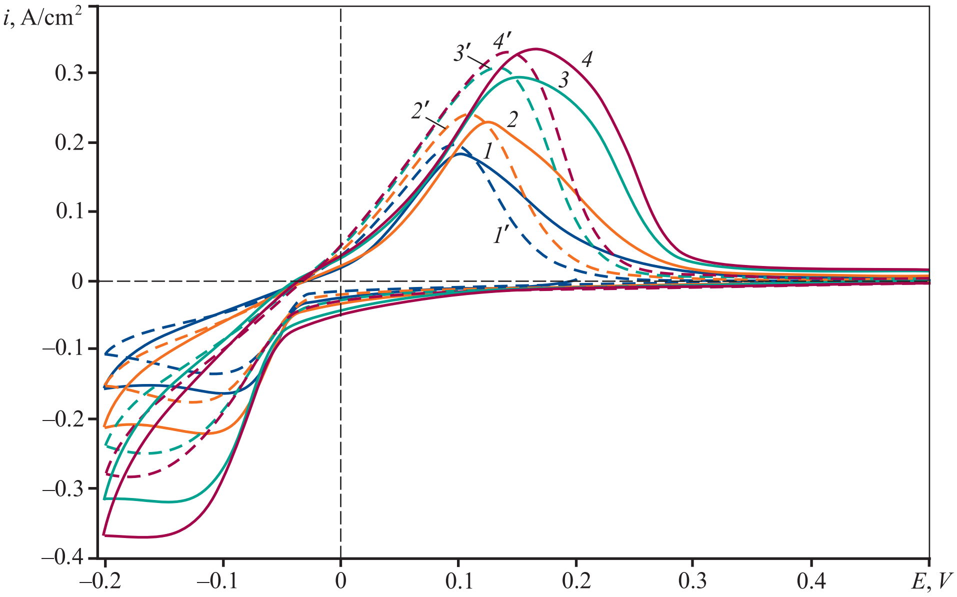

Fig. 2. Current voltage dependencies obtained on glassy carbon at 750 °C in 66.5KF–33.3KCl–0.23K_2SiF_6 (***1–4***) and 65.2KF–32.6KCl–2.0KI–0.23K_2SiF_6 (***1′–4′***) melts (mol.%)

Potential scanning rate, V/s: ***1***, ***1′*** – 0.1; ***2***, ***2′*** – 0.2; ***3***, ***3′*** – 0.4; ***4***, ***4′*** – 0.7

Рис. 2. Вольт-амперные зависимости, полученные на стеклоуглероде при температуре 750 °C в расплавах (мол.%) 66,5KF–33,3KCl–0,23K_2SiF_6 (***1–4***) и 65,2KF–32,6KCl–2,0KI–0,23K_2SiF_6 (***1′–4′***)

Скорость развертки потенциала, В/с: ***1***, ***1′*** – 0,1; ***2***, ***2′*** – 0,2; ***3***, ***3′*** – 0,4; ***4***, ***4′*** – 0,7

The dependencies display a distinct cathode peak and an anode peak, indicating the electroreduction of silicon ions and the oxidation of electrodeposited silicon, respectively. The presence of a single cathode peak suggests that the cathodic process occurs in a single stage: $Si^{4+} + 4e^- = Si^0$. The non-symmetry of the anode peak suggests a two-stage oxidation of silicon, involving the oxidation of silicon to various electroactive ions and the sluggish diffusion of silicon-containing ions within the electrode vicinity. As the scanning rate increases, the peak potential of the cathode current density shifts towards the negative region. This behavior is typical for electrochemical reactions following a mechanism of quasi-reversible or irreversible electrochemical processes. Furthermore, at potentials more negative than –0.2 V, a distinct wave is observed, indicating the initiation of electroreduction of potassium cations.

Similar trends were observed in the KF—KCl—K_2SiF_6 melt with the addition of 2 mol.% KI, indicating that the underlying mechanism of the process remains unchanged. However, some differences were observed in the current-voltage dependencies obtained with the addition of KI. These differences include lower cathode currents and narrower anode peaks, indicating alterations in the kinetics of anodic dissolution of silicon. The reduction in cathode current can be attributed to a change in the wetting angle between the glassy carbon electrode and the melt upon the addition of potassium iodide. This change is likely caused by modifications in the interfacial tension

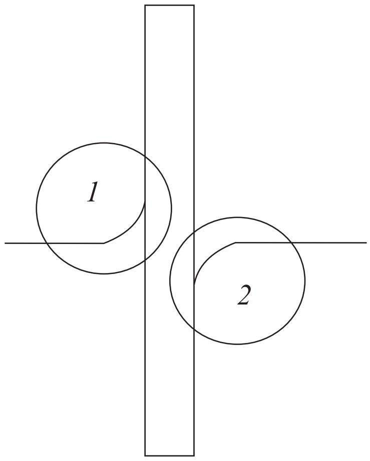

Fig. 3. Changes in meniscus shape upon KI addition to KF–KCl–K_2SiF_6 melt

1 – w/o KI; ***2*** – 2 mol.% KI

Рис. 3. Схематическое отображение изменения формы мениска при добавлении KI в расплав KF–KCl–K_2SiF_6

1 – без KI; ***2*** – 2 мол.% KI

at the boundary between the glass carbon electrode and the KF—KCl—K_2SiF_6 melt due to the presence of KI. It should be noted that the influence of KI may primarily affect the surface of the working glass carbon electrode rather than directly affecting the cathode current. This effect is illustrated schematically in Fig. 3.

Analysis of KI influence. In order to consider the impact of the meniscus formed during polarization on the three-phase boundary between the electrode, melt, and atmosphere, current-voltage dependencies were obtained with varying immersions of the working electrode into the melt. The goal was to account for the actual surface area of electrode-electrolyte contact affected by the presence of the melt meniscus. The measurement error associated with the true electrode surface area was estimated based on the cathode peak currents using the following equations:

$$I_1/(S_1 + \Delta S) = I_2/(S_2 + \Delta S) = I_3/(S_3 + \Delta S), \quad (1)$$

$$\Delta S = (I_1S_2 - I_2S_1)/(I_2 - I_1) =$$
$$= (I_1S_3 - I_3S_1)/(I_3 - I_1) = (I_2S_3 - I_3S_2)/(I_3 - I_2), \quad (2)$$

where I_1, I_2, I_3 represent the currents of the cathode peak corresponding to electrode submersions of 5, 10 and 15 mm, respectively, A; S_1, S_2, S_3 denote the measured working surface areas of the electrode at the same submersions, cm^2; ΔS represents the measurement error of the true electrode surface area caused by the occurrence of the melt meniscus at the three-phase boundary, cm^2.

Figure 4 depicts the current density of the cathode peaks as a function of the potential scanning rates for different submersions of the glass carbon electrode. When the electrode is submerged to a depth of 5 mm in the KF—KCl—K_2SiF_6 melt without KI, the peak of the cathode current density, taking into account the measurement error ΔS, is at its maximum. However, the peak decreases as the depth of electrode submersion increases. Conversely, in the presence of 2 mol.% KI, the trend is reversed. This suggests that the addition of KI leads to a decrease in the wetting angle of the glassy carbon electrode, as illustrated in Fig. 3.

The analysis based on Equations (1) and (2) indicates relative changes in the true surface area of the working electrode due to the formation of a melt meniscus during polarization. For the KF—KCl—K_2SiF_6 melt the estimated relative change is +12.9 %, while for the same melt with the addition of 2 mol.% KI, the relative change is –10.9 %. These calculations were performed under equivalent conditions. Considering the wetting phenomena, the actual peaks of cathode current density in the KF—KCl—K_2SiF_6 melt with and without 2 mol.% KI differ by 9 % (as shown in Fig. 4), which falls within the range of measurement error. Therefore, based on the voltammetry measurements, it can be concluded that the addition of 2 mol.% KI does not significantly affect the rate of silicon electrodeposition. However, it is worth noting that KI may exert a more noticeable influence on the formation of silicon nuclei, which, in turn, can impact the morphology of the deposited material.

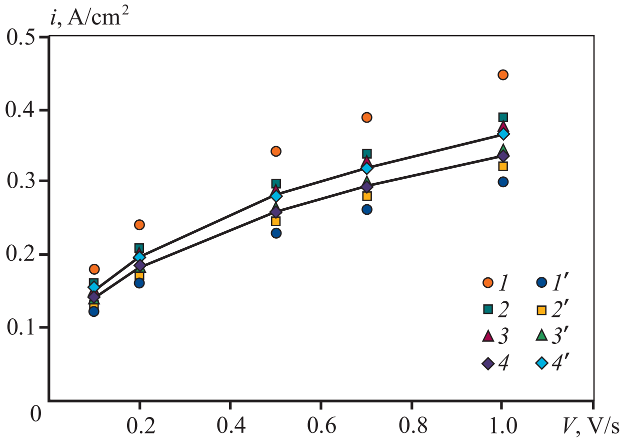

Fig. 4. Current density of cathode peaks as a function of potential scanning rate with various immersions (***1***, ***1′*** – 5 mm; ***2***, ***2′*** – 10 mm; ***3***, ***3′*** – 15 mm; ***4***, ***4′*** – calculated with accounting for ΔS) of glassy carbon in KF–KCl–K_2SiF_6 melt with addition of 2 mol.% KI (***1′***–***4′***) and without it (***1***–***4***)

Рис. 4. Зависимости плотности тока катодных пиков от скорости развертки потенциала при разных погружениях (***1***, ***1′*** – 5 мм; ***2***, ***2′*** – 10 мм; ***3***, ***3′*** – 15 мм; ***4***, ***4′*** – рассчитанные с учетом ΔS) стеклоуглеродного электрода в расплаве KF–KCl–K_2SiF_6 с добавкой 2 мол.% KI (***1′***–***4′***) и без нее (***1***–***4***)

Electrodeposition of silicon from KF—KCl—KI—K_2SiF_6 melts. The effect of iodide addition on the morphology of silicon deposits during electrodeposition from KF—KCl—K_2SiF_6 melt was investigated. The experiments were conducted using melts without KI, as well as with the addition of 2 and 4 mol.% KI. The electrolysis was performed at a temperature of 750 °C, using galvanostatic mode with glassy carbon plates prepared in a similar manner as the cathodes. The cathode current density was set at 0.02 A/cm^2, and the electrolysis duration was 120 minutes.

Figure 5 presents SEM-images of the obtained silicon deposits. In the melt without KI, the deposits appear as

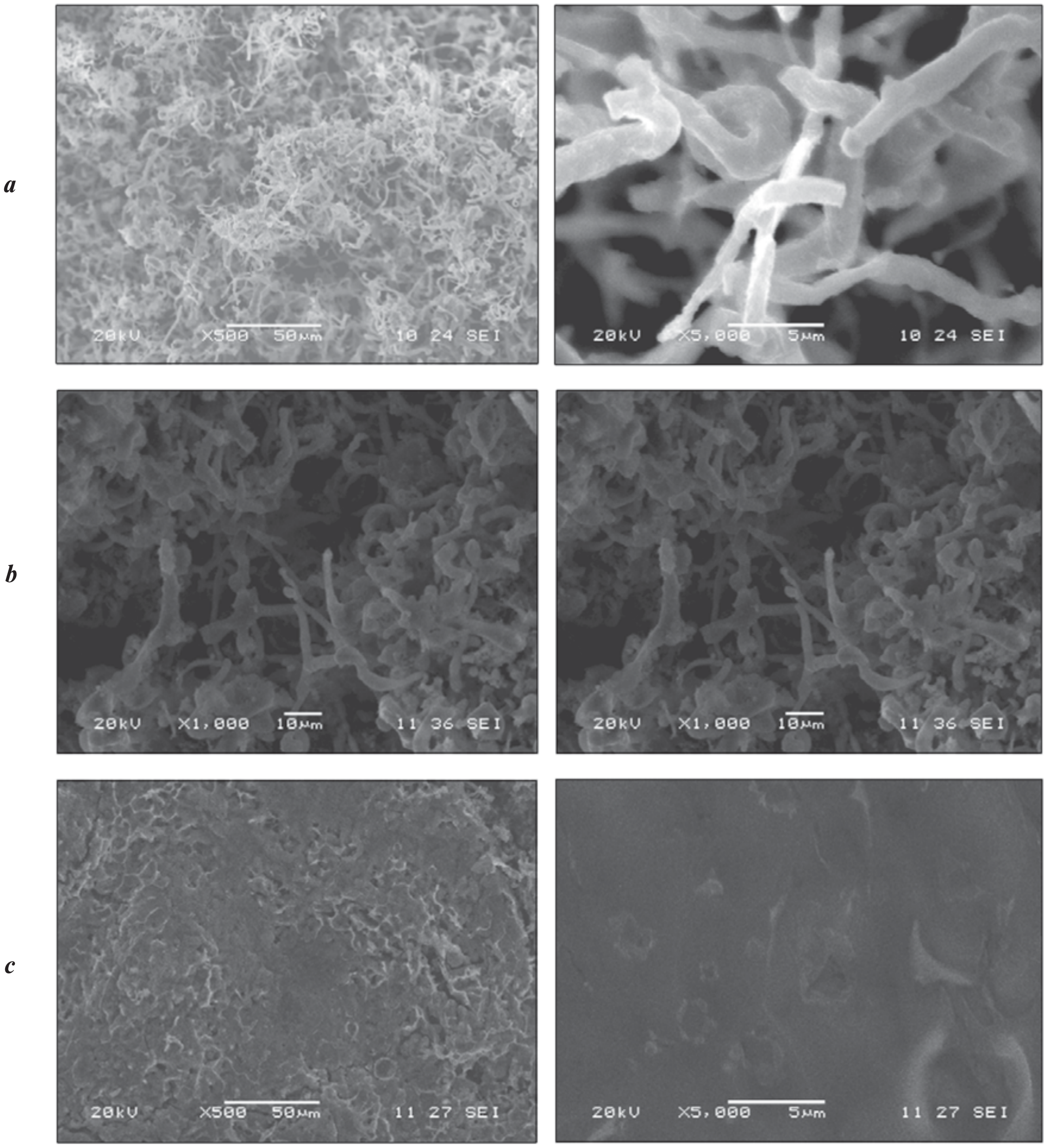

Fig. 5. SEM-images of silicon deposits obtained upon electrolysis of KF–KCl–K_2SiF_6 melt on glassy carbon at cathode current density of 0.02 A/cm^2 and at 750 °C

KI content, mol. %: ***a*** – 0; ***b*** – 2; ***c*** – 4

Рис. 5. Микрофотографии осадков кремния, полученных при электролизе расплава KF–KCl–K_2SiF_6 на стеклоуглероде при катодной плотности тока 0,02 А/см^2 и температуре 750 °C

Содержание KI, мол.%: ***a*** – 0; ***b*** – 2; ***c*** – 4

fibers with arbitrary shapes, having an average diameter of 1—2 μm. Upon adding potassium iodide in amounts of 2 and 4 mol.% to the melt, the silicon fibers agglomerate, resulting in the formation of solid silicon deposits. Energy dispersion analysis of the deposits revealed the presence of silicon and oxygen, with the oxygen content reaching up to 5 wt.% in terms of silicon dioxide. *X*-ray phase analysis of the deposits yielded similar results (see Fig. 6).

The findings from the electrochemical measurements and experiments on silicon electrodeposition highlight the significant influence of iodide on the morphology of silicon deposits. Specifically, with the addition and increased concentration of iodide in the melt, a smoothing

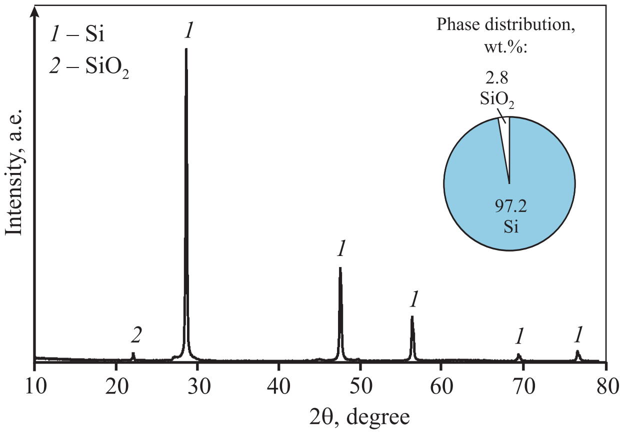

Fig. 6. Diffraction pattern of typical silicon deposit obtained upon electrolysis of KF–KCl–K_2SiF_6 melt with KI addition

Рис. 6. Дифрактограмма типичного осадка кремния, полученного при электролизе расплава KF–KCl–K_2SiF_6 с добавкой KI

effect on the deposit can be expected, assuming all other conditions remain constant.

Conclusions

The influence of potassium iodide (KI) as a surfactant on the kinetics of electroreduction of silicon ions and the morphology of silicon deposits on a glassy carbon cathode was studied using voltammetry, galvanostatic electrolysis, and scanning electron microscopy. The research was conducted in a 66.5KF—33.3KCl—0.23K_2SiF_6 melt (mol.%) at a temperature of 750 °C.

The results demonstrated that the addition of 2 mol.% KI to the KF—KCl—K_2SiF_6 melt alters the interfacial tension at the boundary between the glassy carbon electrode, melt, and environment. This leads to a decrease in the wetting of the glassy carbon electrode by the melt, resulting in a reduction in the actual working surface area and cathode current while maintaining current density. By accounting for this impact and estimating the influence of the melt meniscus shape, it was concluded that the addition of KI does not significantly affect the kinetics of the cathode process. During the electrolysis of the KF—KCl—K_2SiF_6 melt, fibrous silicon deposits with arbitrary shapes are formed on the glass carbon cathode. However, the addition of 2 and 4 mol.% KI to the melt causes the silicon deposits to agglomerate and become smoother under equivalent electrolysis conditions (cathode current density: 0.02 A/cm^2, electrolysis duration: 2 hours.

These findings indicate the possibility of adjusting the morphology of electrodeposited silicon, which can be advantageous for specific applications in various fields.

References

1. Nemchinova N.V., Buzikova T.A. Study of the phase-and-chemical composition of silicon production furnace slags. *Izvestiya. Non-Ferrous Metallurgy*. 2017;(1):31—39. (In Russ.).
https://doi.org/10.17073/0021-3438-2017-1-31-39
Немчинова Н.В., Бузикова Т.А. Исследование фазового состава печных шлаков кремниевого производства. *Известия вузов. Цветная металлургия*. 2017;(1):31—39.
2. Timofeev P.A., Timofeev A.N. Thermodynamic assessment of capability for deposition of silicon borides from their halogenides. *Powder Metallurgy and Functional Coatings*. 2017;(1): 58—63. (In Russ.).
https://doi.org/10.17073/1997-308X-2017-1-58-63
Тимофеев П.А., Тимофеев А.Н. Термодинамическая оценка возможности осаждения боридов кремния из их галогенидов. *Известия вузов. Порошковая металлургия и функциональные покрытия*. 2017;1:58—63.
3. Gevel T., Zhuk S., Leonova N., Leonova A., Trofimov A., Suzdaltsev A., Zaikov Yu. Electrochemical synthesis of nano-sized silicon from KCl—K_2SiF_6 melts for powerful lithium-ion batteries. *Applied Sciences*. 2021;11(22): 10927. https://doi.org/10.3390/app112210927
4. Wang F., Li P., Li W., Wang D. Electrochemical synthesis of multidimensional nanostructured silicon as a negative electrode material for lithium-ion battery. *ACS Nano*. 2022;16:7689—7700.
https://doi.org/10.1021/acsnano.1c11393
5. Suzdaltsev A.V. Silicon electrodeposition for microelectronics and distributed energy: a mini-review. *Electrochem*. 2022;3(4):760—768.
https://doi.org/10.3390/electrochem3040050
6. Dong Y., Slade T., Stolt M.J., Li L., Girard S.N., Mai L., Jin S. Low-temperature molten-salt production of silicon nanowires by the electrochemical reduction of $CaSiO_3$. *Angewandte Chemie*. 2017;129:14645—14649.
https://doi.org/10.1002/ange.201707064
7. Zou X., Ji L., Yang X., Lim T., Yu E.T., Bard A.J. Electrochemical formation of a p-n junction on thin film silicon deposited in molten salt. *Journal of American Chemical Society*. 2017;139:16060—16063.
https://doi.org/10.1021/jacs.7b09090
8. Zaykov Y.P., Zhuk S.I., Isakov A.V., Grishenkova O.V., Isaev V.A. Electrochemical nucleation and growth of

silicon in the KF—KCl—K_2SiF_6 melt. *Journal of Solid State Electrochemistry.* 2015;19:1341—1345. https://doi.org/10.1007/s10008-014-2729-z

9. Zhuk S.I., Gevel T.A., Zaikov Yu.P. Effect of the substrate material on kinetics and mechanism of electrodeposition from the KCl—KF—K_2SiF_6 melt. *Rasplavy.* 2021;(4): 354—364. (In Russ.). https://doi.org/10.31857/S0235010621040101
Жук С.И., Гевел Т.А., Зайков Ю.П. Влияние материала подложки на кинетику и механизм электроосаждения кремния из расплава KCl—KF—K_2SiF_6. *Расплавы.* 2021;(4):354—364.
10. Yasuda K., Maeda K., Hagiwara R., Homma T., Nohira T. Silicon electrodeposition in a water-soluble KF—KCl molten salt: Utilization of $SiCl_4$ as Si source. *Journal of the Electrochemical Society.* 2017;164:D67—D71. https://doi.org/10.1149/2.0641702jes
11. Padamata S.K., Saevarsdottir G. Silicon electrowinning by molten salts electrolysis. *Fronties in Chemistry.* 2023;11:1133990. https://doi.org/10.3389/fchem.2023.1133990
12. Parasotchenko Yu.A., Pavlenko O.B., Suzdaltsev A.V., Zaikov Yu.P. Electrochemical nucleation of silicon in the low-temperature LiCl—KCl—CsCl—K_2SiF_6 melt. *Journal of the Electrochemical Society.* 2023;170(2):022505. https://doi.org/10.1149/1945-7111/acbabf
13. Gevel T., Zhuk S., Suzdaltsev A.V., Zaikov Yu.P. Study into the possibility of silicon electrodeposition from a low-fluoride KCl—K_2SiF_6 melt. *Ionics.* 2022;28:3537—3545. https://doi.org/10.1007/s11581-022-04573-9
14. Pavlenko O.B., Ustinova Yu.A., Zhuk S.I., Suzdaltsev A.V., Zaikov Yu.P. Silicon electrodeposition from low-melting LiCl—KCl—CsCl melts. *Russian Metallurgy (Metally).* 2022;(8):818—824. https://doi.org/10.1134/S0036029522080109
Павленко О.Б., Устинова Ю.А., Жук С.И., Суздальцев А.В., Зайков Ю.П. Электроосаждение кремния из расплавов на основе легкоплавкой системы LiCl—KCl—CsCl. *Расплавы.* 2022;(1):49—60.
15. Savchenkov S.A., Bazhin V.Y., Brichkin V.N., Kosov Y.I., Ugolkov V.L. Production features of magnesium-neodymium master allot synthesis. *Metallurgist.* 2019;63(3-4): 394—402. https://doi.org/10.1007/s11015-019-00835-6
Савченков С.А., Бажин В.Ю., Бричкин В.Н., Косов Я.И., Уголков В.Л. Технологические особенности синтеза лигатур магний—неодим. *Металлург.* 2019;(4):71—77.
16. Morachevskii A.G. Physicochemical studies of utilization of lead batteries. *Russian Journal of Applied Chemistry.* 2014;87(3):241—257. https://doi.org/10.1134/S107042721403001X
Морачевский А.Г. Физико-химические исследования процессов утилизации свинцовых аккумуляторов (Обзор). *Журнал прикладной химии.* 2014;87(3): 273—290.
17. Shurov N.I., Khramov A.P., Zaikov Yu.P., Kovrov V.A., Suzdaltsev A.V. Reduction mechanism of oxides in calcium chloride melts. *Russian Journal of Non-Ferrous Metals.* 2015;56:267—271. https://doi.org/10.3103/S1067821215030207
Шуров Н.И., Храмов А.П., Зайков Ю.П., Ковров В.А., Суздальцев А.В. О механизме восстановления оксидов в расплавах хлорида кальция. *Известия вузов. Цветная металлургия.* 2015;(2):14—19.
18. Yasinsky A.S., Polyakov P.V., Klyuchantsev A.B. Anode gas dynamics in high-temperature cryolite melt-alumina slurry. *Izvestiya. Non-Ferrous Metallurgy.* 2017;(1):13—18. (In Russ.). https://doi.org/10.17073/0021-3438-2017-1-13-18
Ясинский А.С., Поляков П.В., Ключанцев А.Б. Динамика движения анодного газа в высокотемпературной суспензии «криолитовый расплав-глинозем». *Известия вузов. Цветная металлургия.* 2017;(1):13—18.
19. Sizyakov V.M., Bazhin V.Yu., Vlasov A.A., Feshchenko R.Yu., Khrapkova A.N. On interdependence of alumina charge with cryolite-alumina melt. *Izvestiya. Non-Ferrous Metallurgy.* 2014;(3):24—28. (In Russ.). https://doi.org/10.17073/0021-3438-2014-3-24-28
Сизяков В.М., Бажин В.Ю., Власов А.А., Фещенко Р.Ю., Храпкова А.Н. О взаимодействии глиноземной шихты с криолитоглиноземным расплавом. *Известия вузов. Цветная металлургия.* 2014;(3):24—28.
20. Zaikov Yu., Batukhtin V., Shurov N., Suzdaltsev A. High-temperature electrochemistry of calcium. *Electrochemical Materials & Technologies.* 2022;1(1):20221007. https://doi.org/10.15726/elmattech.2022.1.007
21. Trofimova T.S., Darintseva A.B., Ostanina T.N., Rudoi V.M., Il'ina I.E. Effect of the structure and morphology of Ni-based porous deposits on their electrocatalytic activity towards hydrogen evolution reaction. *Powder Metallurgy and Functional Coatings.* 2021;15(4):57—67. (In Russ.). https://doi.org/10.17073/1997-308X-2021-4-57-67
Трофимова Т.С., Даринцева А.Б., Останина Т.Н., Рудой В.М., Ильина И.Е. Влияние структуры и морфологии пористых осадков на основе никеля на их электрокаталитические свойства при получении водорода. *Известия вузов. Порошковая металлургия и функциональные покрытия.* 2021;15(4):57—67.
22. Lebedev V.A., Polyakov V.V. Electrode processes in the production of microdispersed titanium powder by volumetric electrolytic reduction of its ions with sodium dissolved in the $BaCl_2$—$CaCl_2$—NaCl melt in the absence

of titanium halides in the initial melt. *Powder Metallurgy and Functional Coatings.* 2022;16(4):4—14. (In Russ.). https://doi.org/10.17073/1997-308X-2022-4-14
Лебедев В.А., Поляков В.В. Электродные процессы при получении микродисперсного порошка титана объемным электролитическим восстановлением его ионов натрием, растворенным в расплаве $BaCl_2$—$CaCl_2$—NaCl, в отсутствие галогенидов титана в исходном расплаве. *Известия вузов. Порошковая металлургия и функциональные покрытия.* 2022;16(4):4—14.

23. Nikitin V.S., Ostanina T.N., Kumkov S.I., Rudoy V.M., Ostanin N.I. Determination of the growth time period of loose zinc deposit using interval analysis methods. *Powder Metallurgy and Functional Coatings.* 2020;(1):11—21. (In Russ.). https://doi.org/10.17073/1997-308X-2020-11-21
Никитин В.С., Останина Т.Н., Кумков С.И., Рудой В.М., Останин Н.И. Определение периода наращивания рыхлого осадка цинка с использованием методов интервального анализа. *Известия вузов. Порошковая металлургия и функциональные покрытия.* 2020;(1):11—21.
24. Laptev M.V., Khudorozhkova A.O., Isakov A.V., Grishenkova O.V., Zhuk S.I., Zaikov Y.P. Electrodeposition of aluminum-doped thin silicon films from a KF—KCl—KI—K_2SiF_6—AlF_3 melt. *Journal of Serbian Chemical Society.* 2021;86):1075—1087. https://doi.org/10.2298/JSC200917065L
25. Abdurakhimova R.K., Laptev M.V., Leonova N.M., Leonova A.M., Schmygalev A.S., Suzdaltsev A.V. Electroreduction of silicon from the NaI—KI—K_2SiF_6 melt for lithium-ion power sources. *Chimica Techno Acta.* 2022;9(4):20229424. https://doi.org/10.15826/chimtech.2022.9.4.24
26. Isakov A., Laptev M., Khudorozhkova A., Grishenkova O., Zaikov Y., Khvostov S., Kinev E., Rychkov V. Neutron transmutation doping of thin silicon films electrodeposited from the KF—KCl—KI—K_2SiF_6 melt. *Journal of the Electrochemical Society.* 2020;167(8):082515. https://doi.org/10.1149/1945-7111/ab933c
27. Filatov A.A., Nikolaev A.Y., Suzdaltsev A.V., Zaikov Y.P. Extraction of zirconium from its oxide during the electrolysis of KF—AlF_3—Al_2O_3—ZrO_2 melts. *Russian Journal of Non-Ferrous Metals.* 2022;63(4):379—384. https://doi.org/10.3103/S106782122204006X
Филатов А.А., Николаев А.Ю., Суздальцев А.В., Зайков Ю.П. Извлечение циркония из его оксида при электролизе расплавов KF—AlF_3—Al_2O_3—ZrO_2. *Известия вузов. Цветная металлургия.* 2022;28(3):13—20. https://doi.org/10.17073/0021-3438-2022-3-13-20

Information about the authors

Sergey I. Zhuk – Junior Researcher of the Laboratory of Electrode Processes, Institute of High-Temperature Electrochemistry of Ural Branch of the Russian Academy of Sciences (IHTE UB RAS); Junior Researcher of the Laboratory of Electrochemical Devices and Materials, Ural Federal University n.a. the First President of Russia B.N. Eltsin (UrFU).
https://orcid.org/0000-0003-2889-7318
E-mail: ZhukSI83@mail.ru

Lyudmila M. Minchenko – Cand. Sci. (Chem.), Engineer of the Laboratory of Electrode Processes, IHTE UB RAS.
https://orcid.org/0000-0001-6067-5251
E-mail: l.minchenko@ihte.uran.ru

Andrey V. Suzdaltsev – Dr. Sci. (Chem.), Leading Researcher of the Laboratory of Electrode Processes, IHTE UB RAS; Head of the Laboratory of Electrochemical Devices and Materials, UrFU.
https://orcid.org/0000-0003-3004-7611
E-mail: suzdaltsev_av@ihte.uran.ru, a.v.suzdaltsev@urfu.ru

Информация об авторах

Сергей Иванович Жук – мл. науч. сотрудник лаборатории электродных процессов Института высокотемпературной электрохимии Уральского отделения Российской академии наук (ИВТЭ УрО РАН); мл. науч. сотрудник научной лаборатории электрохимических устройств и материалов Уральского федерального университета им. первого Президента России Б.Н. Ельцина (УрФУ).
https://orcid.org/0000-0003-2889-7318
E-mail: ZhukSI83@mail.ru

Людмила Михайловна Минченко – к.х.н., инженер лаборатории электродных процессов ИВТЭ УрО РАН.
https://orcid.org/0000-0001-6067-5251
E-mail: l.minchenko@ihte.uran.ru

Андрей Викторович Суздальцев – д.х.н., вед. науч. сотрудник лаборатории электродных процессов ИВТЭ УрО РАН; заведующий научной лабораторией электрохимических устройств и материалов УрФУ.
https://orcid.org/0000-0003-3004-7611
E-mail: suzdaltsev_av@ihte.uran.ru, a.v.suzdaltsev@urfu.ru

Andrey V. Isakov – Cand. Sci. (Chem.), Head of the Laboratory of Electrocrystallization and High-Temperature Electroplating, IHTE UB RAS.
https://orcid.org/0000-0002-0192-3048
E-mail: ihte_uran@mail.ru

Yuriy P. Zaikov – Dr. Sci. (Chem.), Prof., Scientific Supervisor of the IHTE UB RAS; Head of the Department of Technology of Electrochemical Production, UrFU.
https://orcid.org/0000-0001-6138-3955
E-mail: zaikov@ihte.uran.ru

Андрей Владимирович Исаков – к.х.н., заведующий лабораторией электрокристаллизации и высокотемпературной гальванотехники ИВТЭ УрО РАН.
https://orcid.org/0000-0002-0192-3048
E-mail: ihte_uran@mail.ru

Юрий Павлович Зайков – д.х.н., проф., научный руководитель ИВТЭ УрО РАН; заведующий кафедрой технологии электрохимических производств УрФУ.
https://orcid.org/0000-0001-6138-3955
E-mail: zaikov@ihte.uran.ru

Contribution of the authors

S.I. Zhuk – preparation of electrolytes, electrochemical measurements, electrodeposition, registration of the research results, participation in the writing of the article.

L.M. Minchenko – installation manufacturing, microscopic analysis, electrodeposition.

A.V. Suzdaltsev – definition the purpose of the work, writing the text of the article.

A.V. Isakov – discussion of the research results.

Yu.P. Zaikov – general management of research.

Вклад авторов

С.И. Жук – приготовление электролитов, электрохимические измерения, электроосаждение, оформление результатов исследований, участие в написании статьи.

Л.М. Минченко – изготовление установки, микроскопический анализ, электроосаждение.

А.В. Суздальцев – постановка цели работы, написание текста статьи.

А.В. Исаков – обсуждение результатов исследований.

Ю.П. Зайков – общее руководство исследованиями.

The article was submitted 14.02.2023, revised 03.04.2023, accepted for publication 07.04.2023

Статья поступила в редакцию 14.02.2023, доработана 03.04.2023, подписана в печать 07.04.2023

METALLURGY OF RARE AND PRECIOUS METALS / МЕТАЛЛУРГИЯ РЕДКИХ И БЛАГОРОДНЫХ МЕТАЛЛОВ

UDC 661.897
https://doi.org/10.17073/0021-3438-2023-3-27-37

Research article
Научная статья

Preparation of rhodium concentrate from gold cementate

Ya.D. Zelyakh[1], **R.S. Voinkov**[1,2], **K.L. Timofeev**[1,2], **G.I. Maltsev**[1]

[1] **JSC Uralelectromed**
1 Uspenskiy prosp., Verkhnyaya Pyshma, Sverdlovsk region, 624091, Russia

[2] **Technical University of Ural Mining and Metallurgical Company**
3 Uspenskiy prosp., Verkhnyaya Pyshma, Sverdlovsk region, 624091, Russia

✉ Yakov D. Zelyakh (zyad@elem.ru)

Abstract: This article describes studies on improving reprocessing technology gold production cementate (GPC) formed in refining section of chemical metallurgical shop at JSC Uralelektromed, in order to increase the extraction rate of targeted metals into marketable products, diversification of production, achievement of economic effect due to increasing content of precious metals (PM) in individual concentrates. The optimization of GPC reprocessing technology includes intensification of leaching of initial material and filtration of produced pulp, in order to increase the extraction of gold and platinum group metals (PGM) into solution and decrease the circulated PM. This would allow individual products (crude PM) to be obtained with minimum material loss and labor consumption. It is possible to increase rhodium content in concentrate and to reduce its circulation by preliminary oxidating annealing at the temperature above 500 °C. At this temperature hardly soluble trioxide Rh_2O_3 is formed on rhodium surface, insoluble in aqua regia, thus allowing it to deposit in the form of individual product. The influence of temperature and composition of gaseous phase was established upon oxidizing annealing of initial raw stuff ($t = 500 \div 750$ °C) on the composition of rhodium trioxide concentrate ($15 \div 45$ % Rh_2O_3). Reprocessing flowchart of gold production cementate was developed and tested on commercial scale, allowing for the simultaneous production of several products: deposited gold ($Au \geq 98$ %), deposited silver ($Ag \geq 98$ %), PGM concentrate ($Pt \geq 45$ % and $Pd \geq 15$ %), rhodium concentrate ($Rh = 15 \div 45$ %).

Keywords: precipitate of gold recovery, precipitation, precious metals, annealing, leaching, rhodium, concentrate of platinum group metals.

For citation: Zelyakh Ya.D., Voinkov R.S., Timofeev K.L., Maltsev G.I. Preparation of rhodium concentrate from gold cementate. *Izvestiya. Non-Ferrous Metallurgy*. 2023;29(3):27–37. https://doi.org/10.17073/0021-3438-2023-3-27-37

Получение концентрата родия из цементата золота

Я.Д. Зелях[1], **Р.С. Воинков**[1,2], **К.Л. Тимофеев**[1,2], **Г.И. Мальцев**[1]

[1] **АО «Уралэлектромедь»**
624091, Россия, Свердловская обл., г. Верхняя Пышма, Успенский пр-т, 1

[2] **Технический университет Уральской горно-металлургической компании**
624091, Россия, Свердловская обл., г. Верхняя Пышма, Успенский пр-т, 3

✉ Яков Дмитриевич Зелях (zyad@elem.ru)

Аннотация: Проведены исследования по совершенствованию технологии переработки цементата производства золота (ЦПЗ), образующегося в аффинажном отделении химико-металлургического цеха АО «Уралэлектромедь», с целью повышения степени извлечения целевых металлов в товарные продукты, диверсификации производства, получения экономического эффекта за счет увеличения содержания драгоценных металлов (ДМ) в индивидуальных концентратах. Оптимизация технологии переработки ЦПЗ предусматривает интенсификацию процессов выщелачивания исходного материала и фильтрации полученной пульпы для увеличения показателей извлечения в раствор золота, металлов платиновой группы (МПГ) и снижения находящихся в обороте ДМ, что позволит получить индивидуальные продукты (черновые ДМ) с минимальными материальными затратами и трудоемкостью. Повысить содержание родия в концентрате и сократить его количество в обороте при переработке цементата возможно путем предварительного окислительного обжига при температуре свыше 500 °С, при которой на поверхности родия образуется труднорастворимый триоксид Rh_2O_3, не растворяющийся в «царской водке», что позволяет выделить его в виде индивидуального продукта. Установлено влияние температуры и состава газовой фазы при проведении окислительного обжига исходного сырья ($t = 500\div750$ °С) на состав концентрата триоксида родия ($15\div45$ % Rh_2O_3). Разработана и опробована в промышленном варианте схема переработки цементата производства золота, которая позволяет селективно получить несколько продуктов: осажденное золото (Au ≥ 98 %), осажденное серебро (Ag ≥ 98 %), концентрат МПГ (Pt ≥ 45 % и Pd ≥ 15 %), концентрат родия (Rh = 15÷45 %).

Ключевые слова: цементат производства золота, цементация, драгоценные металлы, обжиг, выщелачивание, родий, концентрат металлов платиновой группы.

Для цитирования: Зелях Я.Д., Воинков Р.С., Тимофеев К.Л., Мальцев Г.И. Получение концентрата родия из цементата золота. *Известия вузов. Цветная металлургия*. 2023;29(3):27–37. https://doi.org/10.17073/0021-3438-2023-3-27-37

Introduction

The content of platinum metals in Ural ores is not high, although at least 97 % of platinoids is extracted from initial raw stuff to anode copper. In the technological circuit of copper production at OAO UMMC, platinoids comprised in crude copper are supplied to AO Uralelektromed. The head enterprise of the company is one of the largest copper refineries in Russia constantly upgrading its technology. In the course of copper electric refining, mud is generated containing precious metals (PM), %: 0.35—0.48 Au, 8.66—11.31 Ag, 0.002—0.004 Pt, 0.025—0.052 Pd, 0.0009—0.0025 Rh [1—3]. Subsequently, PM are concentrated in silver gold alloy (SGA) which is transferred to refining [4—8]. Figure 1 illustrates the technological flowchart of SGA reprocessing at AO Uralelektromed. The products of refining are gold and silver in ingots, as well as platinum group meals concentrate (PGMC) in the form of cathode residue and powder (PGMC-CR and PGMC-P, respectively).

The growing consumption of platinum group metals (PGM) together with increase in their price has led to increasing interest to studies of selective production of refined platinum metals, including the possibility of selective extraction of platinum metals from multicomponent technogenic raw stuff as exemplified by gold production cementate (GPC) [9—13].

The gold production cementate is formed in refining section of chemical metallurgical shop upon PM recovery by metal containing materials from waste solution of recycling gold deposition and PGMC powder, as well as washing waters of dust and gas capturing system of melting stage. The content of main GPC components, % is as follows: 12—30 Au, 2—6 Ag, 14—32 Pt, 5—15 Pd, 2—8 Rh, 25—35 impurities. Impurities in GPC are presented by Cu, Se, Te, Fe and S in amounts up to 10 % each, as well as by other components [14—17].

In order to increase extraction of valuable component and complexity of use of formed process products, GPC is reprocessed both with the collective extraction of impurities and with the selective extraction of precious metals [18; 19]. The composition of the products obtained and efficiency of their extraction depend, in particular, on the nature and properties of solvent [20—22]. The production of individual products of high purity is accompanied by numerous stages of repurification and complexity of the process hardware [23]. AO Uralelektromed currently operates the following flowchart of GPC reprocessing (Fig. 2).

The higher duration (from 4 to 6 h) of cementate dissolution stage should be mentioned. It is directly proportional to the content of non-precious metals: this is accompanied by a decrease in the specifications of direct extraction of metals to targeted products (up to 50 % Au, 40 % Pt, 60 % Pd). It is also interrelated with the long-term filtration of pulp after GPC dissolution in aqua regia solution (from 0.5 to 2 h) due to amorphous structure of the material.

The qualitative phase analysis of the initial cementate is illustrated in Fig. 3. While studying phase structure of the material considered, the possibility of existence of amorphous phases was established (halo with the central point $2\theta \sim 46.89°$) — up to 36 %, stipulated by scatter from unordered phases. The expressed

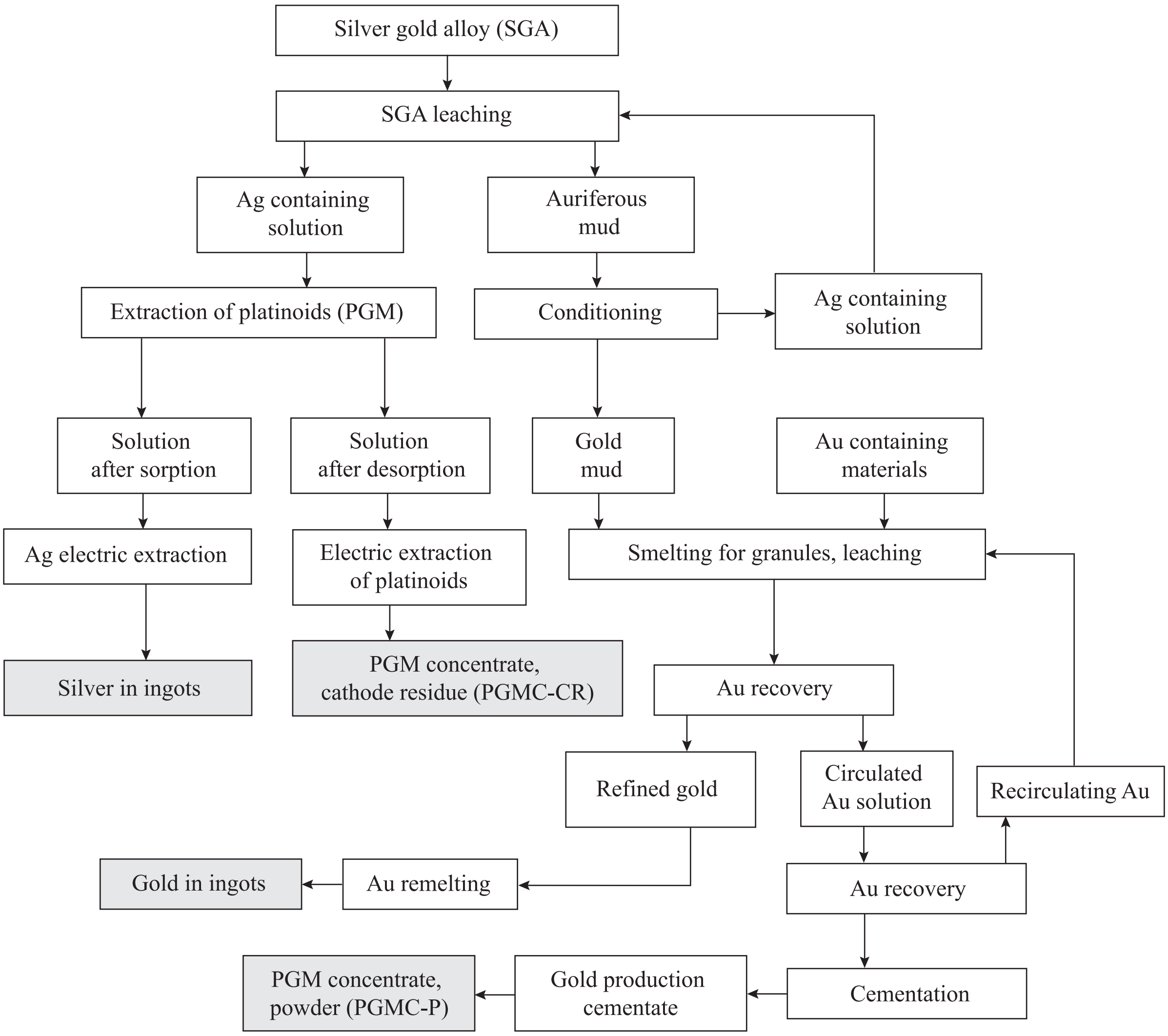

Fig. 1. Flowchart of PM refining at AO Uralelektromed

Рис. 1. Принципиальная схема аффинажа ДМ в АО «Уралэлектромедь»

lines in the diffraction pattern are probably referred to AgAu.

The optimization of GPC reprocessing technology stipulates for oxidizing annealing, leading to intensification of leaching of initial material and filtration of obtained pulp aimed at improving extraction of gold and PGM into solution and decrease in the content of recycling precious metals, thus allowing individual products to be obtained (crude PM), as well as to diversify the production process (production of rhodium concentrate).

According to the existing technology, rhodium is distributed between insoluble residue after GPC leaching (~40 % Rh are extracted) and concentrate of platinoid in the form of powder (PGMC-P, ~60 % Rh) obtained by cementation. Rhodium content in the concentrate is 2—8 %. Rhodium content in PGMC powder can be increased and its recirculating content can be reduced upon GPC reprocessing by preliminary oxidizing annealing at a temperature above 500 °C. At this temperature hardly soluble trioxide Rh_2O_3 is formed on rhodium surface, insoluble in aqua regia, thus allowing it to be deposited in the form of individual product [24—29].

The aim of this work was to improve the reprocessing technology of cementate of gold production including additional production of crude metals (silver: Ag ≥ 98 %, rhodium concentrate: Rh = 15÷45 %) with retention of gold quality (Au ≥ 98 %) and PGM concentrate (Pt ≥ 45 % and Pd ≥ 15 %).

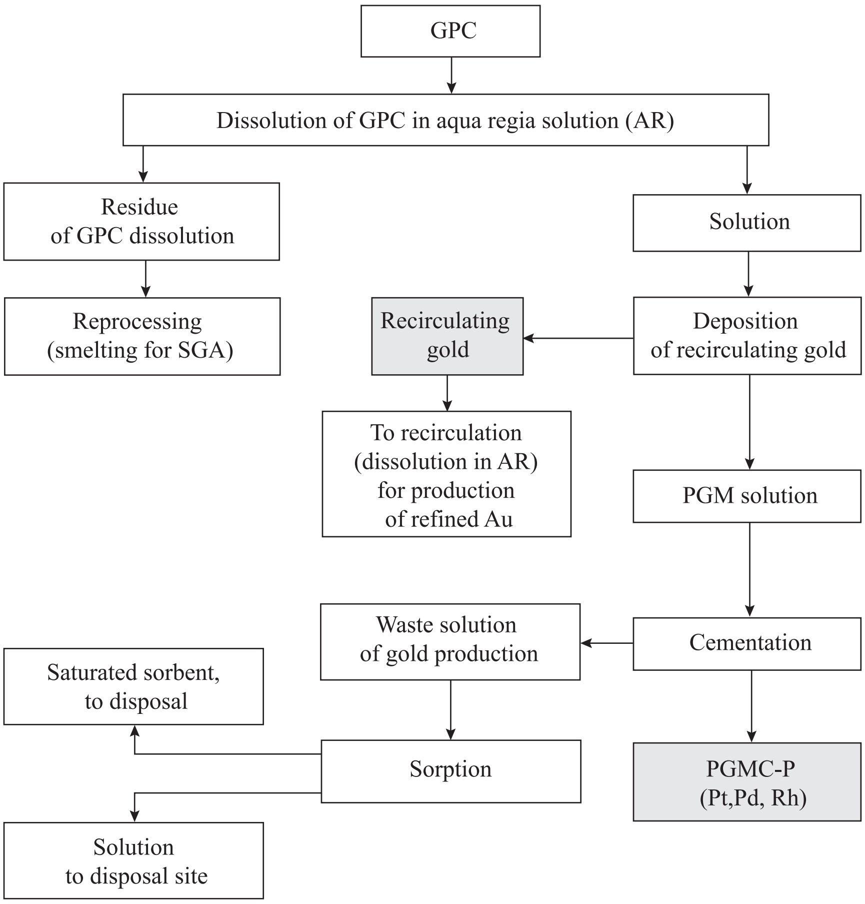

Fig. 2. Existing flowchart of GPC reprocessing

Рис. 2. Принципиальная существующая схема переработки ЦПЗ

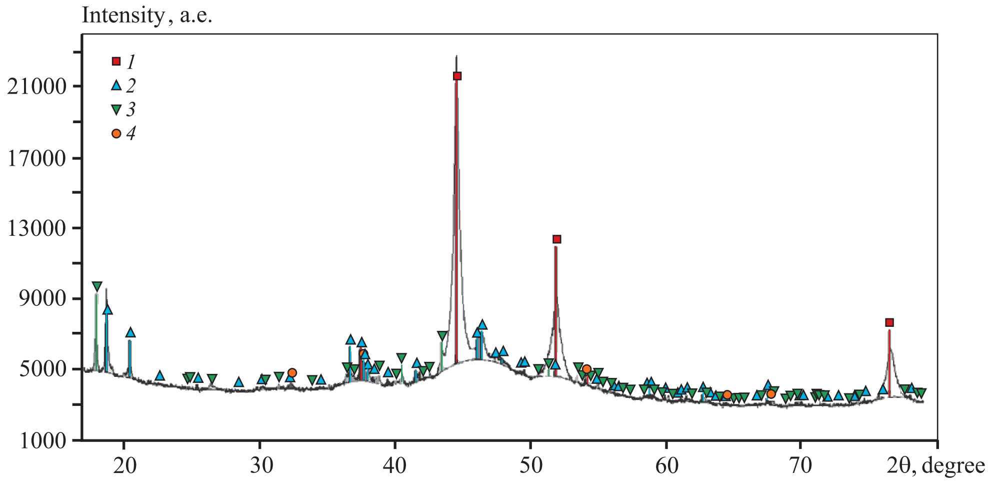

Fig. 3. Qualitative phase analysis of initial GPC
(DiffracSuite EVA v6.0; ICDD PDF-2 2019, diffraction pattern fragment)

1 – AuAg; ***2*** – atacamite $Cu_2Cl(OH)_3$; ***3*** – botallackite $Cu_2(OH)_3Cl$; ***4*** – chlorargyrite AgCl

Рис. 3. Качественный фазовый анализ пробы «ЦПЗ исходный»
(DiffracSuite EVA v6.0; ICDD PDF-2 2019, фрагмент дифрактограммы)

1 – AuAg; ***2*** – атаканит $Cu_2Cl(OH)_3$; ***3*** – боталлакит $Cu_2(OH)_3Cl$; ***4*** – хлораргирит AgCl

Experimental

In order to estimate the possibility of production of concentrate with a higher rhodium content, a series of experiments were carried out according to the improved flowcharts illustrated in Fig. 4.

The experiments differed in the conditions of oxidizing annealing (Table 1). Annealing in test *1* was carried out in a laboratory muffle furnace and compared with the data on reprocessing of initial material (test *1.1*, see Table 2). Tests *2*, *3* were carried out under industrial conditions: electric furnace of indirect heating; material layer height not more than 2 cm. The parameters of other technological procedures were identical.

GPC leaching after annealing was carried out in laboratory and commercial reactors at 85—95 °C and L : S = 5 mixture of acids with the following composition, vol.% : 85—95 HCl, 5—15 HNO_3.

The chemical analysis of process products was carried out using an inductively coupled Spectroblue plasma atomic emission spectrometer (Spectro Analytical Instruments, Germany). The final products were analyzed by atomic emission spectroscopy with spark emission of spectrum using a Spectrolab M12 (Germany) emission spectrometer.

Samples of the cementate and products of its annealing were also studied by *X*-ray phase analysis (XPA) using a Bruker D8 Advance diffractometer (Bruker Corp., USA) in the range of diffraction angles $2\theta = 15\div80°$ in $\text{Co}K_\alpha$-radiation with the increment of 0.025° using a LynxEye position sensitive detector. The total time of recording was 7.5 h, the equivalent time per step: 1860 s. The qualitative phase analysis was carried out using Bruker DiffracSuite EVA v6.0 software and database of reference diffraction spectra ICDD PDF-2 (v. 2019). The quantitative phase analysis was carried out in the Bruker TOPAS 5.0 full profile package according to Rietveld.The crystalline phases were taken from Crystallography Open Database (Cambridge university, Great Britain). Micro images of the

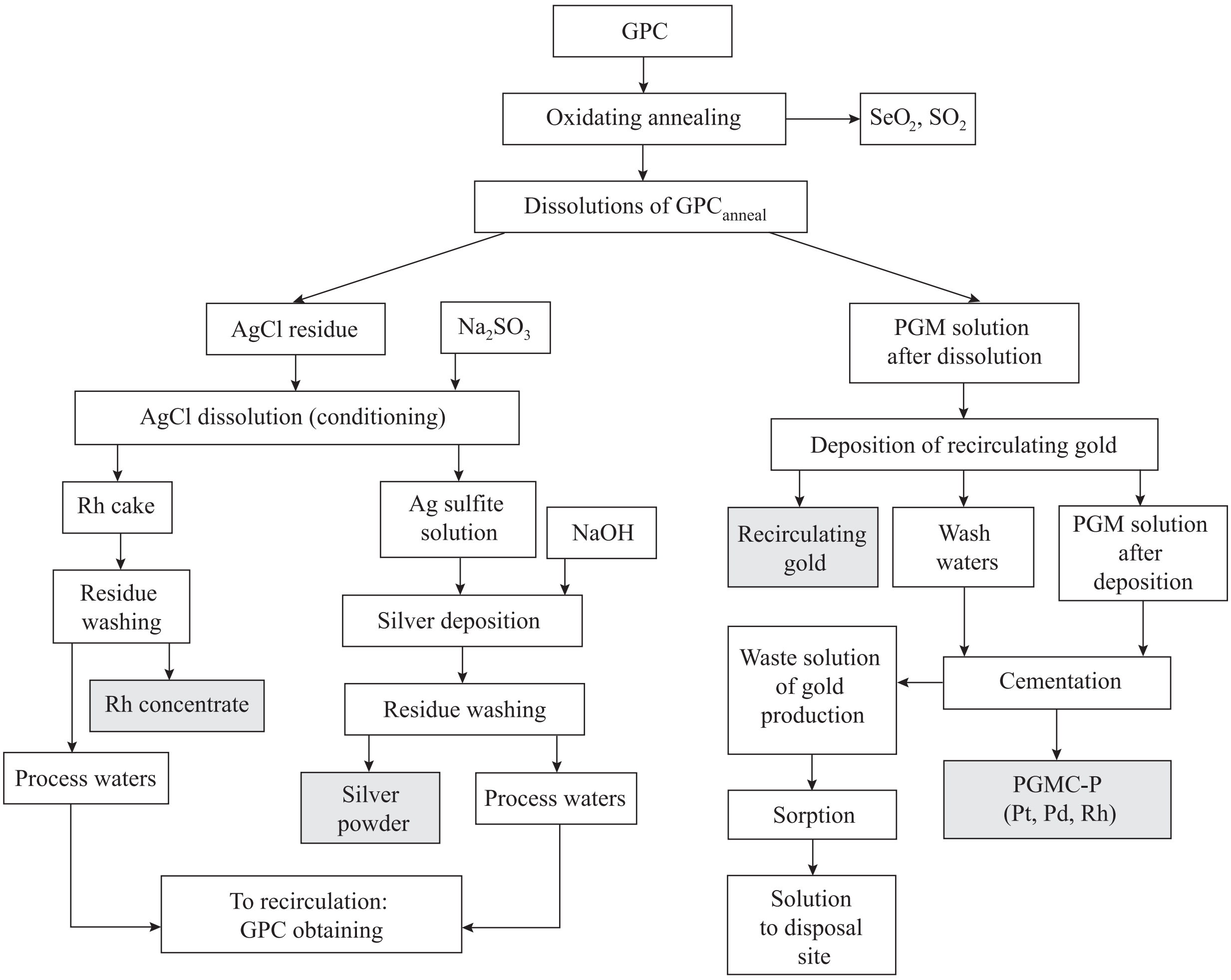

Fig. 4. Proposed flowchart of GPC reprocessing

Рис. 4. Предлагаемая технологическая схема переработки ЦПЗ

Table 1. **Technological parameters of GPC annealing**

Таблица 1. Технологические параметры обжига ЦПЗ

Test No.	*t*, °C	Duration, h	GPC weight, kg	Annealing conditions
1.1	–	–	0.2	Laboratory, w/o preliminary annealing
1	750	10–12	0.2	Laboratory, periodical air supply (0.05 n.m^3/h)
2	500	8–10	28.1	Industrial, pure oxygen supply (20 n.m^3/h)
3	620	24–30	20.7	Industrial, periodical air supply (5 n.m^3/h)
4	720	8–10	25.6	Industrial, pure oxygen supply (20 n.m^3/h)
5	720	12–14	21.5	Industrial, periodical air supply Industrial (5 n.m^3/h)

samples were obtained using a Tescan Vega electron microscope (Tescan, Czech Republic) with the magnification of $60^{\times}$ and $400^{\times}$.

Results and discussion

In the course of leaching of annealed materials both the duration of material dissolution and filtration duration of the pulps (Fig. 5) decrease by 50—70 %, related with variations in residue structure (Fig. 6, laboratory experiments). Despite the additional procedure of annealing with the duration of 8—16 h, the technology does not result in increase of unfinished production. This allows the number of repeated dissolutions to be reduced and up to 5 % of rhodium from circulation to be removed. Table 2 summarizes the leaching degrees of metals into solution in each experiment.

The qualitative phase analysis of GPC after annealing is illustrated in Fig. 6. Variations in the residue structure are observed, as evidenced by XPA data. According to the diffraction pattern, the formation of crystals was identified, and the fraction of amorphous phases significantly decreased. The results of *X*-ray spectral microanalysis also confirm the conclusions obtained. In comparison with the initial cementate (Fig. 7, *a*), the product after annealing (Fig. 7, *b*) demonstrates obviously distinguishable Mcalpineite crystals Cu_3TeO_6 formed as a result of oxidizing annealing. The possibility of crystal formation was demonstrated in [30]. Additional confirmation of the conclusions about variations of residue structure are the practical results of cementate filtrate rates, before and after annealing.

Neither the composition of gaseous phase (oxygen, air, or oxygen air mixture (OAM)), nor the mode of gas supply (0,05—20 n.m^3/h) exerted noticeable impact on

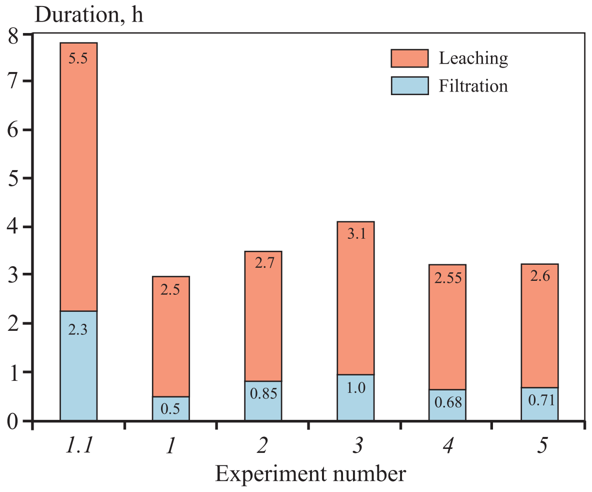

Fig. 5. Duration of leaching and filtration stages as a function of conditions of preliminary annealing

Рис. 5. Зависимость продолжительности стадий выщелачивания и фильтрации от условий предварительного обжига

Table 2. **Degree of metal leaching into solution, %**

Таблица 2. Степень выщелачивания металлов в раствор, %

Test No.	Au	Ag	Pt	Pd	Rh
1.1	80	9	77	74	62
1	99.99	4	86	82	30
2	99.99	3	99.99	99.99	50
3	99.99	1.5	88	72	34
4	99.99	2.6	95.7	86.2	32
5	99.99	1.8	96.4	90.1	33

the efficiency of rhodium oxidation, due to excessive content of oxidizer. The gas composition in commercial tests was stipulated by the technological features and parameters of the annealing furnaces involved. The efficiency of rhodium oxidation was influenced to the highest extent by the temperature: at $t = 750$ °C only 30 % Rh is dissolved. The significant difference in the degrees of PM extraction into solution is stipulated not only by the annealing temperature, but also by various content of metallic impurities (Cu, Te, Fe, Sb) in different batches of GPC, their influence will be estimated in further studies.

Excessive nitric acid was removed from the leaching solution by the addition of ethyl alcohol solution upon heating. Table 3 summarizes the compositions of recirculating gold and PGMC. The PM extraction (Au, Pt, Pd, Rh) from leaching solution to final products was more than 99 %.

The insoluble residue of GPC dissolution after an-

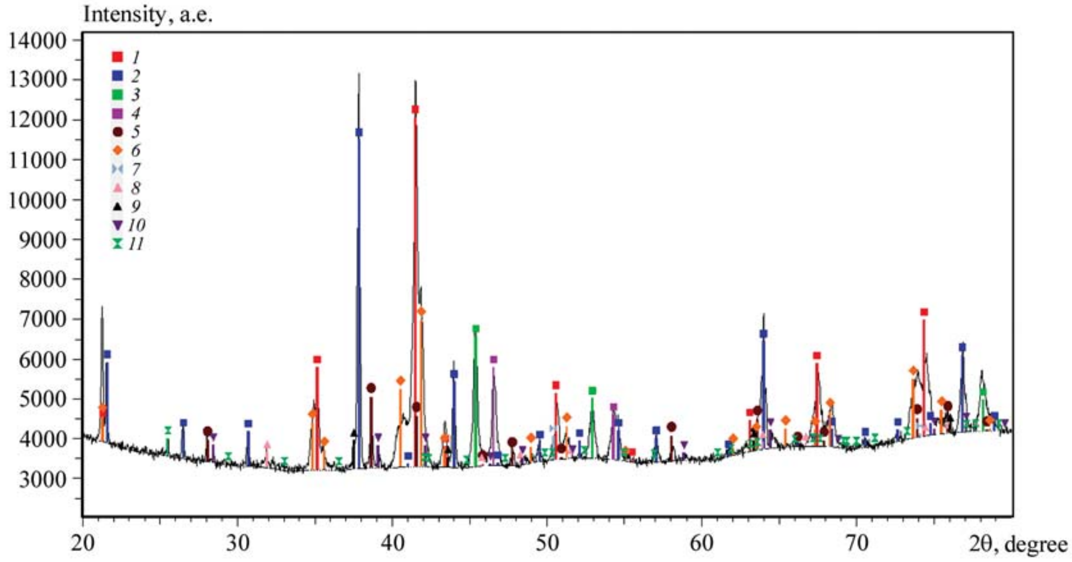

Fig. 6. Qualitative phase analysis of GPC after annealing
(DiffracSuite EVA v6.0; ICDD PDF-2 2019, diffraction pattern fragment)

Phases: ***1*** – iron manganate Fe_2MnO_4; ***2*** – copper nickel tellurium oxide $Cu_2Ni(TeO_6)$; ***3*** – $Au_{0.8}Cu_{0.2}$; ***4*** – platinum Pt; ***5*** – hematite Fe_2O_3; ***6*** – copper ferrite $CuFe_2O_4$; ***7*** – propatagium $Fe_{0.75}Pt_{0.25}$; ***8*** – rutile TiO_2; ***9*** – AgO; ***10*** – $(Cr_{0.88}Ti_{0.12})_2O_3$; ***11*** – cristobalite SiO_2

Рис. 6. Качественный фазовый анализ пробы «ЦПЗ после обжига»
(DiffracSuite EVA v6.0; ICDD PDF-2 2019, фрагмент дифрактограммы)

Фазы: ***1*** – манганат железа Fe_2MnO_4; ***2*** – медно-никелевый оксид теллура $Cu_2Ni(TeO_6)$; ***3*** – $Au_{0,8}Cu_{0,2}$; ***4*** – платина Pt; ***5*** – гематит Fe_2O_3; ***6*** – феррит меди $CuFe_2O_4$; ***7*** – ферроплатина $Fe_{0,75}Pt_{0,25}$; ***8*** – рутил TiO_2; ***9*** – AgO; ***10*** – $(Cr_{0,88}Ti_{0,12})_2O_3$; ***11*** – кристобалит SiO_2

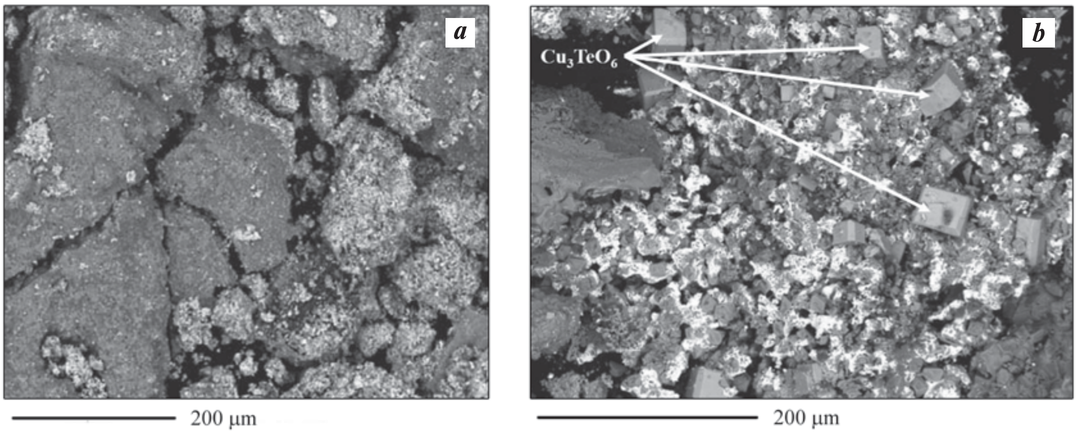

Fig. 7. GPC micro images before (***a***) and after (***b***) annealing

Рис. 7. Микрофотографии ЦПЗ до (***a***) и после (***b***) обжига

Table 3. **PM content (%) in recirculated gold and PGMC**

Таблица 3. Содержание ДМ (%) в золоте оборотном и КМПГ

Test No.	Au	Ag	Pt	Pd	Rh
1.1	99.6/0.46	0.022/1.01	0.017/32.53	0.029/11.5	0.045/9.12
1	99.3/–	0.020/0.005	0.178/46.15	0.199/22.70	0.001/2.10
2	98.9/0.012	0.257/0.720	0.234/38.80	0.010/15.12	0.010/3.10
3	99.4/0.056	0.015/0.329	0.045/48.13	0.105/19.79	0.000/2.52
4	98.6/0.021	0.153/0.56	0.184/45.7	0.095/20.1	0.011/2.15
5	99.01/0.015	0.104/0.43	0.078/44.5	0.102/19.97	0.009/2,42

Remark: numerator – recirculated gold, denominator – PGMC.

Table 4. **PM content in rhodium concentrate, %**

Таблица 4. Содержание ДМ в концентрате родия, %

Test No.	Rh	Au	Ag	Pt	Pd
1.1	8.4	0.1	0.15	3.5	2.8
1	45.00	0.15	0.250	1.17	0.58
2	20.08	1.07	0.543	3.96	6.16
3	15.10	0.54	5.200	1.600	11.7
4	40.25	0.96	1.2	1.512	8.92
5	37.89	0.85	1.08	2.08	9.07

Table 5. **PM content in silver residue, %**

Таблица 5. Содержание ДМ в осадке серебра, %

Test No.	Au	Ag	Pt	Pd	Rh
1.1	0.05	85.1	2.3	1.58	0.45
1	–	99.59	0.00	0.00	0.00
2	0.18	94.61	0.77	0.15	0.30
3	2.34	86.80	1.70	0.68	0.39
4	0.26	92.48	0.89	0.57	0.05
5	0.34	93.26	1.04	0.39	0.12

nealing in aqua regia is comprised mainly of silver chloride (AgCl) and rhodium oxide (Rh_2O_3). An increase in rhodium content in solid phase was achieved by leaching of insoluble residue by sodium sulfite. The silver in testes *1*/*2*/*3* passes into solution with the following concentrations, g/dm^3: 9.18/9.2/7.9. The silver extraction is, %: 99.99/99.99/75. The final solid residue is rhodium concentrate (Table 4), suitable for subsequent reprocessing with production of metallic rhodium.

From the sulfite conditioning solutions obtained, the silver was reduced to metallic state by the addition of caustic soda:

$$2AgCl + Na_2SO_3 + 2NaOH \rightarrow$$
$$\rightarrow 2Ag\downarrow + Na_2SO_4 + 2NaCl + H_2O. \qquad (1)$$

The analysis results of silver residue are summarized in Table 5.

The annealing conditions and rhodium contents in the products of various stages are illustrated in Fig. 8 and Table 6.

The efficiency of rhodium oxidation directly depends on the annealing temperature mode. An increase

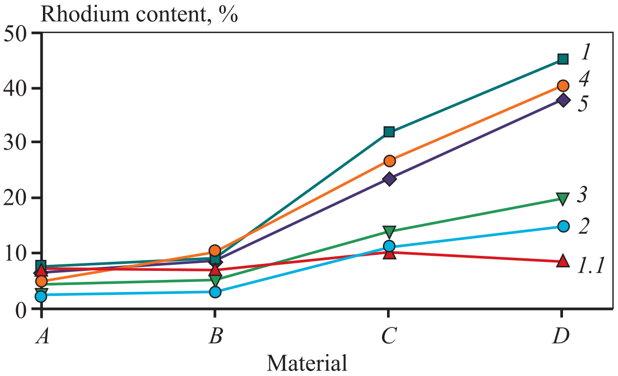

Fig. 8. Rhodium content in GPC reprocessing products annealed under various conditions

Material: ***A*** – initial GPC; ***B*** – GPC after annealing; ***C*** – insoluble residue of GPC leaching; ***D*** – rhodium concentrate
t, °C: ***1.1*** – w/o annealing; ***1*** – 750, OAM; ***2*** – 500, O_2; ***3*** – 620, OAM; ***4*** – 720, O_2; ***5*** – 720, OAM

Рис. 8. Зависимость содержания родия в продуктах переработки ЦПЗ, обожженного при различных условиях

Материал: ***A*** – ЦПЗ исходный; ***B*** – ЦПЗ после обжига; ***C*** – нерастворимый остаток выщелачивания ЦПЗ; ***D*** – концентрат родия
t, °C: ***1.1*** – без обжига; ***1*** – 750, КВС; ***2*** – 500, O_2; ***3*** – 620, КВС; ***4*** – 720, O_2; ***5*** – 720, КВС

Table 6. **Rhodium concentration in initial cementate and products of its reprocessing, %**

Таблица 6. Концентрация родия в исходном цементате и продуктах его переработки, %

Test No.	Annealing conditions		Initial cementate	Cementate after annealing	Residue of AR dissolution*	Rhodium concentrate**
	t, °C	Gas				
1.1	W/o annealing		7.00	7.00	10.29	8.40
1	750	OAM	7.00	9.30	31.95	45.00
2	500	O_2	2.33	2.95	11.00	15.00
3	620	OAM	4.40	5.20	14.00	20.00
4	720	O_2	5.07	10.27	26.83	40.25
5	720	OAM	6.52	8.68	23.72	37.89

[*] Material residue after dissolution in aqua regia.

[**] The obtained rhodium concentrate after performed procedures according to flowchart in Fig. 4.

in the annealing temperature from 500 to 750 °C increases the rhodium content in the concentrate from 15 to 45 %.

Conclusions

The reprocessing flowchart of collective cementate of gold production containing precious metal at AO Uralelektromed was developed and tested. The dependence of the extent of rhodium oxidation on the temperature of preliminary annealing of the cementate was established. Its increase from 500 to 750 °C enhances the content of the targeted metal in the marketable product (concentrate) from 15 to 45 % Rh. The optimum parameters of preliminary oxidating annealing are as follows: 750 °C, 2 hours.

The proposed technological flowchart of GPC reprocessing allows the following individual products to be achieved: silver (Ag ≥ 98 %) and rhodium concentrate (Rh = 15÷45 %) while preserving the quality of gold (Au ≥ 98 %) and PGM concentrate (Pt ≥ 45 %, Pd ≥ 15 %).

In order to further develop this topic, the refinement of rhodium concentrate, adjustment of optimum conditions of its reprocessing and commercial implementation of the technology, could be additionally studied.

References

1. Nagai H., Shibata E., Nakamura T. Development of methods for concentration and dissolution of Rh and Ru from copper slime. *Hydrometallurgy*. 2017;169:282—289. https://doi.org/10.1016/j.hydromet.2017.01.004
2. Crundwell F.K., Moats M.S., Ramachandran V., Robinson T.G., Davenport W.G. Extractive metallurgy of nickel, cobalt and platinum group metals. Chapter 37. Refining of the platinum-group metals. Elsevier Ltd., 2011. P. 489—534. https://doi.org/10.1016/C2009-0-63541-8
3. Nakhjiri A.T., Sanaeepur H., Amooghin A.E., Shirazi M.M.A. Recovery of precious metals from industrial wastewater towards resource recovery and environmental sustainability: A critical review. *Desalination*. 2022;527:115510. https://doi.org/10.1016/j.desal.2021.115510
4. Hayashibe Y. Reference module in chemistry, molecular sciences and chemical engineering. In: *Precious Metals*. Elsevier Ltd., 2005. P. 277—287.
5. Mastyugin S.A., Volkova N.A., Naboichenko S.S., Lastochkina M.A. Sludge of electrolytic refining of copper and nickel. Ekaterinburg: UrFU, 2013. 256 p. (In Russ).
Мастюгин С.А., Волкова Н.А., Набойченко С.С., Ласточкина М.А. Шламы электролитического рафинирования меди и никеля. Екатеринбург: УрФУ, 2013. 256 с.
6. Mulwanda J., Dorfling C. Recovery of dissolved platinum group metals from copper leach solutions by precipitation. *Minerals Engineering*. 2015;80:50—56. https://doi.org/10.1016/j.mineng.2015.07.002
7. Boduen A.Y., Fokina S.B., Polezhaev S.Yu. The hydrometallurgical pretreatment of a refractory gold sulfide concentrate. In: *Innovation-based development of the mineral resources sector: challenges and prospects:* Proceedings of the 11th Russian-German raw materials conference (Potsdam, Germany, 7—8 Nov. 2018). London: CRC Press, 2018. P. 331—340. https://doi.org/10.1201/9780429022388
8. Korolev A.A., Krayukhin S.A., Mastyugin S.A., Gibadullin T.Z., Lebed A.B. A method for obtaining silver and platinum group metals: Pat. 2680552 (RF). 2018. (In Russ.).
Королев А.А., Краюхин С.А., Мастюгин С.А., Гиба-

дуллин Т.З., Лебедь А.Б. Способ получения серебра и металлов платиновой группы: Пат. 2680552 (РФ). 2018.

9. Zotova I.E. , Fokina S.B., Boduen A.Ya., Petrov G.V. Sorption concentration of ruthenium from sulfuric solutions. *Non-Ferrous Metals*. 2019;(1):12—15. https://doi.org/10.17580/nfm.2019.01.02
10. Aghaei E., Alorro R.D., Encila A.N., Yoo K. Magnetic adsorbents for the recovery of precious metals from leach solutions and wastewater. *Metals*. 2017;7(12):529. https://doi.org/10.3390/met7120529
11. Aleksandrova T.N., O'Connor C. Processing of platinum group metal ores in Russia and South Africa: current state and prospects. *Journal of Mining Institute*. 2020;244:462—473. (In Russ.). https://doi.org/10.31897/PMI.2020.4.9
    Александрова Т.Н., О'Коннор С. Переработка платинометалльных руд в России и Южной Африке: состояние и перспективы. *Записки Горного института*. 2020;244:462—473. https://doi.org/10.31897/PMI.2020.4.9
12. Jacek Sitko. Analysis of selected technologies of precious metal recovery processes. *Multidisciplinary Aspects of Production Engineering* 2019;2(1):72—80. https://doi.org/10.2478/mape-2019-0007
13. Kobylyanski A., Zhukova V., Petrov G., Boduen A. Challenges in processing copper ores containing sulfosalts. In: *Scientific and practical studies of raw material issues:* Proceedings of the Russian-German raw materials dialogue: A collection of young scientists papers and discussion (19 Nov. 2019). London: CRC Press, 2020. P. 120—126. https://doi.org/10.1201/9781003017226-18
14. Lebed A.B., Maltsev G.I., Mamyachenkov S.V. Refining of gold of silver alloys at JSC Uralelectromed. Ekaterinburg: UrFU, 2015. 159 p. (In Russ.).
    Лебедь А.Б., Мальцев Г.И., Мамяченков С.В. Аффинаж золотосеребряных сплавов на ОАО «Уралэлектромедь». Екатеринбург: УрФУ, 2015. 159 с.
15. Lebed A.B., Skorokhodov V.I., Kremko E.G., Volkova N.A., Mastyugin S.A., Goryaeva O.Yu., Rychkov D.M. Method of isolation of platinum metals: Pat. 2111272 (RF). 1998. (In Russ.).
    Лебедь А.Б., Скороходов В.И., Кремко Е.Г., Волкова Н.А., Мастюгин С.А., Горяева О.Ю., Рычков Д.М. Способ выделения платиновых металлов: Пат 2111272 (РФ). 1998.
16. Polvanov S., Ergashev N., Khodzhiev M., Tashmuratov A. Study of obtaining accompanying elements in the processing of gold-bearing ores of the muruntau deposit. *Universum: Engineering Sciences*. 2022;7(100):20—24. https://doi.org/10.32743/UniTech.2022.100.7.14079
17. Kononova O.N., Melnikov A.M., Borisova T.V. Method of separation of platinum (II, IV), rhodium (III) and nickel (II) in chloride solutions: Pat. 2527830 (RF). 2010. (In Russ.).
    Кононова О.Н., Мельников А.М., Борисова Т.В. Способ разделения платины (II, IV), родия (III) и никеля (II) в хлоридных растворах: Пат. 2527830 (РФ). 2010.
18. Ginzburg S.I., Ezerskaya N.A., Prokofieva I.V. Fedorenko N.V., Shlenskaya V.I., Belskii N.K. Analytical chemistry of platinum metals. Moscow: Nauka, 1972. 616 p. (In Russ.).
    Гинзбург С.И., Езерская Н.А., Прокофьева И.В., Федоренко Н.В., Шленская В.И., Бельский Н.К. Аналитическая химия платиновых металлов. М.: Наука, 1972. 616 с.
19. Plekhanov K.A., Ashikhin V.V., Sheveleva L.D., Lebed A.B., Krayukhin S.A., Skopin D.Yu. The method of isolation of platinum metals: Pat. 2238244 (RF). 2002. (In Russ.).
    Плеханов К.А., Ашихин В.В., Шевелева Л.Д., Лебедь А.Б., Краюхин С.А., Скопин Д.Ю. Способ выделения платиновых металлов: Пат. 2238244 (РФ). 2002.
20. Huang Z.S., Yang T.Z. Comparative study on refractory gold concentrate kinetics and mechanisms by pilot scale batch and continuous bio-oxidation. *Minerals*. 2021;11(12):1343. https://doi.org/10.3390/min11121343
21. Rinne M., Elomaa H., Seisko S., Lundstrom M. Direct cupric chloride leaching of gold from refractory sulfide ore: process simulation and life cycle assessment. *Mineral Processing and Extractive Metallurgy Review*. 2021;43(5):598—609. https://doi.org/10.1080/08827508.2021.1910510
22. Maslenitsky I.N., Chugaev L.V. Metallurgy of precious metals. Moscow: Metallurgiya, 1987. 432 p. (In Russ.).
    Масленицкий И.Н., Чугаев Л.В. Металлургия благородных металлов. М.: Металлургия, 1987. 432 с.
23. Meretukov M.A., Orlov A.M. Metallurgy of precious metals. Foreign experience. Moscow: Metallurgiya, 1991. 416 p. (In Russ.).
    Меретуков М.А., Орлов А.М. Металлургия благородных металлов. Зарубежный опыт. М.: Металлургия, 1991. 416 с.
24. Kepp K.P. Chemical causes of metal nobleness. *ChemPhysChem*. 2020;21(5):360—369. https://doi.org/10.1002/cphc.202000013
25. Fedorov I.A. Rhodium. Moscow: Nauka, 1966. 276 p. (In Russ.).
    Федоров И.А. Родий. М.: Наука, 1966. 276 с.
26. Beamish F. Analytical chemistry of precious metals. Ed. S.I. Ginzburg. Moscow: Mir, 1969. 592 p. (In Russ.).
    Бимиш Ф. Аналитическая химия благородных ме-

таллов. Пер. с англ. под ред. С.И. Гинзбург. М.: Мир, 1969. 592 с.

27. Kunimori K., Oyanagi H., Shindo H., Ishigaki T., Uchijima T. Structural transformation and catalytic behaviors of rhodium ternary oxides during calcination and reduction treatments. *Studies in Surface Science and Catalysis*. 1993;75:2039—2042. https://doi.org/10.1016/S0167-2991(08)64220-2
28. Šarić A., Popović S., Trojko R., Music S. The thermal behavior of amorphous rhodium hydrous oxide. *Journal of Alloys and Compounds*. 2001;320(1):140—148. https://doi.org/10.1016/S0925-8388(01)00938-0
29. Barclay G.A., Broadbent R.F., Kingston J.V., Scollary G.R. The thermal behaviour of some rhodium complexes. *Thermochimica Acta*. 1974;10(1):73—83. https://doi.org/10.1016/0040-6031(74)85025-2
30. Nitsenko A.V., Volodin V.N., Linnik X.A., Tuleutay F.K., Burabaeva N.M. Distillation recovery of tellurium from copper telluride in oxide forms. *Izvestiya. Non-Ferrous Metallurgy*. 2022;28(4):45—54. (In Russ.). https://doi.org/10.17073/0021-3438-2022-4-45-54
Ниценко А.В., Володин В.Н., Линник К.А., Тулеутай Ф.Х., Бурабаева Н.М. Дистилляционное извлечение теллура из теллурида меди в оксидных формах. *Известия вузов. Цветная металлургия*. 2022;28(4): 45—54. https://doi.org/10.17073/0021-3438-2022-4-45-54

Information about the authors

Yakov D. Zelyakh – Leading Process Engineer of the Research Center of JSC «Uralelectromed».
https://orcid.org/0000-0003-0486-9363
E-mail: zyad@elem.ru

Roman S. Voinkov – Cand. Sci. (Eng.), Head of the Research Center of JSC «Uralelectromed»; Associate Professor of the Department of Metallurgy of the Technical University of the Ural Mining and Metallurgical Company (UMMC).
https://orcid.org/0000-0001-6697-1596
E-mail: r.voinkov@elem.ru

Konstantin L. Timofeev – Dr. Sci. (Eng.), Head of the Technical Department of JSC «Uralelectromed»; Associate Professor of the Department of Metallurgy of the Technical University of the UMMC.
https://orcid.org/0000-0002-9525-6476
E-mail: K.Timofeev@elem.ru

Gennady I. Maltsev – Dr. Sci. (Eng.), Senior Scientific Officer, Chief Specialist of the Research Center of JSC «Uralelectromed».
https://orcid.org/0000-0002-0750-0070
E-mail: mgi@elem.ru

Информация об авторах

Яков Дмитриевич Зелях – вед. инженер-технолог Исследовательского центра АО «Уралэлектромедь».
https://orcid.org/0000-0003-0486-9363
E-mail: zyad@elem.ru

Роман Сергеевич Воинков – к.т.н., начальник Исследовательского центра АО «Уралэлектромедь»; доцент кафедры металлургии Технического университета Уральской горно-металлургической компании (УГМК).
https://orcid.org/0000-0001-6697-1596
E-mail: r.voinkov@elem.ru

Константин Леонидович Тимофеев – д.т.н., начальник технического отдела АО «Уралэлектромедь»; доцент кафедры металлургии Технического университета УГМК.
https://orcid.org/0000-0002-9525-6476
E-mail: K.Timofeev@elem.ru

Геннадий Иванович Мальцев – д.т.н., ст. науч. сотрудник, гл. специалист Исследовательского центра АО «Уралэлектромедь».
https://orcid.org/0000-0002-0750-0070
E-mail: mgi@elem.ru

Contribution of the authors

Ya.D. Zelyakh – formulated the main concept, prepared the experiments, calculations, analysis of research results, wrote the manuscript, formulated conclusions.

R.S. Voinkov – provided resources, formulated the main concept, formulated the target and objective of the study, wrote the manuscript, formulated conclusions.

K.L. Timofeev – scientific advising, revised the manuscript, revised the conclusions.

G.I. Mal'tsev – scientific advising, calculations, wrote the manuscript.

Вклад авторов

Я.Д. Зелях – формирование основной концепции, подготовка экспериментов, проведение экспериментов, проведение расчетов, анализ результатов исследований, подготовка текста статьи, формулировка выводов.

Р.С. Воинков – обеспечение ресурсами, формирование основной концепции, постановка цели и задачи исследования, подготовка текста, формулировка выводов.

К.Л. Тимофеев – научное руководство, корректировка текста, корректировка выводов.

Г.И. Мальцев – научное руководство, проведение расчетов, подготовка текста статьи.

The article was submitted 27.12.2022, revised 05.04.2023, accepted for publication 10.04.2023

Статья поступила в редакцию 27.12.2022, доработана 05.04.2023, подписана в печать 10.04.2023

UDC 621.74
https://doi.org/10.17073/0021-3438-2023-3-38-53

Research article
Научная статья

The efficiency of multithreaded computing in casting simulation software

V.E. Bazhenov[1], **A.V. Koltygin**[1], **A.A. Nikitina**[1], **V.D. Belov**[1], **E.A. Lazarev**[2]

[1] **National University of Science and Technology «MISIS»**
4 Leninskiy Prosp., Moscow, 119049, Russia

[2] **PJSC "UEC-Kuznetsov"**
29 Zavodskoe Shosse, Samara, 443009, Russia

✉ Viacheslav E. Bazhenov (V.E.Bagenov@gmail.com)

Abstract: The utilization of computer simulation software for casting process simulation is becoming essential in the advancement of casting technology in aviation and other high-tech engineering fields. With the increase in the number of computational cores in modern CPUs, the use of multi-threaded computations is becoming increasingly relevant. In this study, the efficiency of multi-threaded computations in modeling casting processes was evaluated using finite element method casting simulation software ProCast and PoligonSoft, which utilize parallel computing architectures with distributed (DMP) and shared (SMP) memory, respectively. Computations were performed on Intel and AMD-based computers, varying the number of computational threads from 4 to 32. The calculation efficiency was evaluated by measuring the calculation speed increase in the filling and solidification of GP25 castings made of ML10 alloy, as well as the complex task of filling and solidification modeling nickel superalloy casing castings with radiation heat transfer simulation. The results indicate that the minimum computation time in ProCast software is observed when using 16 computational threads. This pattern holds true for both computing systems (Intel and AMD processors), and increasing the number of threads beyond this point does not make a practical difference. The performance decrease in this scenario can be attributed to the low-performance energy-efficient cores in systems based on Intel processors or the decrease in core frequency and full loading of physical cores in systems based on AMD processors. Multi-threading the modeling task in PoligonSoft software is less efficient than in ProCast, which is a result of the shared-memory architecture used in PoligonSoft. Despite the significant difference in parallel efficiency, the task of GP25 casting solidification in both PoligonSoft and ProCast is solved in a time close enough to be considered sufficient.

Keywords: casting simulation, multithreaded computing, ProCast, PoligonSoft, SMP, DMP.

Acknowledgments: This research received financial support from the Ministry of Science and Higher Education in the Russian Federation (Agreement No. 075-11-2022-023 from 06 April 2022) under the program ''Scientific and technological development of the Russian Federation'' according to governmental decree No. 218 dated 9 April 2010.

For citation: Bazhenov V.E., Koltygin A.V., Nikitina A.A., Belov V.D., Lazarev E.A. The efficiency of multithreaded computing in casting simulation software. *Izvestiya. Non-Ferrous Metallurgy.* 2023;29(3):38–53. https://doi.org/10.17073/0021-3438-2023-3-38-53

Эффективность многопоточных вычислений в системах компьютерного моделирования литейных процессов

В.Е. Баженов[1], **А.В. Колтыгин**[1], **А.А. Никитина**[1], **В.Д. Белов**[1], **Е.А. Лазарев**[2]

[1] **Национальный исследовательский технологический университет «МИСИС»**
119049, Россия, г. Москва, Ленинский пр-т, 4, стр. 1

[2] **ПАО «ОДК-Кузнецов»**
443009, Россия, г. Самара, ул. Заводское шоссе, 29

✉ Вячеслав Евгеньевич Баженов (V.E.Bagenov@gmail.com)

Аннотация: Применение систем компьютерного моделирования литейных процессов (СКМ ЛП) становится обязательным при разработке литейной технологии в авиации и других наукоемких областях техники. В связи с увеличением числа расчетных ядер в современных процессорах актуальным становится осуществление многопоточных вычислений. В работе оценивалась эффективность многопоточных вычислений при моделировании литейных процессов с помощью конечно-элементных СКМ ЛП «ProCast» и «ПолигонСофт», использующих архитектуры параллельных расчетов с распределенной (DMP) и общей (SMP) памятью соответственно. Для вычислений применяли компьютеры на базе платформ от компаний «Intel» и «AMD». Число расчетных потоков варьировали от 4 до 32. Эффективность оценивали по приросту скорости расчета заполнения и затвердевания отливки «ГП25» из сплава МЛ10, а также решения сложной задачи моделирования заполнения и затвердевания корпусных отливок из никелевого жаропрочного сплава с учетом радиационного теплообмена. Показано, что минимальное время расчета в СКМ ЛП «ProCast» наблюдается при использовании 16 вычислительных потоков. Причем это характерно для обеих вычислительных систем (на процессорах «Intel» и «AMD»), и увеличение числа потоков выше этого предела не имеет практического смысла. Снижение производительности в данном случае может быть связано с наличием малопроизводительных энергоэффективных ядер в случае применения системы на процессоре «Intel», а также полной загрузки физических ядер и уменьшением частоты ядер для системы на процессоре от «AMD». Распараллеливание задачи моделирования в СКМ ЛП «ПолигонСофт» менее эффективно, чем в СКМ ЛП «ProCast», вследствие реализации архитектуры с общей памятью. В то же время, несмотря на значительную разницу в эффективности распараллеливания, задача затвердевания отливки «ГП25» в СКМ ЛП «ПолигонСофт» и «ProCast» решается за достаточно близкое время.

Ключевые слова: компьютерное моделирование литейных процессов, многопоточные вычисления, ProCast, ПолигонСофт, SMP, DMP.

Благодарности: Работа выполнена при финансовой поддержке Министерства науки и высшего образования Российской Федерации в рамках постановления Правительства № 218 по соглашению о предоставлении субсидии № 075-11-2022-023 от 06.04.2022 г. «Создание технологии изготовления уникальных крупногабаритных отливок из жаропрочных сплавов для газотурбинных двигателей, ориентированной на использование отечественного оборудования и организацию современного ресурсоэффективного, компьютероориентированного литейного производства».

Для цитирования: Баженов В.Е., Колтыгин А.В., Никитина А.А., Белов В.Д., Лазарев Е.А. Эффективность многопоточных вычислений в системах компьютерного моделирования литейных процессов. *Известия вузов. Цветная металлургия*. 2023;29(3):38–53.
https://doi.org/10.17073/0021-3438-2023-3-38-53

Introduction

With the advancements in computer technology, simulation has become extensively utilized in various manufacturing fields, including casting. Casting engineers routinely employ numerous casting simulation software (CSS) for this purpose. Nowadays, simulation has become an obligatory step in the process of gating system development, particularly in industries like aerospace and other advanced sectors. The implementation of simulation helps in reducing production engineering costs.

In order to enhance performance, advanced computer-aided engineering (CAE) tools and CSS support multithreaded computations. The initial concept of parallel computing originated from grid computing, which involves a network of interconnected computers forming a “virtual supercomputer”. Presently, cloud computing employing remote supercomputers has become the dominant approach, although multi-core personal computers (PCs) are also widely used [1]. These developments are based on the progress in computer science, particularly the increasing computational speed of multicore processors [2]. Furthermore, GPU computing has emerged as an intriguing advancement, although its current usage in casting simulation is limited [3—5].

Parallel computing is typically categorized into two types: distributed memory processing (DMP) and shared memory processing (SMP). In DMP, each CPU core is allocated a specific memory, whereas in SMP, all cores access the same shared memory (see Fig. 1) [4; 6]. The message passing interface (MPI) is responsible for managing message exchange between multiple cores [7].

The DMP architecture has been proven to be more efficient. For example, Pannala S. et al. [8] conducted an assessment of parallel computations for fluidized bed simulation. They found that the SMP architecture with 32 threads resulted in a 14-fold improvement in performance, whereas the DMP architecture achieved a remarkable 27-fold acceleration under the same conditions, which is close to the theoretical maximum limit of 32.

However, it should be noted that the total increase in computing performance is often is less than the sum of the performance of individual cores [9]. The SYSWeld (ESI Group) welding and heat treatment simulation software utilizes the DMP architecture, which yields a 5-fold performance improvement with 8 threads [10]. As the number of threads is further increased, the efficiency of computation parallelization diminishes. For 32 threads, the performance gain was only 9-fold, representing a mere quarter of the theoretically possible limit. In the work by Yang W.-H. et al. [11], ANSYS (ANSYS, Inc.) was employed to simulate plastic injection molding with 1 to 4 threads. The performance improvement ranged from 1.5 to 2.1 times for two threads, and 3.1 to 3.4 times for four threads. Corke G. [12] tackled various simulation problems in ANSYS 17 with different thread numbers (up to 28), revealing that the performance gain occurred up to 16 threads. Beyond that point, increasing the number of threads had little to no effect on performance, and in some cases, it even decreased. On average, the performance gain remained below 7-fold for 28 threads. Posey S. et al. [5] reported a 6-fold performance improvement when solving deformable body, CFD, and heat transfer problems with LS-DYNA (ANSYS, Inc.) using 6 threads. The computational performance is not solely determined by CPU speed and the number of threads. Corke G. [12] demonstrated that replacing the hard disk drive (HDD) with a Serial Advanced Technology Attachment (SATA) Solid-state drive (SSD) resulted in a 4-fold performance increase, while a faster NVME (Non-Volatile Memory Host Controller Interface Specification) SSD led to a 7-fold improvement. Expanding the RAM also contributes to the performance gain, although to a lesser extent. Yang W.-H. et al. [11] reported conflicting relationships between the number of computational mesh nodes and computational performance [11].

Parallel computations have also been applied to casting simulation. For example, Trębacz L. et al. [13] conducted simulations of continuous steel casting using a distributed solver and the ProCast CSS (ESI Group). Their findings indicated that the size of the FEM mesh has little impact on the efficiency of parallel computing. The study also revealed that the ProCast solver exhibits low computing costs for thread synchronization. The efficiency of the solver with 8 threads reached only 70 % of the theoretically possible limit compared to single-thread computation. Konopka K. et al. [2] simulated continuous casting using ProCast and employed both distributed computing and a cloud computing platform. Their results demonstrated that 2, 4, and 8 threads reduced the calculation time by 71, 219, and 421 %, respectively, compared to a single thread. This indicates that the performance gain diminishes as the number of threads increases, likely due to increasing costs associated with message exchanges between solver threads.

In summary, parallelism in casting simulation can significantly enhance performance. However, it is important to note that the papers [2] and [13] were published in 2014—2015. Since then, parallel computing has advanced significantly with the emergence of

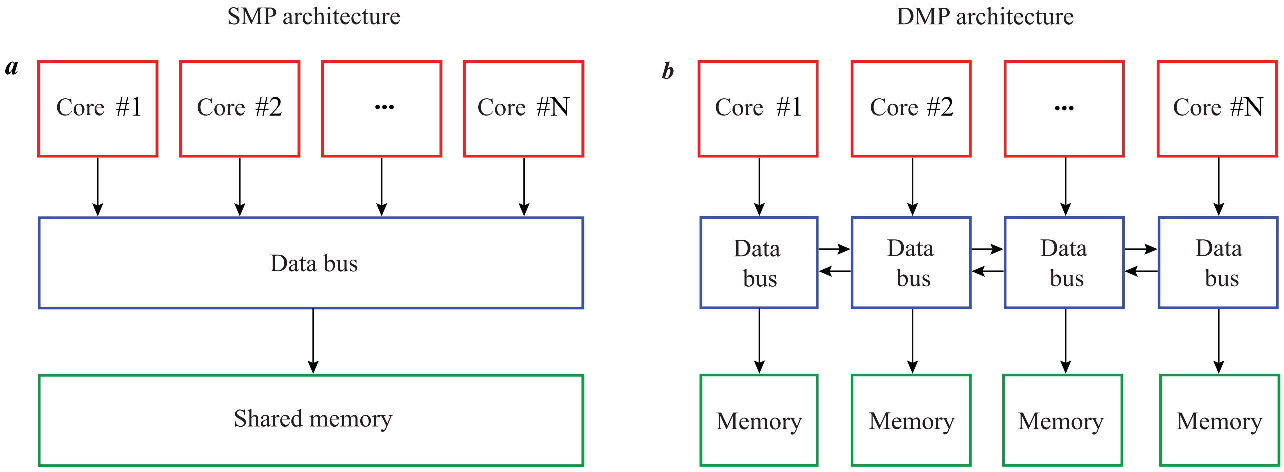

Рис. 1. Архитектуры параллельных вычислений по принципу SMP (***a***) и DMP (***b***)

Fig. 1. Schemes of parallel computing based on the SMP (***a***) and DMP (***b***) architectures

multicore processors capable of running 32 or more threads.

Casting processes are primarily simulated using the finite element method (FEM), finite difference method (FDM), and finite volume method (FVM). FDM (and FVM) solutions are considerably inferior to FEM in terms of accuracy, reliability, computational resource requirements, performance, and postprocessing options [14]. Hence, for casting simulation in this study, we employed FEM.

The objective of this study is to compare the performance of multithreaded casting simulations using ProCast [15; 16] and PoligonSoft [17—19] CSS, which utilize FEM and have DMP and SMP architectures, respectively [13].

Materials and methods

In our study, we conducted simulations of mold filling and solidification using ProCast 2022 (ESI Group, France) and PoligonSoft 2022 (CSoft, Russia). The simulation times were measured for different numbers of threads. ProCast employs FEM to simulate filling and solidification. For solidification analysis, the Fourier heat conduction equation is utilized, taking into account the additional latent heat release. Mold filling is simulated using the Navier-Stokes equation. The filling simulation uses the Newtonian viscosity model and a momentum-driven free surface movement model that considers mass conservation [20]. For further details and equations, please refer to [21—23]. On the other hand, PoligonSoft analyzes solidification using FEM and the Fourier equation [24].

We executed the simulations on two computers equipped with Intel (USA) and AMD (USA) CPUs. The specifications of the computers are provided in Table 1. The Intel system utilized 4, 8, 12, 16, 20, and 24 threads, while the AMD system employed 4, 8, 12, 16, 20, 24, 28, and 32 threads. Throughout the simulations, we monitored the CPU temperature, which remained below the CPU temperature limit, and no throttling (reduction in CPU frequency due to overheating) was necessary. The operating system (OS) and programs running in the background take up some of the computing resources. It is worth noting that the OS and background programs utilize some computing resources. However, in the case of the computers we used, the impact of the OS is assumed to be negligible due to the large number of cores in the processors, excessive RAM allocation for the OS, and, most importantly, the presence of fast SSD M.2 NVME SSDs. To minimize any performance impact, no other applications were running on the computers during the simulations.

In our analysis, we primarily focused on the GP25 cast part, which is manufactured using the ML10 magnesium alloy and cast in resin bonded sand mold with cast iron chill inserts. The GP25 part is a thin-walled, case-shaped part, and its configuration is presented in [25]. To estimate the thermophysical properties of the ML10 alloy, we utilized ProCast thermodynamic properties database for non-equilibrium solidification, employing the Scheil-Gulliver model. Similarly, the properties of the cast iron chill inserts were obtained from the ProCast materials database. The thermophysical properties of the resin bonded sand mold were referenced from Palumbo G. et al. [26], while the casting-mold and casting-chill insert interfacial heat transfer coefficients were obtained from Bazhenov V. et al. [27; 28]. The mold filling time was 40 s., with a melt pouring temperature of 720 °C, and a mold temperature of 20 °C. The mold filling and solidification simulation time were measured separately since the number of FEM mesh nodes varies during filling but remains constant during solidification. This variation may potentially impact the runtime with different thread configurations.

Furthermore, we conducted simulations of filling and solidification for three large-size casing parts (ranging from 705 to 1136 mm in diameter) made of the VZHL14H-VI nickel superalloy, using an investment casting process with ceramic mold. The simulation encompassed various stages, including mold cooling in the furnace before filling, melt filling into the mold, and subsequent cooling. The simulation also accounted for radiation heat transfer. The aim was to assess the efficiency of parallelism in addressing complex, multistage simulation problems. The thermophysical properties of the VZHL14H-VI alloy were calculated using the thermodynamic database of ProCast CSS, while the Scheil-Gulliver model was employed to estimate properties for non-equilibrium solidification. The thermophysical properties of the mold ceramics, steel furnace components, heat insulation, and backing material were derived from the ProCast materials database. The boundary conditions were also retrieved from the database using the investment casting simulation workflow. The initial melt temperature was set at 1450 °C, and the initial mold temperature was 950 °C.

Table 1. **Hardware of computers used for simulation**

Таблица 1. Комплектующие, используемые при сборке компьютеров для моделирования

Name	Intel system	AMD system
Processor	Intel Core I9 12900KF (16 cores, 24 threads)	AMD Ryzen 9 5950X (16 cores, 32 threads)
Motherboard	Gygabyte Gaming X (LGA1700, Z690)	MSI MAG Torpedo (AM4, X570)
RAM	Kingston DIMM DDR5, 5200 MHz, CL40, 64 GB (2 modules)	Kingston DIMM DDR4, 3600 MHz, CL18, 64 GB (2 modules)
Cooling system	NZXT Kraken X73 liquid cooler	ID-Cooling SE-207 XT air cooler
SSD	Samsung 980 Pro, M.2 NVME, 1000 GB	Samsung 970 EVO, M.2 NVME, 500 GB

For mesh generation, the Visual Mesh mesher, a module of ProCast, was employed. The same mesh was used for the PoligonSoft simulations. The GP25 part employed an adaptive mesh with variable element sizes (node-to-node distances), ranging from 3, 4, 5, 6, 8, to 10 mm. These meshes are denoted as L3, L4, L5, L6, L8, and L10, respectively. The finite elements representing the riser and mold were 2 times and 5 times larger, respectively (as indicated in Table 2). The number of tetrahedral finite elements for meshes L3 to L10 ranged from 7.37 to 0.73 mln.

Regarding the FEM meshes representing the casting of large parts made of the VZHL14H-VI nickel superalloy, the element sizes ranged from 3 mm for the part itself to 70 mm for the furnace chamber.

Results and discussion

Figure 2 illutstrates the simulation times for GP25 mold filling using ProCast on Intel and AMD PCs, as well as the corresponding performance gain (expressed as percentage) with respect to the number of threads. These results pertained to finite elements L3—L10 size.

For the Intel PC (Fig. 2, *a*), the simulation time curve exhibits a minimum value across all the meshes, irrespective of the number of elements. The minimum simulation time was achieved when employing 16 threads. However, increasing the thread count to 20 and 24 not only fails to decrease the simulation time but actually leads to an increase. Additionally, the simulation time increases as the number of mesh elements grows.

Figure 2, *b* demonstrates that the performance gain for 8 threads compared to 4 threads ranges from 66 to 77 %, while for 16 threads, it falls between 144 and 172 %. In most cases, meshes with a larger number of smaller elements yield a higher performance gain. The dashed curve represents the maximum theoretical performance gain, assuming that the gain for *N* threads is equal to the performance of a single thread multiplied by *N*. Accordingly, the maximum theoretical performance gain for 8 and 16 threads over 4 threads should be 100 and 300 % respectively. However, it is evident that as the threads count increases, the deviation from the maximum possible performance gain becomes more pronounced. Notably, when the number of threads exceeds 16 (20 and 24), a decrease in performance is observed.

While a decrease in performance with increasing thread count has been observed by other researchers studying different simulation software [2; 5; 8; 10—13], the decline seen when the number of threads surpasses 16 appears somewhat peculiar. To shed light on potential causes for this performance degradation, a closer examination of the Intel I9 12900KF processor is warranted. This processor comprises 8 performance cores (designated as “P” for “performance”) and 8 energy-efficient cores (denoted as “E”). The P cores can further divide calculations into 2 threads,

Table 2. **The mesh parameters used for simulation**

Таблица 2. Характеристики сеточных моделей, использованных для моделирования

Part	Initial mesh element size, mm			Number of 3D elements, mln.
	Part	Riser	Mold	
GP25 (L10)	10	20	50	0.73
GP25 (L8)	8	16	40	0.98
GP25 (L6)	6	12	30	1.62
GP25 (L5)	5	10	25	2.35
GP25 (L4)	4	8	20	3.82
GP25 (L3)	3	6	15	7.37
Casing part 1	3–70	3–70	3–70	7.32
Casing part 2	3–70	3–70	3–70	3.52
Casing part 3	3–70	3–70	3–70	4.94

resulting in a total of 16 P and 8 E logical cores. The performance of the P cores significantly surpasses that of the E cores.

Table 3 presents the number of logical cores versus the number of threads, as well as the core clock frequency measured after 5 minutes of the simulation start. For 4 threads, both the performance P cores and energy-efficient cores are utilized. It should be noted that 12 performance logical cores and 7 energy-efficient cores are employed when utilizing 4 threads, which accounts for the majority of available cores. Consequently, the application is distributed among the logical cores, as each physical P core encompasses two logical cores. Only when 4 threads are employed the clock frequencies of individual physical cores increase to 5 GHz and 3.9 GHz for P and E cores, respectively. This factor may account for the high performance gain observed (which is quite close to the theoretically maximum achievable gain) with a small number of threads. However, employing energy-efficient cores proves impractical given their lower performance. After distributing the mesh nodes across the cores, each simulation step is completed more swiftly by the high-performance cores, leading to the performance cores waiting for the energy-efficient cores to finish their part of the calculation.

For 8 or more threads, the clock frequencies of P and E cores are 4.9 GHz and 3.7 GHz, respectively. The utilization of cores varies randomly, but their overall load increases. The case of 16 threads is particularly interesting as only the performance P cores are engaged, representing the maximum performance mode (as shown in Fig. 2, *a* and *b*). Further increasing the thread count results in a slowdown of the simulation due to the simultaneous utilization of energy-efficient E cores and the absence of load sharing among logical cores. For instance, with 20 threads, the E cores bear a 50 % load, with only 4 out of 8 E cores being operational. The remaining E cores remain idle, with a load of 0 %.

In the case of the AMD system (refer to Fig. 2, *c*), a similar trend is observed with the simulation time curve reaching its minimum when the number of threads is 16, mirroring the behavior of the Intel system. Despite the architectural differences between the processors, the optimal performance is achieved when utilizing 16 threads for both systems. However, increasing the number of threads beyond 20 results in a significant increase in simulation time, with the simulation time for 8 threads being shorter than for 20 threads.

Figure 2, *d* illustrates the performance gain for the AMD system. The gain is lower compared to the Intel system, with 44 % to 62 % for 8 threads and 97 % to 116 % for 16 threads. As the number of threads increases, the performance gain deviates further from the dashed

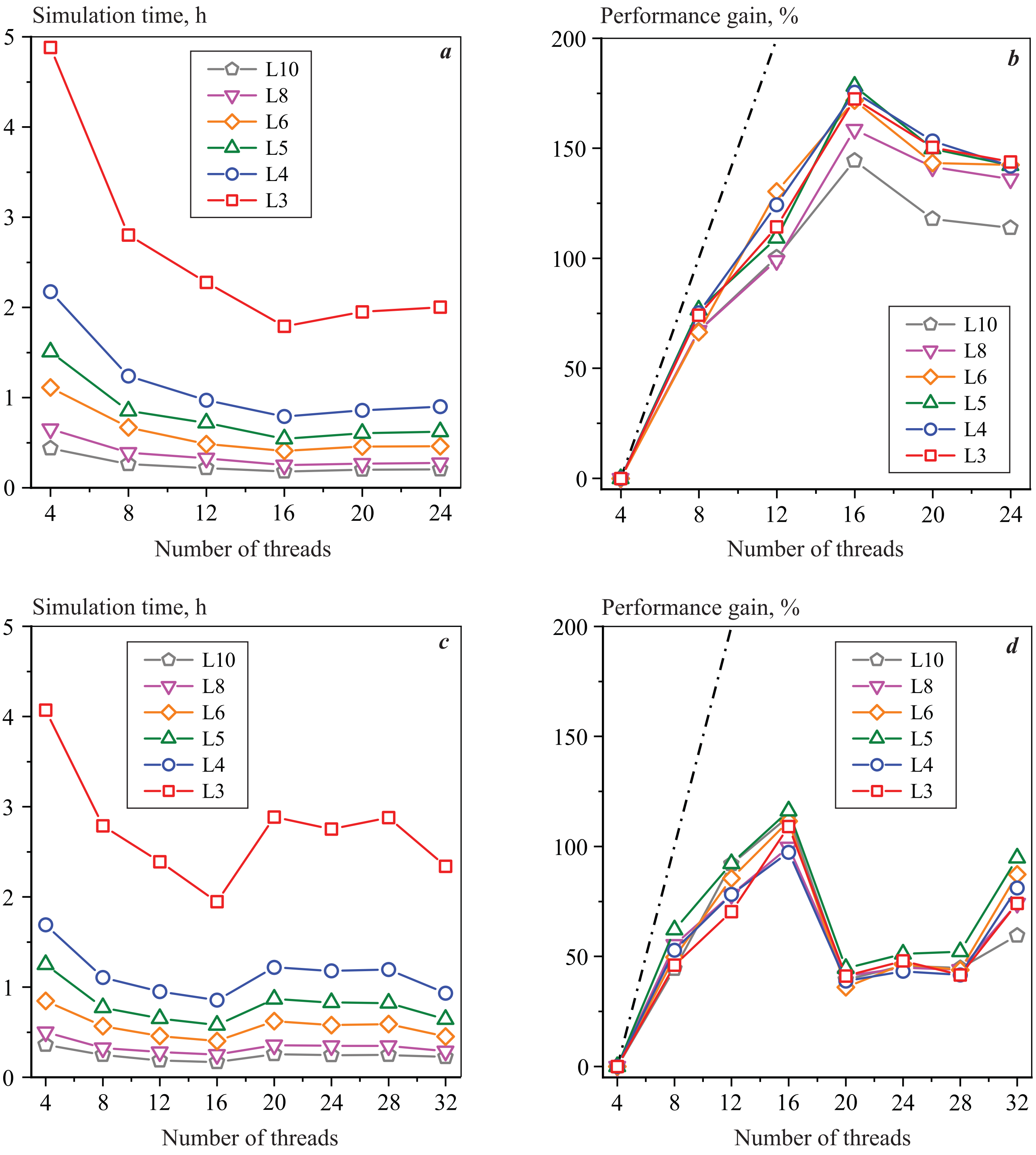

Fig. 2. The calculation time of GP25 casting filling in ProCast (***a***, ***c***) and the calculation speed growth (***b***, ***d***) depending on the number of threads involved in the calculation, when using computers based on the platforms from Intel (***a***, ***b***) and AMD (***c***, ***d***) and L3–L10 simulation meshes (see Table 2)

Рис. 2. Длительность расчета заливки отливки «ГП25» в программе «ProCast» (***a***, ***c***) и прирост скорости расчета (***b***, ***d***) в зависимости от количества потоков, задействованных в расчете при использовании компьютеров на базе платформ «Intel» (***a***, ***b***) и «AMD» (***c***, ***d***) и расчетных сеток L3–L10 (см. табл. 2)

Table 3. **The number of threads involved in the calculation, cores load and frequency**

Таблица 3. Задействованное в расчете количество потоков, загрузка ядер и частота

Number of threads	Intel					AMD				
	P cores		E cores		P/E core clock frequency, GHz	CCX #0		CCX #1		Core clock frequency, GHz
	Number (16 max.)	Load, %	Number (8 max.)	Load, %		Number (16 max.)	Load, %	Number (16 max.)	Load, %	
4	12	13	7	25	4.9–5.0 / 3.7–3.9	16	13	11	13	4.63
8	9	36	5	23	4.9 / 3.7	16	26	14	25	4.58
12	11	49	8	46	4.9 / 3.7	16	51	8	25	4.41
16	16	100	0	0	4.9 / 3.7–3.9	16	53	16	51	4.30
20	16	100	4	50	4.9 / 3.7	16	100	4	26	4.42
24	16	100	8	100	4.9 / 3.7	16	100	8	52	4.31
28	–	–	–	–	–	16	100	12	76	4.19
32	–	–	–	–	–	16	100	16	100	4.08

line representing the maximum theoretical performance gain. Notably, a substantial performance drop occurs when the number of threads exceeds 20, without any apparent correlation between the performance gain and mesh size.

The AMD 5950X processor architecture consists of two CCX (core complex) clusters, each containing 16 logical cores (they are specified as CCX #0 and CCX #1 in Table 3). While sharing some similarities with the Intel processor discussed earlier, the AMD complex cores are identical and lack differentiation between high-performance and energy-efficient cores.

Table 3 provides the number of logical cores and threads for the AMD processor. When using 4 threads, both CCXs clusters are utilized, similar to the Intel processor, with most logical cores being actively engaged in load distribution. Consequently, the physical cores can operate at a relatively high clock frequency of 4.63 GHz. However, as the number of threads increases to 8 and 12, the clock frequency is reduced to 4.58 GHz and 4.41 GHz, respectively, impacting the overall efficiency of parallel computation. The distribution of load between the CCXs becomes uneven for 12 threads, potentially leading to a slowdown in the simulation. At the maximum performance mode of 16 threads, the CCX load is evenly distributed at 50 %, utilizing all available logical cores. In this case, the average clock frequency decreases to 4.3 GHz. When the number of threads reaches 20, an asymmetry in the CCX clusters loads becomes apparent. The first CCX #0 is fully loaded at 100 %, making it impossible to distribute the load across its logical cores, while the second CCX #1 is only 25 % loaded. It is important to note that despite the incomplete loading of CCX #1, there is no load distribution among its logical cores. The average clock frequency even experiences a slight increase compared to the 16 threads simulation.

Further increasing the number of threads results in a decrease in the average CPU clock frequency, reaching 4.08 GHz when utilizing all available threads. Hence, the performance degradation observed with 20 or more threads can be attributed to the uneven load distribution between CCXs and the decreasing of CPU core clock frequency. This leads to a decrease in the efficiency of load distribution among the logical cores as the system approaches the limit of physical cores (which is 16 cores in the CPU). Another possible contributing factor could be the cache memory. When one physical core handles two threads, the cache is shared. With a large number of commands and data, they may not fit into the cache memory, resulting in an increased number of RAM accesses operations.

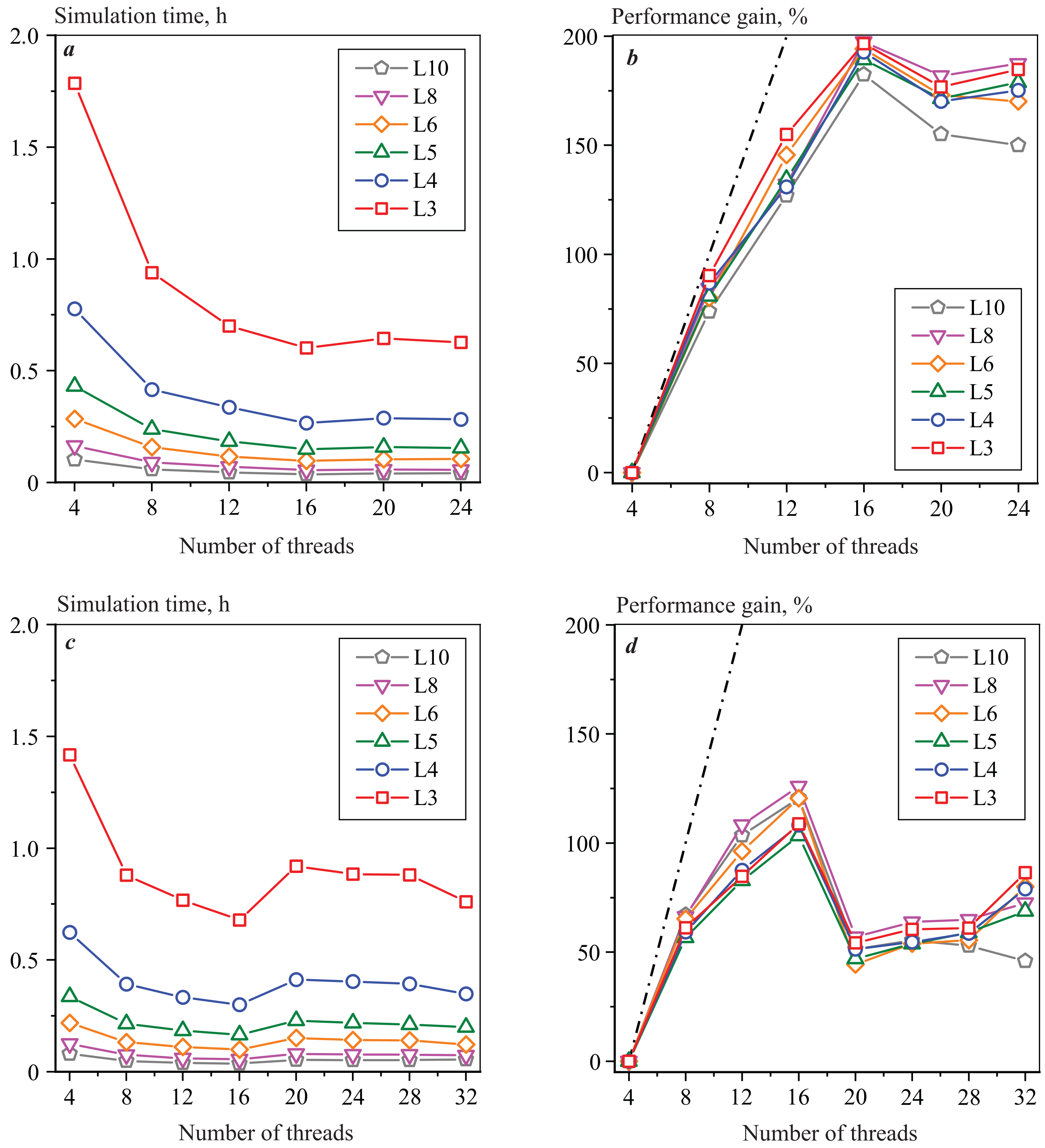

Fig. 3. The calculation time of GP25 casting solidification in ProCast (***a***, ***c***) and the calculation speed growth (***b***, ***d***) depending on the number of threads involved in the calculation, when using computers based on the platforms from Intel (***a***, ***b***) and AMD (***c***, ***d***) and L3–L10 simulation meshes (see Table 2)

Рис. 3. Длительность расчета затвердевания отливки «ГП25» в программе «ProCast» (***a***, ***c***) и прирост скорости расчета (***b***, ***d***) в зависимости от количества потоков, задействованных в расчете при использовании компьютеров на базе платформ «Intel» (***a***, ***b***) и «AMD» (***c***, ***d***) и варьировании размера элементов расчетных сеток L3–L10 (см. табл. 2)

Figure 3 illustrates the simulation time and performance gain for the GP25 part solidification in ProCast on both the Intel and AMD platforms, as well as the relationship with the number of threads. The simulation time and performance gain trends are consistent with those observed in the mold-filling simulation. The only difference is that the solidification simulation is shorter in duration.

Figure 3, *b* presents the performance gain versus the number of threads on the Intel platform. The gain is 73 % to 90 % for 8 threads instead of 4, and 182 % to 197 % for 16 threads instead of 4. Thus, multithreading exhibits slightly higher efficiency in the solidification simulation compared to the mold-filling simulation. This observation holds true for AMD processors as well. One possible explanation for this difference is that during solidification simulation, the distribution of mesh nodes between threads remains constant, whereas during mold-filling simulation, a portion of the CPU time is spent on redistributing nodes between threads.

Figure 4 displays the GP25 part solidification simulation time in PoligonSoft CCS on the Intel platform, along with the performance gain in relation to the number of threads for L3—L10 FEM meshes.

As the number of threads increases, the simulation time decreases and reaches its minimum when using 24 threads. However, the performance gain diminishes with a larger number of threads (Fig. 4, *b*): 23 % to 38 % for 8 threads instead of 4, and 34 % to 65 % for 24 threads. Therefore, increasing the number of threads beyond 8 does not yield significant performance gains. Additionally, as the mesh size decreases and the number of FEM elements increases, there is an almost twofold increase in performance.

Similar to ProCast, analyzing the CPU load is necessary to understand the potential causes of performance degradation and inefficient parallelization of the simulation in PoligonSoft. However, it is challenging to precisely determine how the cores are utilized as the number of threads varies due to PoligonSoft's use of the SMP architecture. The Task Manager

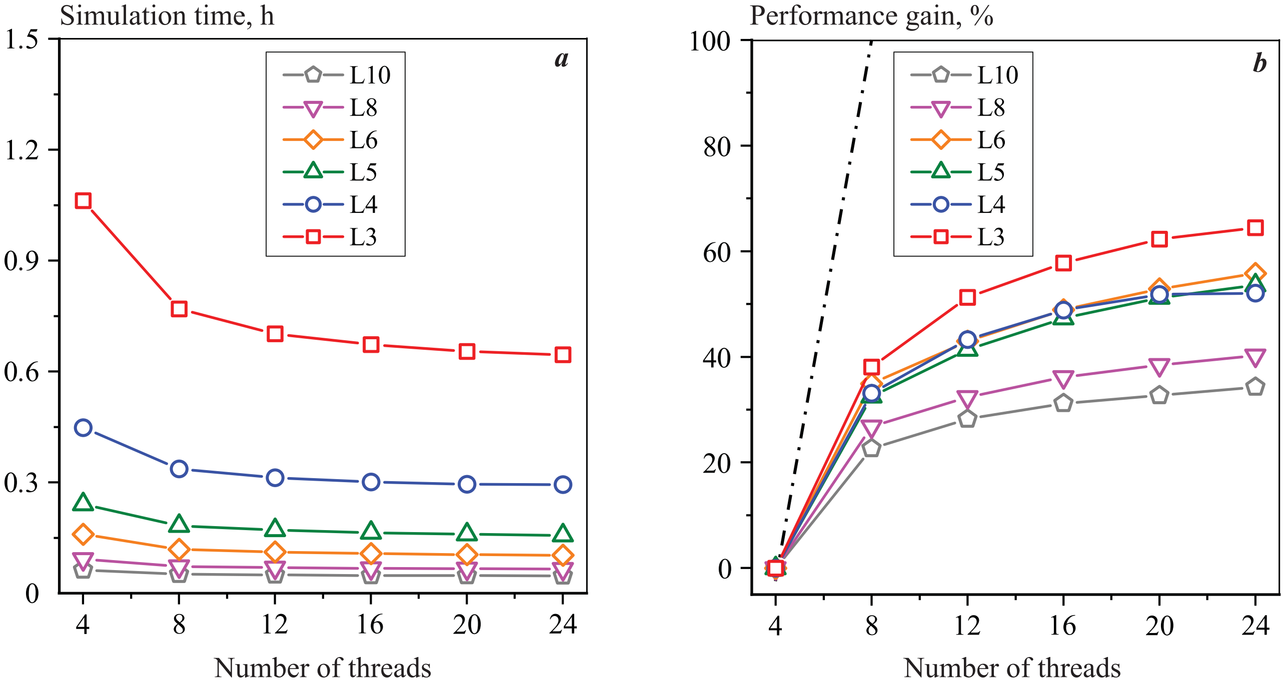

Fig. 4. The calculation time of GP25 casting solidification in PoligonSoft software (***a***) and the calculation speed growth (***b***) depending on the number of threads involved in the calculation, when using computer based on Intel platform and L3—L10 simulation meshes (see Table 2)

Рис. 4. Длительность расчета затвердевания отливки «ГП25» в программе «ПолигонСофт» (***а***) и прирост скорости расчета (***б***) в зависимости от количества потоков, задействованных в расчете при использовании компьютера на базе платформы «Intel» и варьировании размера элементов расчетных сеток L3—L10 (см. табл. 2)

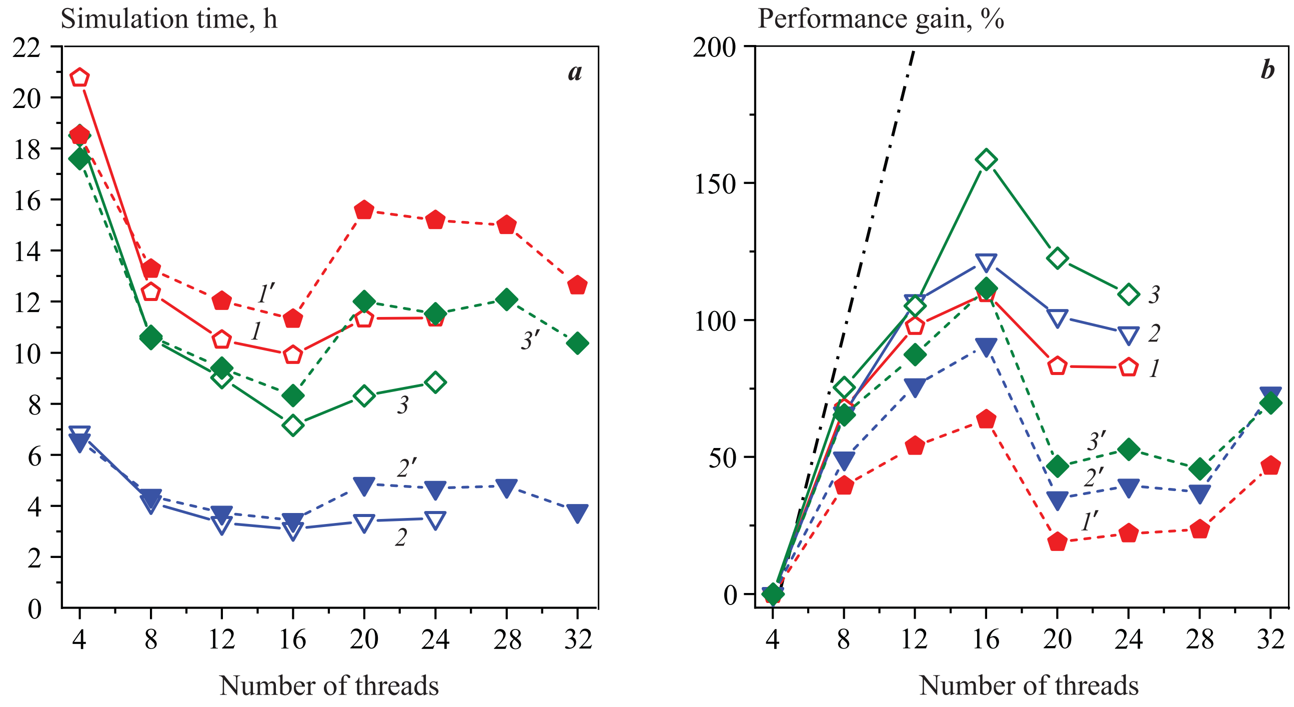

Fig. 5. The calculation time of "body" castings filling and solidification in ProCast (***a***) and the calculation speed growth (***b***) depending on the number of threads involved in the calculation, when using computers based on the platforms from Intel (open points ***1–3***) and AMD (filled points ***1′–3′***)

1, *1′*, *2*, *2′*, *3*, *3′* – numbers of castings "Body"

Рис. 5. Длительность расчета заполнения и затвердевания отливок «Корпус» (см. табл. 2) в программе «ProCast» (***a***) и прирост скорости расчета (***b***) в зависимости от количества потоков, задействованных в расчете при использовании компьютеров на базе платформ «Intel» (пустые точки ***1–3***) и AMD (закрашенные точки ***1′–3′***)

1, *1′*, *2*, *2′*, *3*, *3′* – номера отливок «Корпус»

shows only one process regardless of the actual number of threads. The available information pertains of the load of logical cores from this process, expressed as a percentage for the P and E cores. With 4 threads, only the P cores are loaded, with load varying between 10 % and 22 %. It is worth noting that 22 % represents the peak value reached intermittently, while most of the time, the load remains around 10 %. When the number of threads is increased to 12, both the P cores (20 % to 37 %) and E cores (10 % to 21 %) are utilized. At the maximum number of threads, the load is identical for both P and E cores, and ranging from 20 % to 60 %. The solidification simulation in PoligonSoft significantly underutilizes the CPU due to the less efficient shared memory parallelization (SMP) architecture employed, as opposed to the DMP (Distributed Memory Parallelism) architecture utilized in ProCast, where a specific amount of memory is allocated to each logical core.

Figure 5 illustrates the simulation time for mold filling and solidification of the Casing parts in ProCast, as well as the performance gain in relation to the number of threads for both Intel and AMD computers. This FEM analysis focuses on simulating the cooling of the mold before filling and includes radiation heat transfer. The observed relationships for the GP25 part are consistent with those observed for the Casing part. In both Intel and AMD processors, maximum performance is achieved with 16 threads. With 4 threads, the AMD processor exhibits slightly higher efficiency. However, if the number of threads exceeds 8, the Intel processor becomes more efficient. This difference in performance is likely attributed to the higher clock frequency of the P cores in Intel processor and the use of DDR5 RAM in the Intel computer, as opposed to DDR4 in the AMD computer. The lower performance of the Intel computer with 4 threads is probably due to the predominantly loaded low-performance, energy-efficient E cores (as indicated in Table 3). As the number of threads surpasses 8, the Intel computer utilizes more high-performance cores, while the AMD computer gradually reduces the clock frequency of its

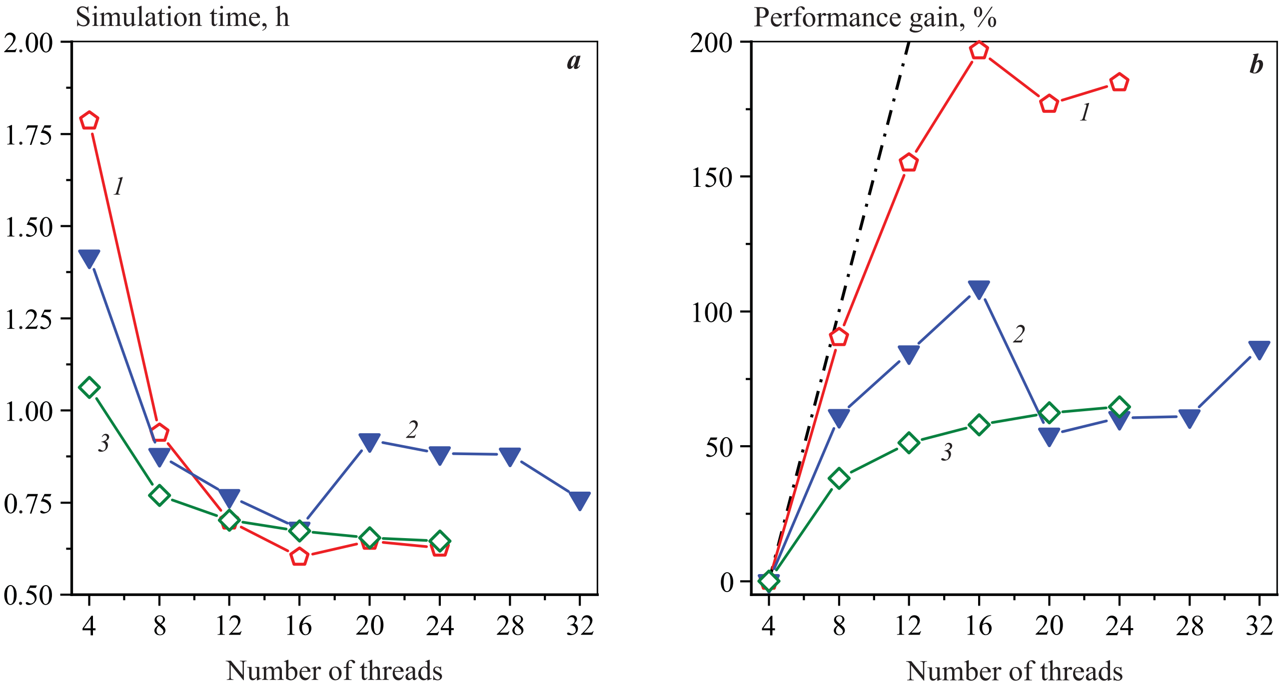

Fig. 6. The calculation time of GP25 casting solidification (***a***) in ProCast (***1***, ***2***) and PoligonSoft (***3***) software and the calculation speed growth (***b***) depending on the number of threads involved in the calculation, when using computers based on the platforms from Intel (open points ***1***, ***3***) and AMD (filled points ***2***) and L3 simulation mesh (see Table 2)

Рис. 6. Длительность расчета затвердевания отливки ГП25 (***a***) и прирост скорости расчета (***b***) в программах «ProCast» (***1***, ***2***) и «ПолигонСофт» (***3***) в зависимости от количества потоков, задействованных в расчете при использовании компьютеров на базе платформ «Intel» (пустые точки ***1***, ***3***) и «AMD» (закрашенные точки ***2***) и расчетной сетки L3 (см. табл. 2)

physical cores. The casting simulation of the GP25 part did not reveal any correlation between the FEM mesh size and the efficiency of parallelism. Similarly, such a relationship was not observed for the Casing parts.

Figure 6 presents the solidification simulation times for the GP25 part in both ProCast and PoligonSoft, as well as the performance gain in relation to the number of threads for Intel and AMD computers. The simulation was conducted using the L3 mesh, which represents the minimum mesh size and the maximum number of FEM elements (as specified in Table 2). Regarding the performance of the ProCast simulation, unlike the casting analysis of the Casing part, the AMD computer demonstrated greater efficiency with 4 and 8 threads, while the Intel computer performed better with a higher number of threads. The potential reasons for this discrepancy are discussed in the earlier section on the Casting part simulation results. It should be noted that the specific number of threads at which one system outperforms the other can vary depending on the specific simulation problem. In general, it is worth noting that the GP25 part solidification simulation in PoligonSoft exhibited faster performance with a small number of threads compared to ProCast. However, when utilizing 16 threads with an Intel processor, ProCast proved to be faster.

It should be noted that the comparison between PoligonSoft and ProCast simulation times is approximate due to potential differences in their FEM algorithms. Therefore, this comparison serves only as a reference and cannot be considered definitive. However, based on the available data, it can be concluded that the solidification simulation times for the same casting parts in ProCast and PoligonSoft are roughly similar.

Despite the diminishing efficiency of parallelism with an increasing number of threads, modern processors equipped with multiple physical and logical cores can still significantly reduce the simulation time for both mold filling and solidification processes. This accelerated simulation enables casting engineers to explore more casting process options, make better-informed decisions, and ultimately enhance the quality of the castings produced. This is particularly crucial when dealing with large, thin-walled parts, which typically involve a vast number of FEM elements and extended simulation durations.

Conclusions

1. The optimal filling and solidification simulation time for the GP25 part in ProCast is achieved with 16 threads on both the Intel Core I9 12900KF and AMD Ryzen 9 5950X CPUs. By using 16 threads instead of 4, the Intel computer experiences a performance gain of approximately 180 %, while the AMD computer shows a gain of around 110 %.

2. The performance decrease obserbed when using more than 16 threads can be attributed to several factors. In the case of Intel processors, the presence of slower, energy-efficient cores contributes to the decrease in performance. Similarly, AMD processors experience decreasing of CPU frequency, which impacts their overall performance. Additionally, both computers exhibit an uneven load distribution between threads due to the full utilization of physical cores.

3. PoligonSoft's parallel GP25 part casting simulation exhibits significantly lower efficiency compared to ProCast. This is primarily due to PoligonSoft's SMP (shared memory parallelization) architecture, which underutilizes the logical cores available. As a result, the performance gain achieved when using 24 threads instead of 4 does not exceed 65 %.

4. Despite the notable difference in parallelization efficiency, the GP25 part's solidification simulation times in PoligonSoft and ProCast remain relatively close.

5. When conducting a more complex simulation of a large-size VZHL14H-VI nickel superalloy part casting in ceramic molds using ProCast, which includes accounting for mold cooling, melt pouring, and subsequent cooling with radiation heat transfer, the parallelization efficiency remains consistent with that observed in the GP25 part simulation.

References

1. Schwiegelshohn U., Badia R.M., Bubak M., Danelutto M., Dustdar S., Gagliardi F., Geiger A., Hluchy L., Kranzlmüller D., Laure E., Priol T., Reinefeld A., Resch M., Reuter A., Rienhoff O., Rüter T., Sloot P., Talia D., Ullmann K., Yahyapour R., von Voigt G. Perspectives on grid computing. *Future Generation Computer Systems.* 2010;26:1104—1115. https://doi.org/10.1016/j.future.2010.05.010
2. Konopka K., Miłkowska-Piszczek K., Trebacz L., Falkus J. Improving efficiency of ccs numerical simulations through use of parallel processing. *Archives of Metallurgy and Materials.* 2015;60(1):235—238. https://doi.org/10.1515/amm-2015-0037
3. Istomin V.A., Shvarts D.R., Ishkhanov E.A., Tikhomirov M.D. Using the meshfree smoothed-particles method in the simulation of hydrodynamics in the casting simulation software "PoligonSoft". *Liteinoe Proizvodstvo.* 2012;(8):20—22 (In Russ.).
   Истомин В.А., Шварц Д.Р., Ишханов Е.А., Тихомиров М.Д. Использование бессеточного метода сглаженных частиц при моделировании гидродинамики в СКМ ЛП «ПолигонСофт». *Литейное производство.* 2012;(8):20—22.
4. Cai Y., Li G., Wang H., Zheng G., Lin S. Development of parallel explicit finite element sheet forming simulation system based on GPU architecture. *Advances in Engineering Software.* 2012;45:370—379. https://doi.org/10.1016/j.advengsoft.2011.10.014
5. Posey S., Kodiyalam S. Performance benefits of NVIDIA GPUs for LS-DYNA®. In: *8th European LS-DYNA Users Conference* (May 2011). Strasbourg, 2011. P. 1—6.
6. Kaplinger B., Wie B., Dearborn D. Efficient parallelization of nonlinear perturbation algorithms for orbit prediction with applications to asteroid deflection and fragmentation. In: *20th AAS/AIAA Space Flight Mechanics Meeting* (15—17 February 2010). San Diego, 2010. P. 1845—1860.
7. Thibault S.E., Holman D., Trapani G., Garcia S. CFD simulation of a quad-rotor UAV with rotors in motion explicitly modeled using an LBM approach with adaptive refinement. In: *55th AIAA Aerospace Sciences Meeting* (9—13 January 2017). Grapevine: American Institute of Aeronautics and Astronautics, 2017. P. 1—16. https://doi.org/10.2514/6.2017-0583
8. Pannala S., D'Azevedo E.F., Syamlal M. O'Brien T. Hybrid (OpenMP and MPI) parallelization of MFIX: A multiphase CFD code for modeling fluidized beds. In: *Proceedings of the ACM Symposium on Applied Computing (SAC)* (9—12 March 2003). Melbourne: Association for Computing Machinery, 2003. P. 199—206. https://doi.org/10.1145/952532.952574

9. Tomsich P., Rauber A., Merkl D. ParSOM: Using parallelism to overcome memory latency in self-organizing neural networks. In: *High Performance Computing and Networking:* Proceedings of the 8th International Conference (8—10 May 2000). Amsterdam: Springer, 2000. P. 136—145.
https://doi.org/10.1007/3-540-45492-6_15
10. Bilenko G.A. General capabilities of the software package Welding simulation suite. *Metallurgist.* 2011;55(5—6): 323—327. (In Russ.).
https://doi.org/10.1007/s11015-011-9430-6
Биленко Г.А. Общие возможности пакета программ Welding simulation suite. *Металлург.* 2011;(5):28—31.
11. Yang W.-H., Peng A., Liu L., Hsu D.C. Parallel true 3D CAE with hybrid meshing flexibility for injection molding. In: *Annual Conference of the Society of Plastics Engineers ANTEC 2005* (1—5 May 2005). Boston: Curran Associates Inc., 2005. Vol. 1. P. 56—60.
12. Corke G. Workstations for simulation (FEA). URL: https://develop3d.com/features/workstations-for-simulation-fea-ansys-mechanical-17-0 (accessed: 17.01.2023).
13. Trębacz L., Miłkowska-Piszczek K., Konopka K., Falkus J. Numerical simulation of the continuous casting of steel on a grid platform. In: *eScience on distributed computing infrastructure. Lecture notes in computer science* (Eds. M. Bubak, J. Kitowski, K. Wiatr). Heidelberg: Springer, 2014. Vol. 8500. P. 407—418.
https://doi.org/10.1007/978-3-319-10894-0_29
14. Tikhomirov M.D., Komarov I.A. Principles of simulation of casting processes. Which is better, the finite element method or the finite difference method? *Liteinoe Proizvodstvo.* 2002;(5):22—28. (In Russ.).
Тихомиров М.Д., Комаров И.А. Основы моделирования литейных процессов. Что лучше — метод конечных элементов или метод конечных разностей? *Литейное производство.* 2002;(5):22—28.
15. Tarasevich N.I., Korniets I.V., Tarasevich I.N., Dudchenko A.V. Comparative analysis of computer simulation software for metallurgical and foundry processes. *Metall i Lit'e Ukrainy.* 2010;(5):20—25. (In Russ.).
Тарасевич Н.И., Корниец И.В., Тарасевич И.Н., Дудченко А.В. Сравнительный анализ систем компьютерного моделирования металлургических и литейных процессов. *Металл и литье Украины.* 2010;(5):20—25.
16. Simulate the complete casting process to reach zero defects with a single tool. URL: https://www.esi-group.com/products/casting (accessed: 6.02.2023).
17. Turishchev V. Simulation of foundry processes: What to choose? *CADmaster.* 2005;(2):33—35. (In Russ.).
Турищев В. Моделирование литейных процессов: Что выбрать? *CADmaster.* 2005;(2):33—35.
18. Casting processes computer simulation system (CSS CP) «PoligonSoft». (In Russ.). URL: https://poligonsoft.ru (accessed: 6.02.2023).
Система компьютерного моделирования литейных процессов (СКМ ЛП) «ПолигонСофт». URL: https://poligonsoft.ru (дата обращения: 6.02.2023).
19. Monastyrskii A., Tikhomirov M. The casting simulation software "PoligonSoft" 13.X. Overview, results, plans. *CADmaster.* 2013;(2):44—48. (In Russ.).
Монастырский А., Тихомиров М. СКМ ЛП «ПолигонСофт» 13.Х. Обзор, итоги, планы. *CADmaster.* 2013;(2):44—48.
20. ESI Group, ProCAST 2010.0 User's Manual (ESI Group, 2010). URL: https://myesi.esi-group.com/system/files/documentation/ProCAST/2010/ProCAST_20100_UM.pdf (accessed: 12.09.2022).
21. Yang L., Chai L.H., Liang Y.F., Zhang Y.W., Bao C.L., Liu S.B., Lin J.P. Numerical simulation and experimental verification of gravity and centrifugal investment casting low pressure turbine blades for high Nb—TiAl alloy. *Intermetallics.* 2015;66:149—155.
https://doi.org/10.1016/j.intermet.2015.07.006
22. Lu S., Xiao F., Guo Z., Wang L., Li H., Liao B. Numerical simulation of multilayered multiple metal cast rolls in compound casting process. *Applied Thermal Engineering.* 2016;93:518—528.
https://doi.org/10.1016/j.applthermaleng.2015.09.114
23. Dantzig J.A., Rappaz M. Solidification. Lausanne: EPFL Press, 2009. 621 p.
24. Tikhomirov M.D. Main aspects of solving the heat transfer problem in the simulation of foundry processes. *Liteinoe Proizvodstvo.* 1998;(4):30—34. (In Russ.).
Тихомиров М.Д. Основные аспекты решения тепловой задачи при моделировании литейных процессов. *Литейное производство.* 1998;(4):30—34.
25. Koltygin A.V., Bazhenov V.E., Tseloval'nik Yu.V., Belov V.D., Yudin V.A. Results of computer of shrinkage microporosity simulation in ML10 alloy body casting. *Liteinoe Proizvodstvo.* 2020;(8):23—27. (In Russ.).

Колтыгин А.В., Баженов В.Е., Целовальник Ю.В., Белов В.Д., Юдин В.А. Результаты компьютерного моделирования усадочной микропористости в корпусной отливке из сплава МЛ10. *Литейное производство.* 2020;(8):23—27.

26. Palumbo G., Piglionico V., Piccininni A., Guglielmi P., Sorgente D., Tricarico L. Determination of interfacial heat transfer coefficients in a sand mould casting process using an optimised inverse analysis. *Applied Thermal Engineering.* 2015; 78:682—694.
https://doi.org/10.1016/j.applthermaleng.2014.11.046
27. Bazhenov V.E., Petrova A.V., Koltygin A.V., Tseloval'nik Yu.V. Determination of the interfacial heat transfer coefficient between AZ91 alloy casting and resin bonded sand mold. *Tsvetnye Metally.* 2017;(8):89—96. (In Russ.).
https://doi.org/10.17580/tsm.2017.08.14
Баженов В.Е., Петрова А.В., Колтыгин А.В., Целовальник Ю.В. Определение коэффициента теплопередачи между отливкой из сплава МЛ5 (AZ91) и формой из холоднотвердеющей смеси. *Цветные металлы.* 2017;(8):89—96.
28. Bazhenov V.E., Tselovalnik Yu.V., Koltygin A.V., Belov V.D. Investigation of the interfacial heat transfer coefficient at the metal—mold interface during casting of an A356 aluminum alloy and AZ81 magnesium alloy into steel and graphite molds. *International Journal of Metalcasting.* 2021;15(2):625—637.
https://doi.org/10.1007/s40962-020-00495-2

Information about the authors

Viacheslav E. Bazhenov – Cand. Sci. (Eng.), Assistant Prof., Department of Foundry Technologies and Material Art Working (FT&MAW), National University of Science and Technology “MISIS” (NUST MISIS).
https://orcid.org/0000-0003-3214-1935
E-mail: V.E.Bagenov@gmail.com

Andrey V. Koltygin – Cand. Sci. (Eng.), Assistant Prof., Department of FT&MAW, NUST MISIS.
https://orcid.org/0000-0002-8376-0480
E-mail: misistlp@mail.com

Anna A. Nikitina – Educat. Master, Department of FT&MAW, NUST MISIS.
https://orcid.org/0000-0002-5399-0330
E-mail: nikitina.misis@gmail.com

Vladimir D. Belov – Dr. Sci. (Eng.), Head of the Department of FT&MAW, NUST MISIS.
https://orcid.org/0000-0003-3607-8144
E-mail: vdbelov@mail.ru

Evgenii A. Lazarev – Head Metallurgist of the PJSC “UEC-Kuznetsov”.
E-mail: ea.lazarev@uec-kuznetsov.ru

Информация об авторах

Вячеслав Евгеньевич Баженов – к.т.н., доцент кафедры литейных технологий и художественной обработки материалов (ЛТиХОМ) Национального исследовательского технологического университета «МИСИС» (НИТУ МИСИС).
https://orcid.org/0000-0003-3214-1935
E-mail: V.E.Bagenov@gmail.com

Андрей Вадимович Колтыгин – к.т.н., доцент кафедры ЛТиХОМ, НИТУ МИСИС.
https://orcid.org/0000-0002-8376-0480
E-mail: misistlp@mail.ru

Анна Андреевна Никитина – учебный мастер кафедры ЛТиХОМ, НИТУ МИСИС.
https://orcid.org/0000-0002-5399-0330
E-mail: nikitina.misis@gmail.com

Владимир Дмитриевич Белов – д.т.н., заведующий кафедрой ЛТиХОМ, НИТУ МИСИС.
https://orcid.org/0000-0003-3607-8144
E-mail: vdbelov@mail.ru

Евгений Алексеевич Лазарев – главный металлург ПАО «ОДК-Кузнецов».
E-mail: ea.lazarev@uec-kuznetsov.ru

Contribution of the authors

V.E. Bazhenov – conceptualization, realization of simulation, analysis of the simulation results, writing of the manuscript.

A.V. Koltygin – scientific guidance, review and editing of the manuscript.

A.A. Nikitina – realization of simulation, analysis of the simulation results.

V.D. Belov – supervision, review and editing of the manuscript.

E.A. Lazarev – formulation of the aims and objectives of the study, provision of resources.

Вклад авторов

В.Е. Баженов – формирование основной концепции, проведение расчетов, обработка результатов расчетов, написание текста статьи.

А.В. Колтыгин – научное руководство, редактирование текста статьи.

А.А. Никитина – проведение расчетов, обработка результатов расчетов.

В.Д. Белов – общее руководство, редактирование текста статьи.

Е.А. Лазарев – формулировка цели и задачи исследования, обеспечение ресурсами.

The article was submitted 09.02.2023, revised 22.03.2023, accepted for publication 24.03.2023

Статья поступила в редакцию 09.02.2023, доработана 22.03.2023, подписана в печать 24.03.2023

FOUNDRY / ЛИТЕЙНОЕ ПРОИЗВОДСТВО

UDC 621.74.045 : 53.09
https://doi.org/10.17073/0021-3438-2023-3-54-66

Research article
Научная статья

Porous wax patterns for high-precision investment casting

S.G. Zhilin, N.A. Bogdanova, O.N. Komarov

Institute of Machinery and Metallurgy of Far-Eastern Branch of the Russian Academy of Sciences
681005, Russia, Khabarovsk region, Komsomolsk-on-Amur, Metallurgists str., 1

✉ Sergey G. Zhilin (sergeyzhilin1@rambler.ru)

Annotation: Aerospace, manufacturing, and shipbuilding industries strive to enhance their competitiveness by optimizing material utilization and improving production processes. The investment casting process offers the capability to fabricate intricate and precise components using a diverse range of alloys. However, this method is not without its drawbacks, including high manufacturing costs and a significant rate of defective castings, which can reach up to 30 %. These defects primarily arise from the stresses imposed on the wax patterns and ceramic molds,leading to their distortion. To address this issue, efforts have been made to reduce stress by employing compacted wax powders for the production of investment patterns. However, stress relaxation in the wax patterns remains a concern as it can result in elastic deformation of the compacted material and subsequent alterations in the final product dimensions. To mitigate this issue, a series of tests were conducted with the objective of studying stress relaxation under constant compression strain, as described by the Kohlrausch equation. The obtained results provide valuable insights that enable the prediction of the ultimate dimensions of patterns created using different grades of wax.

Keywords: testing, manufacturing process, investment casting, stress-strain state, compaction, porosity, elastic deformation.

Acknowledgments: This study has received financial support from the Khabarovsk Federal Research Center, Far East Branch, Russian Academy of Sciences. The authors acknowledge the utilization of the Research Data Processing and Storage Center, Far East Branch, Russian Academy of Science, which is funded by the Russian government through the Ministry of Science and Higher Education under Project No. 075-15-2021-663.

For citation: Zhilin S.G., Bogdanova N.A., Komarov O.N. Porous wax patterns for high-precision investment casting. *Izvestiya. Non-Ferrous Metallurgy*. 2023;29(3):54–66. https://doi.org/10.17073/0021-3438-2023-3-54-66

Исследование процессов формирования пористых выплавляемых моделей, применяемых для изготовления высокоточного литья

С.Г. Жилин, Н.А. Богданова, О.Н. Комаров

Институт машиноведения и металлургии Дальневосточного отделения Российской академии наук
681005, Россия, Хабаровский край, г. Комсомольск-на-Амуре, ул. Металлургов, 1

✉ Сергей Геннадьевич Жилин (sergeyzhilin1@rambler.ru)

Аннотация: Конкурентоспособность современных предприятий машино-, судо- и авиастроения во многом определяется материало- и энергоэффективностью технологий, направленных на получение конструкций и узлов деталей ответственного назначения. Применение литья по выплавляемым моделям (ЛВМ) обеспечивает получение заготовок повышенной размерной и геометрической точности, сложной пространственной конфигурации из широкой номенклатуры сплавов. К недостаткам ЛВМ следует отнести многостадийность процесса и высокую стоимость конечного продукта, что предполагает недопустимость брака, доля которого может достигать 30 %. Брак в ЛВМ преимущественно вызван теплофизическими явлениями, сопровождающими ряд технологических операций и обусловливающими наличие напряжений в структуре воскообразных и керамических материалов, что определяет деформационные процессы в выплавляемых моделях и оболочковых формах. Для устранения негативного влияния теплофизического фактора и снижения напряжений в структурах промежуточных изделий процесса, выплавляемые модели формируют прессованием порошков воскообразных модельных композиций. При этом нерешенным остается вопрос релаксации напряжений в прессовках, приводящих к упругому отклику уплотненного материала и, как следствие, изменению размеров получаемого изделия. Поиск вариантов наиболее рационального режима формирования прессовки привел к необходимости проведения серии экспериментов, в результате которых предполагается достижение релаксации напряжений σ в условиях постоянной деформации сжатия, описываемого уравнением Кольрауша. Полученные в ходе эксперимента результаты позволят прогнозировать конечные размеры прессовок и сформировать математическую модель процесса, актуальную для широкой номенклатуры воскообразных модельных материалов, применяемых в ЛВМ.

Ключевые слова: экспериментальное моделирование, машиностроительные процессы, литье по выплавляемым моделям, напряженно-деформированное состояние, прессовка, пористость, упругий отклик.

Благодарности: Работа выполнена в рамках государственного финансирования Хабаровского федерального исследовательского центра ДВО РАН. Исследования проведены с использованием ресурсов ЦКПН «Центр обработки и хранения научных данных ДВО РАН», финансируемого Российской Федерацией в лице Министерства науки и высшего образования Российской Федерации по проекту № 075-15-2021-663.

Для цитирования: Жилин С.Г., Богданова Н.А., Комаров О.Н. Исследование процессов формирования пористых выплавляемых моделей, применяемых для изготовления высокоточного литья. *Известия вузов. Цветная металлургия*. 2023;29(3):54–66. https://doi.org/10.17073/0021-3438-2023-3-54-66

Introduction

Various industries, including manufacturing, aerospace, and shipbuilding, strive to maintain their competitiveness by reducing production costs while ensuring product quality. Renowned marine engine manufacturers (Wärtsila, Caterpillar, Volvo Penta, MTU, Cummins, etc.) achieve cost reduction through the implementation of reuse and circular processes [1], thereby ensuring long-term competitiveness. The introduction of advanced technologies and innovative manufacturing equipment may result in a significant increase in the final product cost [2]. One approach to cost control during the initial stages of manufacturing, is the use of workpiece casting. For parts subjected to cyclic mechanical and thermal loads, castings should possess high structural strength [3] or hardness [4]. Special requirements also apply to titanium alloy castings and castings for offshore drilling equipment, particularly when centrifugal casting is employed [5], or high dimensional and geometric accuracy is expected.

In shipbuilding, ship propellers represent the largest castings and are typically manufactured using eutectic and near-eutectic high-entropy alloys. These alloys offer high strength and ductility, making them suitable for various operating temperatures [6]. Researchers worldwide are dedicated to enhancing casting quality, improving final product outcomes, and developing new casting repair technologies [7—9].

Simulation plays a crucial role in achieving high-precision casting and reducing defects, as well as operating costs. For example, simulation tools (FEM, volume difference method; vector element or vector gradient methods, etc.) can model the shrinkage that occurs in sandy clay mold casting. The extent of shrinkage is influenced by numerous thermophysical properties of the alloy [10; 11]. It is important to verify the simulation results through physical testing, as most casting simulation tools rely on certain approximate assumptions.

While several codes are available for analyzing conventional sand and clay mold casting processes (e.g., casting of ship propellers and other large ship components), only a limited number of tools can effectively simulate special casting processes such as centrifugal casting, injection molding, or investment casting [12]. Investment casting, in particular, presents significant challenging for analysis due to the multitude of factors that affect casting quality.

The investment casting process is a multi-stage procedure designed for manufacturing large, solid, complex-shaped parts. In some cases, additional machining processes are not required [13]. With the investment casting process, castings up to 500 mm in size can be produced with a wall thickness of up to 1 mm and a surface roughness of up to R_a = 1.25 μm. The ISO tolerance grade of the casting typically ranges from 11 to 16, provided that the mold tolerances do not exceed grade 8 or 9.

The standard process for investment casting typically involves the following steps:

— manufacturing and assembly of wax patterns;

— layer-by-layer formation of a ceramic shell around the patterns;

— heating and removal of the wax from the mold;

— baking the mold and filling it with molten metal;

— machining of the final cast part.

During the investment casting process, there is a volume variation in the part due to shrinkage or thermal expansion, which can reach 10—14 %. To determine the necessary machining allowances for the casting, it is essential to consider the thermophysical processes involved in metal heating and cooling [14; 15]. These processes can potentially result in manufacturing defects. Investment casting is known for its relatively high defect rate, which can be as high as 30 % [16; 17]. Several negative factors contribute to these defects, including:

— changes in the temperature of wax pattern, leading to surface delamination, shrinkage, or buckling once it is placed into the mold;

— ingress of melted wax into the ceramic mold material during the wax removal process, causing mold destruction during the baking or filling stages.

Figure 1 illustrates a flowchart depicting the occurrence of defects in investment casting. The flowchart includes the following stages:

1 — wax shrinkage, resulting in distortion of the casting geometry:

2 — cracks in the ceramic mold layers caused by the thermal expansion of the wax during heating and removal;

3 — wax expansion in the ceramic shell pores during

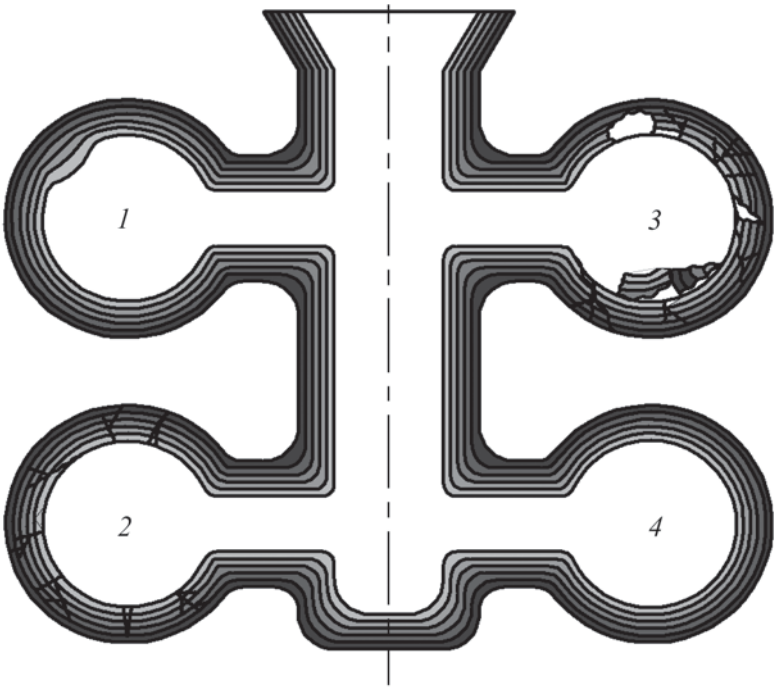

Fig. 1. Investment casting defect formation flowchart for a 5-layer ceramic shell mold

Рис. 1. Схема последовательности появления типичных дефектов, характерных для различных этапов получения отливок методом ЛВМ, на примере 5-слойной керамической оболочковой формы baking, leading to ceramic fragments getting into the casting;

4 — defect-free ceramic mold cavity.

To mitigate shrinkage-related issues, conventional anti-shrinkage measures include using materials with the required rheological properties or controlling such properties, as well as casting within a narrow temperature range [18; 19].

Casting is a complex and costly process, and any defects are deemed unacceptable, which has prompted the exploration of alternative casting methods.

However, the utilization of new or improved wax materials can result in additional expenses. Most commonly, oil paraffin waxes are employed along with various additives such as stearin, ceresin, rosin, and brown coal wax. One commonly used wax is PS50/50, which is a blend consisting of equal weights of paraffin and stearin [13].

During the solidification of PS50/50 wax, stresses develop within the investment pattern, leading to cracking and chipping. Consequently, enhancing casting accuracy becomes challenging. To address this issue, the preferable approach is to create investment patterns using wax powder due to its superior manufacturability. This method helps reduce stress and allows for improved accuracy, as the powdered material can penetrate even the most intricate cavities [20; 21].

The cold compaction of wax powder in the casting process introduces various factors such as interparticle friction, friction against the mold walls [22], and temperature rise. As the wax grains come into contact, they melt and form a porous matrix that matches the configuration of the mold cavity, thereby preventing shrinkage defects in both the investment pattern and the mold walls.

However, there are drawbacks of this process, including potential geometry distortions when the pressurized air is released and the compacted wax expands. Experimental measurements have shown that the elastic deformation of the wax after the load is removed ranges from 0.7 to 1.2 % in the direction of compression and from 0.4 to 0.5 % in the transverse direction [23]. Compared to liquid or paste-like materials, powder wax cores maintain their dimensions more effectively [24; 25]. While acceptable casting accuracy can be achieved with powder wax patterns, there is still a need to address distortions through experimental studies on the elastic distortion of wax after compaction.

The extent of distortion is influenced by the rheological properties of the wax, including elasticity, plasticity, strength, ductility, and creep. Cold compaction can result in local overheated spots. The magnitude of elastic distortion depends on the stress relaxation time, which is affected by particle size, compaction pressure, and rate. Stress levels increase with greater compaction intensity. The study aimed to determine the point at which the elastic deformation of a compacted material under a constant load becomes irreversible (plastic) [26; 27]. Initial findings revealed that when the compaction (mold closing) rate ranges from 0.25 to 1.5 mm/s, the distortion of powder wax does not exceed 1.2 % in the direction of compaction. The application of forced relaxation by allowing the wax to dwell in the mold under load helps redistribute stress and reduces distortion.

The objective of this study was to compare computational and experimental properties of wax powder to predict dimensional deviations in porous wax patterns relative to the mold cavity dimensions.

The research workflow involved the following steps:

— testing to obtain the stress vs. porosity relationship for powder wax compaction;

— comparison of simulated stress values with actual measurements;

— determination of the factors in the stress relaxation equation for powder wax patterns.

Materials and methods

In order to determine the stress (σ) resulting from variations in strain (ε) over time (τ), we applied the rheological equation:

$$f(\sigma,\varepsilon,\tau) = 0. \tag{1}$$

For the compaction tests of the powder wax, a constant compressive strain (ε = const) was maintained [28]. During the compaction process, the local temperature rises and reaches the melting point. As the load is removed, the temperature decreases. The stress relaxation (σ) in the solidification region of the wax for a constant strain (ε = const) is described by the Kohlrausch equation [29; 30]:

$$\sigma = \sigma_0 \exp^{-(t/a)^b}, \tag{2}$$

where a and b ($0 < b \le 1$) are constants at a given temperature and pressure, σ represents the stress at time t; σ_0 is the relaxing component of the stress.

We estimated the factors of the Kohlrausch equation that describe the relaxation properties of the compacted wax using the experimental curves presented by Pavlov V. et al. [31]. For a porous body, the analytical expression for the relaxation curve is

$$\sigma = \sigma_0(P)\exp^{-(t/\tau)^k}, \tag{3}$$

where $\sigma_0(P)$ represents the peak stress at the compaction puncheon when unloading begins for the given porosity P.

The values τ and k in the analytical equation of the relaxation of the porous body are determined using the least squares method. To do this, we denote the measured stress $\tilde{\sigma}_i$ at the moment t_i and express it in terms of $\sigma_0(P)$:$\tilde{\sigma}_i = \sigma(t_i)/\sigma_0(P)$. Finding the parameters of expression (3) involves minimizing the generalized scattering index. We applied the method of least squares not to the original exponential function (2), but to its transformed version (3). Since the values $\tilde{\sigma}_i$ fall within the range $0 < \tilde{\sigma}_i \le 1$, then $\ln\tilde{\sigma}_i \le 0$, and therefore the scattering index can be represented as

$$Q = \sum_{i=1}^{n}\left\{\ln(-\ln\tilde{\sigma}_i) - \ln\left[-\ln(\exp^{-(t_i/\tau)^k})\right]\right\}^2 = \\ = \sum_{i=1}^{n}\left[\ln(-\ln\tilde{\sigma}_i) - k\ln(t_i/\tau)\right]^2. \tag{4}$$

When selecting the experimental points, it is importante to consider that when unloading begins at $\tilde{\sigma}_i = 1$ or at $t = 0$, expression (4) does not yet exist. However, we can observe that $\exp^{-(t/\tau)^k}\big|_{t=0} = \tilde{\sigma}_i(t_0) = 1$. We equated the partial derivatives of Q with respect to τ and k to zero:

$$\left.\begin{aligned} \frac{\partial Q}{\partial \tau} &= 2\sum_{i=1}^{n}[\ln(-\ln\tilde{\sigma}_i) - k\ln(t_i/\tau)]\frac{k}{\tau} = 0,\\ \frac{\partial Q}{\partial \tau} &= -2\sum_{i=1}^{n}[\ln(-\ln\tilde{\sigma}_i) - k\ln(t_i/\tau)]\ln(t_i/\tau) = 0. \end{aligned}\right\} \tag{5}$$

By transforming system (5), we obtained the normal equations in their standard form:

$$\left.\begin{aligned} &kn\ln\left(\frac{1}{\tau}\right) + k\sum_{i=1}^{n}\ln t_i = \sum_{i=1}^{n}\ln(-\ln\tilde{\sigma}_i),\\ &k\ln\left(\frac{1}{\tau}\right)\sum_{i=1}^{n}\ln t_i + k\sum_{i=1}^{n}(\ln t_i)^2 = \sum_{i=1}^{n}\ln(-\ln\tilde{\sigma}_i)\ln t_i. \end{aligned}\right\} \tag{6}$$

The solution to system (6) is

$$k\ln\left(\frac{1}{\tau}\right) = \frac{\sum_{i=1}^{n}\ln(-\ln\tilde{\sigma}_i)\sum_{i=1}^{n}(\ln t_i)^2 - \sum_{i=1}^{n}\ln(-\ln\tilde{\sigma}_i)\ln t_i\sum_{i=1}^{n}\ln t_i}{n\sum_{i=1}^{n}(\ln t_i)^2 - \left(\sum_{i=1}^{n}\ln t_i\right)^2},$$

$$k = \frac{n\sum_{i=1}^{n}\ln(-\ln\tilde{\sigma}_i)\ln t_i - \sum_{i=1}^{n}\ln(-\ln\tilde{\sigma}_i)\sum_{i=1}^{n}\ln t_i}{n\sum_{i=1}^{n}(\ln t_i)^2 - \left(\sum_{i=1}^{n}\ln t_i\right)^2}. \tag{7}$$

τ is expressed as

$$\tau = \exp\left[\frac{\sum_{i=1}^{n}\ln(-\ln\tilde{\sigma}_i)\ln t_i\sum_{i=1}^{n}\ln t_i - \sum_{i=1}^{n}\ln(-\ln\tilde{\sigma}_i)\sum_{i=1}^{n}(\ln t_i)^2}{n\sum_{i=1}^{n}\ln(-\ln\tilde{\sigma}_i)\ln t_i - \sum_{i=1}^{n}\ln(-\ln\tilde{\sigma}_i)\sum_{i=1}^{n}\ln t_i}\right]. \tag{8}$$

The k and τ parameters of the Kohlrausch equation (3) were determined through experimental analysis using equations (7) and (8).

For wax testing, we utilixed purified paraffin, specifically T1 grade, as well as a 1 : 1 mixture of paraffin and stearin (PS50/50). These materials, classified as Category 1 [13], are commonly employed in investment casting. As the actual properties of the wax may deviate from specified values (e.g., Solid Petroleum Paraffins. Specifications. GOST 23683-89), we measured the density (ρ) and Young's modulus (E): for T1, ρ = 0.86 g/cm^3, E = 81.91 MPa; for PS50/50, ρ = = 0.935 g/cm^3, E = 71.8 MPa. The melting points of T1 and PS50/50 waxes were determined using a Shimadzu DTG-60H differential thermal analyzer, employing a heating rate of 2 °C/min. The melting points were found to be 58 °C and 52 °C, respectively. Due to the relatively low melting points, we conducted the tests within a narrow ambient temperature range of 20±2 °C to enhance accuracy.

The mold used in the experiments was constructed from steel grade 45 (equivalent to US analog: SA-29 1044). Its cavity took the form of a cylindrical shape with an inner diameter of d = 43.3 mm. The mold was assumed to be rigid and non-deformable. The wax patterns were created using T1 and PS50/50 materials with particle sizes of 0.63 mm and 2.5 mm, selected to optimize manufacturability. The bulk den-

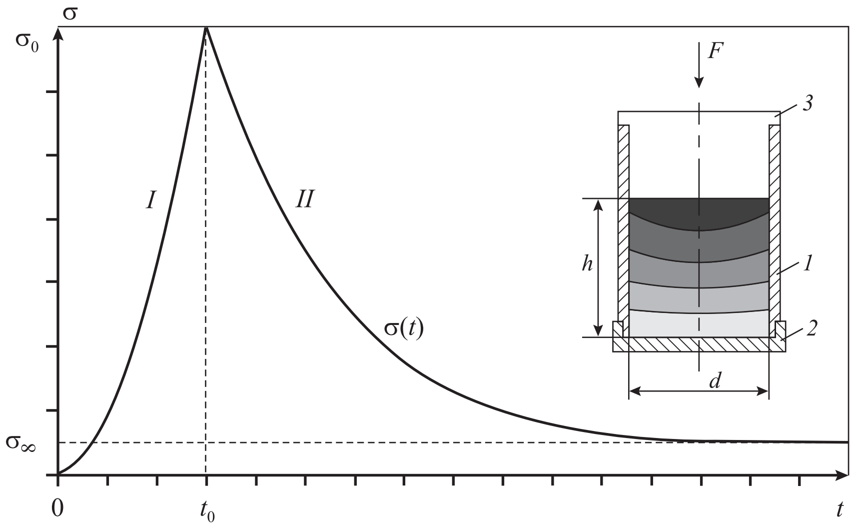

Fig. 2. Loading and relaxation of T1 and PS50 wax powders

I – loading curve, ***II*** – relaxation curve
1 – mold, ***2*** – bottom, ***3*** – puncheon

Рис. 2. Схема нагружения и релаксации порошкового тела из воскообразных материалов Т1 и ПС50/50

I – кривая нагружения, ***II*** – кривая релаксации
1 – пресс-матрица, ***2*** – основание, ***3*** – пресс-пуансон

sity (ρ_{bulk}, g/cm^3) values were as follows: 0.360 (T1, 2.5 mm particle size); 0.320 (T1, 0.63 mm particle size); 0.340 (PS50/50, 2.5 mm particle size); 0.310 (PS50/50, 0,63 mm particle size). The powder was obtained by sieving through 026 sieves, resulting in flake-shaped particles. Consequently, the existing methods used for estimating the final properties of compacted powders with spherical particles [32] were not applicable in this case.

The porosity P of the compacted powders varied within the range of $0\ \% \le P \le 12\ \%$, with increments of 2 %. To control the porosity, we manipulated the deformation (ε) of the powder by moving the puncheon at a rate of 1 mm/s untill the same height matched its diameter ($h = d$, as shown in Fig. 2). Subsequently, we measured the stresses exerted on the sample using an AG-X plus Shimadzu testing machine during a relaxation period of 60 minutes (from t_0 to t_{60}). The maximum load applied was 250 kN. Meeting the machine manufacturer's specifications, a tolerance of 0.03 % was maintained for a load of 100 kN and a deformation of 10 mm, ensuring reliable test results.

Figure 2 illustrates the loading and relaxation process applied to the wax powders during the formation of porous compacted samples using T1 and PS50/50 materials. The porosity of the samples was determined using the following formula

$$P = (1 - \rho_{\text{p}}/\rho_{\text{s}}) \cdot 100\ \%, \qquad (9)$$

where ρ_{p} represents the density of the porous sample, kg/m^3; ρ_{s} represents the density of the solid cast sample, kg/m^3.

To determine the appropriate porosity range, we evaluated the mechanical properties of the samples. It was observed that samples with porosity exceeding 12 % exhibited low surface hardness and strength, rendering them unsuitable for use. The wax powder weight (M, kg) required to produce a sample with the desired porosity P was estimated using the following equation:

$$M = h\rho_{\text{s}}\left(1 - \frac{P}{100}\right)\left(\frac{\pi d^2}{4}\right). \qquad (10)$$

In this case, $h = d = 0.0433$ m. We calculated the necessary weights of T1 and PS50/50 waxes to achieve the specified sample porosity using the following empirical relationships obtained from experimentation:

$$M_{T1} = -0,55P + 55,$$

$$M_{PS50/50} = -0,5959P + 59.59.$$

Once the height h was reached, the loading arm of the AG-X plus Shimadzu machine remained stationary for a duration of 60 minutes while the stresses were recorded. During this time, as the air within the sample was expelled and the density redistributed, the stresses experienced a reduction but were not always completely eliminated. Consequently, the dimensions of the sample underwent changes due to the elastic reaction of the compacted material, which can be quantified as follows:

$$O = \frac{(d_i - d)}{d_i} \cdot 100\ \%, \qquad (11)$$

where O represents the elastic deformation, %; d and d_i denote the inner diameter of the mold and the height of the i-th samples, respectively. These measurements were obtained using a DIN 863 Vogel digital recorder with an accuracy of 0.001 mm.

Furthermore, the AG-X plus Shimadzu determined the compressive strength of the compacted samples at a loading arm velocity of 0.1 mm/s. This evaluation took place after the samples were held at a controlled temperature of 20±2 °C for a period of 48 hours.

Discussion

Figure 3 displays the experimental findings, illustrating exponential relationships between the stress σ_0 within samples composed of compacted T1 and PS50/50 powder waxes with particle sizes 2.5 mm and 0.63 mm, respectively, and the porosity (as the controllable variable). The figure also demonstrates the reliability of the polynomial approximation $1R^2_{2.5}$; $2R^2_{0.63}$; $3R^2_{2.5}$ и $4R^2_{0.63}$ for these specific samples.

Figure 3 demonstrates that the stresses observed in samples with a particle size of 2.5 mm are higher compared to those with a particle size of 0.63 mm across all materials investigated. This relationship can be attributed to the higher bulk density exhibited by the 2.5 mm samples in comparison to the 0.63 mm samples. Additionally, the compaction stress is influenced by the plasticity of the powder, which, in turn, is influenced by the melting point [33; 34]. Given that the melting point of T1 is higher than that of PS50/50, the stress observed in T1 is greater than in PS50/50. It was observed that when the particle size of the T1 and PS50/50 materials increases four-fold within the range of 0 % ≤ P ≤ 2 %, the difference in stresses reaches 30 %. As P increases, the difference diminishes.

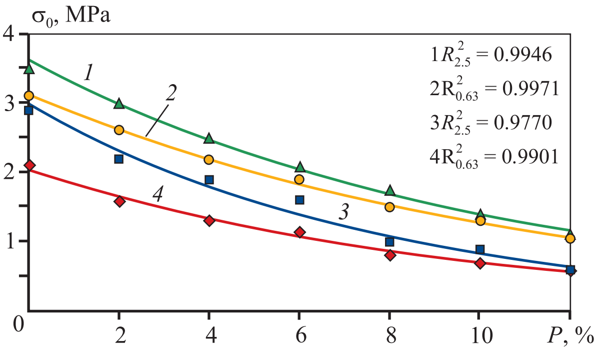

Fig. 3. Stress vs. porosity in the T1 and PS50/50 powder wax samples

1 – T1, 2.5 mm particle size; ***2*** – T1, 0.63 mm particle size;
3 – PS50/50, 2.5 mm particle size;
4 – PS50/50, 0.63 mm particle size

Рис. 3. Сравнение зависимостей напряжений от пористости прессовок из порошков воскообразных материалов Т1 и ПС50/50 различных фракций

1 – Т1, фракция 2,5 мм; ***2*** – Т1, фракция 0,63 мм;
3 – ПС50/50, фракция 2,5 мм; ***4*** – ПС50/50, фракция 0,63 мм

From a practical standpoint, it is valuable to compare the stresses observed in wax patterns with different particle sizes to the breaking stresses of the experimental samples exhibiting the same porosity. Figure 4 illustrates the relationship between the ultimate compressive strength (σ_{comp}) and porosity of the cylindrical samples. It is evident that the breaking stress increases with particle size. It can be concluded that while T1 samples exhibit greater resistance to compression compared to PS50/50 samples, the latter are sufficiently robust to endure the compressive loads applied by the initial (uncured) layer of the refractory shell.

To assess the compressive strength of compacted wax patterns, we introduced the stress safety margin N_{comp}. This margin represents the ratio of the ultimate compressive strength to the stress experienced during the compression of the powder wax. The stress safety margin can be calculated as follows:

$$N_{comp} = (\sigma_{comp} \cdot 100\ \%)/\sigma_0, \qquad (12)$$

where σ_{comp} represents the compressive strength, MPa; aand σ_0 is the compression stress measured by the test machine, MPa.

Figure 5 illustrates the stress safety margin (N_{comp}) as a function of sample porosity within the range of 0 % to 12 % for T1 and PS50/50 waxes, considering particle sizes of 0.63 mm and 2.5 mm.

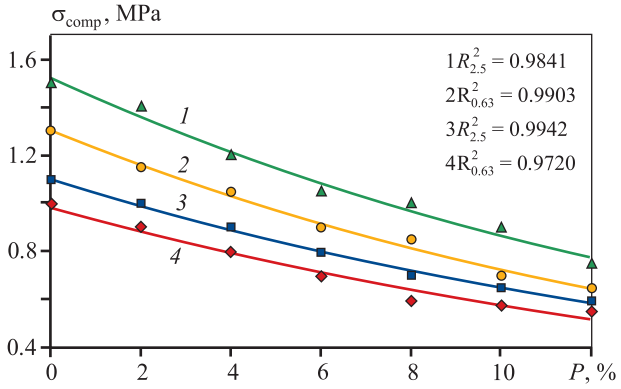

Fig. 4. Ultimate compressive strength vs. porosity in the T1 and PS50/50 powder wax samples

1 – T1, 2.5 mm particle size; ***2*** – T1, 0.63 mm particle size;
3 – PS50/50, 2.5 mm particle size;
4 – PS50/50, 0.63 mm particle size

Рис. 4. Сравнение зависимостей предела прочности на сжатие от пористости прессовок из порошков воскообразных материалов Т1 и ПС50/50 различных фракций

1 – Т1, фракция 2,5 мм; ***2*** – Т1, фракция 0,63 мм;
3 – ПС50/50, фракция 2,5 мм;
4 – ПС50/50, фракция 0,63 мм

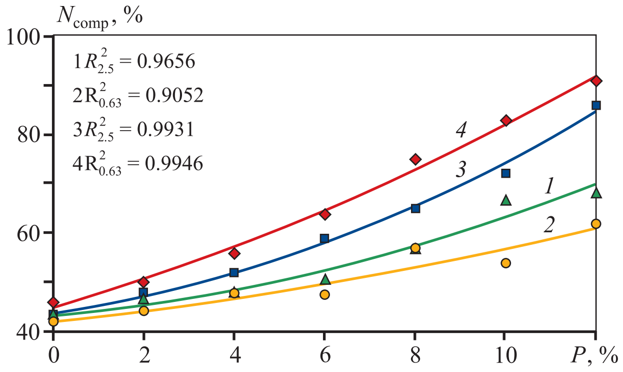

Fig. 5. Stress safety margin vs. porosity of T1 and PS50/50 powder wax samples

1 – T1, 2.5 mm particle size; ***2*** – T1, 0.63 mm particle size;
3 – PS50/50, 2.5 mm particle size;
4 – PS50/50, 0.63 mm particle size

Рис. 5. Сравнение зависимостей показателя пропорциональности напряжений от пористости прессовок из порошков воскообразных материалов Т1 и ПС50/50 различных фракций

1 – Т1, фракция 2,5 мм; ***2*** – Т1, фракция 0,63 мм;
3 – ПС50/50, фракция 2,5 мм;
4 – ПС50/50, фракция 0,63 мм

Using Fig. 5, we can predict the compressive strength of a wax pattern by using the stress safety margin value. For example, if we have a T1 wax sample with a particle size of 0.63 mm and a porosity of 8 %, the ultimate strength σ_{comp} is estimated to be 57 % of the σ_0 stress applied during wax compaction.

Additionally, when measuring the relaxation stresses σ_i in the samples following compression, we observed significant changes in σ_i values within a maximum of 25 minutes for all particle sizes. The time required for σ_i to decrease is longer for samples with a porosity of 2.5 mm compared to those with a particle size of 0.63 mm, particularly in cases of higher porosity. Overall, the relaxation period for PS50/50 wax samples is shorter compared to T1 wax samples. The table presents the experimentally determined values of k and τ for the Kohlrausch equation (obtained from equations (7) and (8)) for samples with 0 % and 12 % porosity. It is noteworthy that k and τ decrease as the porosity increases for all materials. By substituting the values of k and τ into the analytical expression (3), we can obtain the predicted relaxation curves.

Figure 6 displays the estimated and experimental relaxation periods for the T1 (Fig. 6, *a* and *b*) and PS50/50 (Fig. 6, *c* and *d*) samples, considering particle sizes of 2.5 mm and 0.63 mm, respectively.

Figure 6 illustrates that the experimental σ_i stress values, which occur as the compacted material is unloaded, decrease slightly faster than predicted by the exponential law. It was observed that significant changes (more than 90 % reduction) in the experimental σ_i values are achieved within the first 5 minutes and 10 minutes of holding under load for the samples with 12 % and 0 % porosity, respectively. This pattern holds true for all wax grades and particle sizes. Generally, the trends of the estimated and experimental σ_i values align closely with each other.

Conclusion

The study revealed several key findings regarding the compaction and behavior of wax patterns. Firstly, it was observed that the stresses measured during the compaction of larger 2.5 mm particle size powder samples were higher than those of the 0.63 mm particle size samples for all materials. This discrepancy can be attributed to the higher bulk density of the 2.5 mm particle size wax compared to the 0.63 mm particle size wax, as well as differences in the elastic properties and melting points.

Experimental k and τ values for the Kohlrausch equation

Расчетные параметры k и τ для уравнения Кольрауша, определенные по экспериментальным данным

Wax grade	Particle size, mm	Porosity,%	Analytical expression variables	
			k	τ
T1	2.5	0	0.729	3.034
	2.5	12	0.589	1.478
	0.63	0	0.568	2.058
	0.63	12	0.375	0.706
PS50/50	2.5	0	0.722	3.250
	2.5	12	0.401	1.023
	0.63	0	0.566	2.453
	0.63	12	0.313	0.742

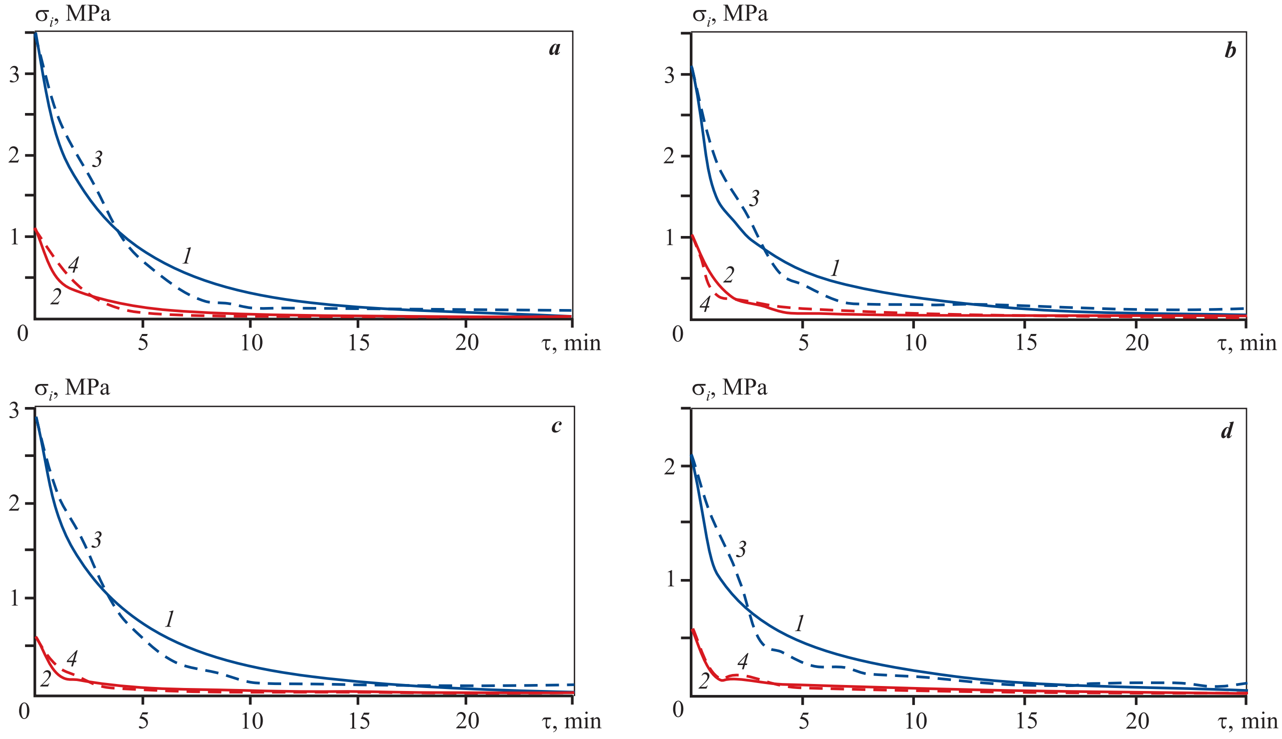

Fig. 6. Experimental and estimated stress vs. relaxation period curves for different wax grades and particle sizes

a – T1, 2.5 mm particle size; ***b*** – T1, 0.63 mm particle size; ***c*** – PS50/50, 2.5 mm particle size; ***d*** – PS50/50, 0.63 mm particle size
1, ***3*** – $P = 0$ %; 2, 4: $P = 12$ %
Solid curves – estimated, dashed curves – experimental

Рис. 6. Сравнение экспериментальных и расчетных экспоненциальных зависимостей напряжений от времени релаксации прессовок для различных материалов и фракций

a – Т1, фракция 2,5 мм; ***b*** – Т1, фракция 0,63 мм; ***c*** – ПС50/50, фракция 2,5 мм; ***d*** – ПС50/50, фракция 0,63 мм
1, ***3*** – $P = 0$ %; ***2***, ***4*** – $P = 12$ %
Сплошные кривые – расчет, штриховые – эксперимент

Additionally, the compressive breaking stress was found to be dependent on both sample porosity and particle size. The proposed stress safety margin provides a means to predict the compression strength of compacted wax patterns.

By utilizing the Kohlrausch equation, exponential relationships were established to describe the stress decrease over time. It was noted that the measured σ_i stresses occurring as the compacted wax is unloaded exhibited a slightly faster decrease than predicted by the exponential law. Significant changes in σ_i were mostly completed within the first 5 to 10 minutes of holding under load. A zero stress reading after relaxation indicated the absence of elastic deformation and confirmed the preservation of the required sample dimensions.

The research outcomes have practical implications for predicting the final dimensions of compacted powder wax patterns and enhancing the accuracy of investment casting. The proposed casting process involves the utilization of wax powder with particle sizes ranging from 0.63 mm to 2.5 mm, replacing the use of liquid or paste wax. The wax patterns are compressed and subsequently held under load. The resulting wax patterns exhibited improved quality, with no defects such as shrinkage, surface waviness, or buckling. The porosity of the samples was evenly distributed, reducing mold shell deformation during wax removal and enhancing the resistance to cracking, ultimately leading to improved casting quality.

References

1. Dogancan Okumus, Sefer A. Gunbeyaz, Rafet Emek Kurt, Osman Turan. Towards a circular maritime industry: Identifying strategy and technology solutions. *Journal of Cleaner Production*. 2023;382:134935. https://doi.org/10.1016/j.jclepro.2022.134935
2. Gogolukhina M., Mamedova L. Organisational and economic aspects of deep modernisation and foundation projects of shipbuilding yards. *Transportation Research Procedia*. 2022;63:2072—2078. https://doi.org/10.1016/j.trpro.2022.06.231
3. Chernyshov E.A., Romanov A.D., Romanova E.A. The quality control of high-resistance steel casting by optimizing the tempering temperature. *Materials Today: Proceedings*. 2021;38(4):1488—1490. https://doi.org/10.1016/j.matpr.2020.08.134
4. Abayomi A. Akinwande, Adeolu A. Adediran, Oluwatosin A. Balogun, Moses Ebiowei Yibowei, Abel A. Barnabas, Henry K. Talabi, Bayode J. Olorunfemi. Optimization of selected casting parameters on the mechanical behaviour of Al 6061/glass powder composites. *Heliyon*. 2022;8(5):e09350. https://doi.org/10.1016/j.heliyon.2022.e09350
5. Li Changyun, Wu Shiping, Guo Jingjie, Su Yanqing, Bi Weisheng, Fu Hengzhi. Model experiment of mold filling process in vertical centrifugal casting. *Journal of Materials Processing Technology*. 2006;176(1—3):268—272. https://doi.org/10.1016/j.jmatprotec.2006.04.004
6. Yiping Lu, Xuzhou Gao, Li Jiang, Zongning Chen, Tongmin Wang, Jinchuan Jie, Huijun Kang, Yubo Zhang, Sheng Guo, Haihui Ruan, Yonghao Zhao, Zhiqiang Cao, Tingju Li. Directly cast bulk eutectic and near-eutectic high entropy alloys with balanced strength and ductility in a wide temperature range. *Acta Materialia*. 2017;124:143—150. https://doi.org/10.1016/j.actamat.2016.11.016
7. Krushenko G.G. Improvement of quality of steel casted propeller for river passenger vessel. *Sudostroenie*. 2016;6(829):54—57. (In Russ). Крушенко Г.Г. Повышение качества стального литого гребного винта для пассажирского речного судна. *Судостроение*. 2016;6(829):54—57.
8. Markov S.P., Muktepavel V.O., Murzin V.V. Surface hardening of the bronze ship propeller. *Morskie intellektual'nye tekhnologii*. 2019;4-1(46):97—101. (In Russ.). Марков С.П., Муктепавел В.О., Мурзин В.В. Поверхностное упрочнение судовых гребных винтов из бронзы. *Морские интеллектуальные технологии*. 2019;4-1(46):97—101.
9. Abashkin E.E., Tkacheva A.V. Study of local combined heat impact on permanent joints. *Morskie intellektual'nye tekhnologii*. 2022;3-1(57):310—318. (In Russ.). https://doi.org/10.37220/MIT.2022.57.3.040 Абашкин Е.Е., Ткачева А.В. Влияние предварительного подогрева пластины на значения и распределение остаточных напряжений, образованных в результате наплавки. *Морские интеллектуальные технологии*. 2022;3-1(57):310—318. https://doi.org/10.37220/MIT.2022.57.3.040
10. Ayar M.S., Ayar V.S., George P.M. Simulation and experimental validation for defect reduction in geometry varied aluminium plates casted using sand casting. *Materials Today: Proceedings*. 2020;27:1422—1430. https://doi.org/10.1016/j.matpr.2020.02.788

11. Pan Tao, Heng Shao, Zhijun Ji, Hai Nan, Qingyan Xu. Numerical simulation for the investment casting process of a large-size titanium alloy thin-wall casing. *Progress in Natural Science: Materials International.* 2018;28(4): 520—528. https://doi.org/10.1016/j.pnsc.2018.06.005
12. Kapranos P., Carney C., Pola A., Jolly M. 5.03 — Advanced casting methodologies: Investment casting, centrifugal casting, squeeze casting, metal spinning, and batch casting. *Comprehensive Materials Processing.* 2014;5:39—67. https://doi.org/10.1016/B978-0-08-096532-1.00539-2
13. Garanin V.F., Ivanov V.N., Kazennov S.A., Kurchman B.S., Lishchenko N.N., Ozerov V.A., Roshan N.R., Sokol I.B., Telis M.Ya., Chulkova A.D., Shklennik Ya.I., Shklennik L.Ya. Investment casting. Ed. V.A. Ozerov. 4th ed. Moscow: Mashinostroenie, 1994. 448 p. (In Russ.).
    Гаранин В.Ф., Иванов В.Н., Казеннов С.А., Курчман Б.С., Лищенко Н.Н., Озеров В.А., Рошан Н.Р., Сокол И.Б., Телис М.Я., Чулкова А.Д., Шкленник Я.И., Шкленник Л.Я. Литье по выплавляемым моделям. Под общ. ред. В.А. Озерова. 4-е изд., перераб. и доп. М.: Машиностроение, 1994. 448 с.
14. Radtsevich Kh.M. Calculation of allowances and interoperational dimensions in mechanical engineering: textbook. allowance. Moscow: Vysshaya shkola, 2004. 272 p. (In Russ.).
    Радцевич Х.М. Расчет припусков и межоперационных размеров в машиностроении: Учеб. пос. М.: Высшая школа, 2004. 272 с.
15. Prokopchuk N.R., Gorshcharik N.D., Klyuev A.Yu., Kozlov N.G., Rozhkova E.I., Latyshevich I.A., Bakovich N.A. Model compositions for precision casting. *Vestsi Natsyyanal'nai akademii navuk Belarusi. Seryya khimichnykh navuk*. 2015;(4): 122—128. (In Russ.).
    Прокопчук Н.Р., Горщарик Н.Д., Клюев А.Ю., Козлов Н.Г., Рожкова Е.И., Латышевич И.А., Бакович Н.А. Модельные составы для точного литья. *Весцi Нацыянальнай акадэміі навук Беларусі. Серыя хімічных навук*. 2015;(4):122—128.
16. Sapchenko I.G., Zhilin S.G., Komarov O.N. Controlling the structure and properties of porous combined removable models. Vladivostok: Dal'nauka, 2007. 138 p. (In Russ.).
    Сапченко И.Г., Жилин С.Г., Комаров О.Н. Управление структурой и свойствами пористых комбинированных удаляемых моделей. Владивосток, Дальнаука, 2007. 138 с.
17. Foggia M.Di, D'Addona D.M. Identification of critical key parameters and their impact to zero-defect manufacturing in the investment casting process. *Procedia CIRP.* 2013;12:264—269. https://doi.org/10.1016/j.procir.2013.09.046
18. Ospennikova O.G. Thermophysical and rheological characteristics of synthetic resins for model compositions. *Liteinoe Proizvodstvo.* 2016;(10):26—28. (In Russ.).
    Оспенникова О.Г. Теплофизические и реологические характеристики синтетических смол для модельных композиций. *Литейное производство.* 2016;(10):26—28.
19. Tascioglu S., Akar N. Conversion of an investment casting sprue wax to a pattern wax by chemical agents. *Materials and Manufacturing Processes.* 2003; 18(5):753—768. https://doi.org/10.1081/AMP-120024973
20. Sapchenko I.G., Zhilin S.G., Potianikhin D.A., Komarov O.N. Mesomechanics of technological properties of powdered polymer compacts in Lost Wax Casting. *AIP Conference Proceedings.* 2014;1623:543—546. https://doi.org/10.1063/1.4899002
21. Vinokurov G.G., Popov O.N. Statistical modeling of local density macrostructure correlation at one-sided pressing of powder materials. *Izvestiya Samarskogo nauchnogo tsentra RAN.* 2011;13(1—3)(39):553—557. (In Russ.).
    Винокуров Г.Г., Попов О.Н. Статистическое моделирование корреляции локальной плотности макроструктуры при одностороннем прессовании порошковых материалов. *Известия Самарского научного центра РАН.* 2011;13(1—3)(39):553—557.
22. Zhilin S.G., Komarov O.N., Bogdanova N.A., Amosov O.S. Mathematical modelling of forming processes in the conditions of uniaxial compaction of powder wax-like materials. In: *CEUR Workshop Proceedings. "ITHPC 2021 — Short paper proceedings of the 6th International Conference on information technologies and high-performance computing".* 2021. P. 148—154.
23. Zhilin S.G., Bogdanova N.A., Komarov O.N., Sosnin A.A. Decrease in the elastic response in compacting a paraffin—stearin powder composition. *Russian Metallurgy (Metally).* 2021;(4):459—463. https://doi.org/10.1134/S0036029521040376
    Жилин С.Г., Богданова Н.А., Комаров О.Н., Соснин А.А. Снижение упругого отклика при уплотнении порошковой парафиностеариновой композиции. *Деформация и разрушение материалов.* 2020;(1):29—33. https://doi.org/10.31044/1814-4632-2020-1-29-33

24. Dong Y.W., Li X.L., Qi Zhao, Jun Yang, Ming Dao. Modeling of shrinkage during investment casting of thin-walled hollow turbine blades. *Journal of Materials Processing Technology*. 2017;244:190—203. https://doi.org/10.1016/j.jmatprotec.2017.01.005
25. Michio Ito, Toshio Yamagishi, Yoshiki Oshida, Carlos A. Munoz. Effect of selected physical properties of waxes on investments and casting shrinkage. *The Journal of Prosthetic Dentistry*. 1996;75(2):211—216. https://doi.org/10.1016/S0022-3913(96)90101-8
26. Malkin A.Ya., Isaev A.I. Rheology. Concepts, methods, applications. Moscow: Professiya, 2007. 560 p. (In Russ.).
    Малкин А.Я., Исаев А.И. Реология. Концепции, методы, приложения. М.: Профессия, 2007. 560 с.
27. Malkin A.Ya., Chalykh A.E. Diffusion and viscosity of polymers. Moscow: Khimiya, 1979. 304 p. (In Russ.).
    Малкин А.Я., Чалых А.Е. Диффузия и вязкость полимеров. М.: Химия, 1979. 304 с.
28. Galperin A.M., Shafarenko E.M., Rheological calculations of mining structures. Moscow: Nedra, 1977. 246 p. (In Russ.).
    Гальперин А.М., Шафаренко Е.М. Реологические расчеты горнотехнических сооружений. М.: Недра, 1977. 246 с.
29. Zhilin S.G., Komarov O.N., Potyanikhin D.A., Sosnin A.A. Experimental determining parameters of Kohlrausch regression dependence for porous compacts from waxy powder compositions. *Inzhenernyi zhurnal: Nauka i innovatsii*. 2018;2(74):9. (In Russ.). http://doi.org/10.18698/2308-6033-2018-2-1732
    Жилин С.Г., Комаров О.Н., Потянихин Д.А., Соснин А.А. Экспериментальное определение параметров регрессионной зависимости Кольрауша для пористых прессовок из воскообразных порошковых композиций. *Инженерный журнал: Наука и инновации*. 2018;2(74):9. http://doi.org/10.18698/2308-6033-2018-2-1732
30. Zhilin S.G., Bogdanova N.A., Komarov O.N. Influence of parameters of the compacting of powder body from wax-like material on the forming of residual stresses of pressing. *Vestnik Chuvashskogo gosudarstvennogo pedagogicheskogo universiteta im. I.Ya. Yakovleva. Seriya: Mekhanika predel'nogo sostoyaniya*. 2019;3(41):110—121. (In Russ.). http://doi.org/10.26293/chgpu.2019.41.3.009
    Жилин С.Г., Богданова Н.А., Комаров О.Н. Влияние параметров уплотнения порошкового тела из воскообразного материала на формирование остаточных напряжений прессовки. *Вестник Чувашского государственного педагогического университета им. И.Я. Яковлева. Серия: Механика предельного состояния*. 2019;3(41):110—121. http://doi.org/10.26293/chgpu.2019.41.3.009
31. Pavlov V.I., Askadskii A.A., Slonimskii G.L. Graph-analytical method for calculating the mechanical characteristics of a material by stress relaxation at constant deformation. *Mekhanika polimerov*. 1965;(6):16—19. (In Russ.).
    Павлов В.И., Аскадский А.А., Слонимский Г.Л. Графоаналитический способ расчета механических характеристик материала по реакции напряжения при постоянной деформации. *Механика полимеров*. 1965;(6):16—19.
32. Pribytkov G.A., Korzhova V.V., Korosteleva E.N. Strength properties and features of destruction of composites of Al—Cr and Al—Cr—Si systems obtained by hot compaction of powder mixtures. *Deformatsiya i razrushenie materialov*. 2013;(8):13—20. (In Russ.).
    Прибытков Г.А., Коржова В.В., Коростелева Е.Н. Прочностные свойства и особенности разрушения композитов систем Al—Cr и Al—Cr—Si, полученных горячим уплотнением порошковых смесей. *Деформация и разрушение материалов*. 2013;(8):13—20.
33. Nicole K. Aragon, Sheng Yin, Hojun Lim, Ill Ryu. Temperature dependent plasticity in BCC micropillars. *Materialia*. 2021;19:101181. https://doi.org/10.1016/j.mtla.2021.101181
34. Remo N. Widmer, Alexander Groetsch, Guillaume Kermouche, Ana Diaz, Gilles Pillonel, Manish Jain, Rajaprakash Ramachandramoorthy, Laszlo Pethö, Jakob Schwiedrzik, Johann Michler. Temperature-dependent dynamic plasticity of micro-scale fused silica. *Materials & Design*. 2022;215:110503. https://doi.org/10.1016/j.matdes.2022.110503

Information about the authors

Sergey G. Zhilin — Cand. Sci. (Eng.), Associate Prof., Leading Researcher, Laboratory for the Problems of Creation and Processing of Materials and Products, Institute of Machinery and Metallurgy of Far-Eastern Branch of the Russian Academy of Sciences.
https://orcid.org/0000-0002-0865-7109
E-mail: sergeyzhilin1@rambler.ru

Nina A. Bogdanova — Junior Researcher, Laboratory of Problems of Creation and Processing of Materials and Products, Institute of Machinery and Metallurgy of Far Eastern Branch of the Russian Academy of Sciences.
https://orcid.org/0000-0002-8769-8194
E-mail: joyful289@inbox.ru

Oleg N. Komarov — Cand. Sci. (Eng.), Associate Prof., Director of Institute of Machinery and Metallurgy of Far-Eastern Branch of the Russian Academy of Sciences.
https://orcid.org/0000-0002-7121-4271
E-mail: olegnikolaevitsch@rambler.ru

Информация об авторах

Сергей Геннадьевич Жилин — к.т.н., доцент, вед. науч. сотрудник лаборатории проблем создания и обработки материалов и изделий Института машиноведения и металлургии (ИМиМ) ДВО РАН.
https://orcid.org/0000-0002-0865-7109
E-mail: sergeyzhilin1@rambler.ru

Нина Анатольевна Богданова — мл. науч. сотрудник лаборатории проблем создания и обработки материалов и изделий ИМиМ ДВО РАН.
https://orcid.org/0000-0002-8769-8194
E-mail: joyful289@inbox.ru

Олег Николаевич Комаров — к.т.н., доцент, директор ИМиМ ДВО РАН.
https://orcid.org/0000-0002-7121-4271
E-mail: olegnikolaevitsch@rambler.ru

Contribution of the authors

Sergey G. Zhilin — determination of the purpose of the work, participation in the processing of experimental data and discussion of the results, writing the article.

Nina A. Bogdanova — conducting experiments, participation in the processing of experimental data and discussion of the results.

Oleg N. Komarov — participation in the processing of experimental data and discussion of the results.

Вклад авторов

С.Г. Жилин — определение цели работы, участие в обработке экспериментальных данных и обсуждении результатов, написание статьи.

Н.А. Богданова — проведение экспериментов, участие в обработке экспериментальных данных и обсуждении результатов.

О.Н. Комаров — участие в обработке экспериментальных данных и обсуждении результатов.

The article was submitted 23.03.2023, revised 06.04.2023, accepted for publication 10.04.2023

Статья поступила в редакцию 23.03.2023, доработана 06.04.2023, подписана в печать 10.04.2023

PRESSURE TREATMENT OF METALS / ОБРАБОТКА МЕТАЛЛОВ ДАВЛЕНИЕМ

UDC 621.777
https://doi.org/10.17073/0021-3438-2023-3-67-78

Research article
Научная статья

Using simulation to design tool for pressing of hollow profiles from aluminum alloys

S.B. Sidelnikov, S.S. Koloskov, N.N. Dovzhenko, Yu.A. Gorbunov, D.S. Voroshilov

Siberian Federal University
95 Krasnoyarskiy Rabochiy prosp., Krasnoyarsk, 660025, Russia

✉ Denis S. Voroshilov (sibdrug@mail.ru)

Abstract: In order to simulate the pressing of hollow profiles made from aluminum alloys, the previously developed design algorithms for the pressing tool and the QForm software were utilized. The objective of this study was to enhance the quality and decrease the design time intervals for pressing tools used in the industrial production of aluminum alloy profiles. A novel design procedure for a combined tool, along with the technology of semi-continuous pressing with welded hollow profiles made from aluminum alloys, was proposed. This was achieved using the QForm software, which enables efficient calculations and adjustments of pressing parameters and tool geometry through a dialog interface. The developed algorithm and design procedures enable the drawing of hollow profiles, technological calculations of pressing parameters, selection of a suitable horizontal hydraulic press, matrix and splitter design, determination of strength parameters, assessment of equipment load, and preparation of working drawings for the pressing tool. In order to validate the effectiveness of the design procedure, it was applied to typical hollow profiles fabricated on a commercial scale. Two variations of the pressing tool design were examined. Simulation results obtained from QForm Extrusion software, specifically designed for pressing analysis, revealed that the initial design of the tool, with predetermined technological parameters and geometry of the splitter and matrix channels, resulted in uneven flow of profile elements and temperature distribution. However, by adjusting the tool parameters, it was possible to achieve a straight profile exit from the matrix and a uniform temperature distribution across its cross section. Industrial verification of the designed tool, utilizing a 33 MN hydraulic horizontal press for pressing profiles made from alloy 6063, demonstrated that significant modifications to the matrix and splitter were not necessary. By employing the proposed pressing tool design, batches of products were successfully manufactured in compliance with the required technical specifications, while reducing the design time intervals of the pressing tool by approximately 50 %.

Keywords: aluminum alloys, hollow profiles, pressing, horizontal hydraulic press, combined tool, technological calculations, design methods and procedures.

Acknowledgement: We acknowledge the support provided by the Governmental contract of Siberian Federal University, Project FSRZ-2020-0013.

For citation: Sidelnikov S.B., Koloskov S.S., Dovzhenko N.N., Gorbunov Yu.A., Voroshilov D.S. Using simulation to design tool for pressing of hollow profiles from aluminum alloys. *Izvestiya. Non-Ferrous Metallurgy*. 2023;29(3):67–78.
https://doi.org/10.17073/0021-3438-2023-3-67-78

Применение моделирования при проектировании инструмента для прессования полых профилей из алюминиевых сплавов

С.Б. Сидельников, С.С. Колосков, Н.Н. Довженко, Ю.А. Горбунов, Д.С. Ворошилов

Сибирский федеральный университет
660025, Россия, г. Красноярск, пр. Красноярский рабочий, 95

✉ Денис Сергеевич Ворошилов (sibdrug@mail.ru)

Аннотация: Для моделирования процесса прессования полых профилей из алюминиевых сплавов использованы разработанные ранее алгоритмы проектирования прессового инструмента и программный комплекс «QForm». Целью проведенных исследований являлось повышение качества и снижение сроков проектирования прессового инструмента для промышленных условий производства профилей из алюминиевых сплавов. Предложены новая методика проектирования комбинированного инструмента и технологии для полунепрерывного прессования со сваркой полых профилей из алюминиевых сплавов с помощью программного комплекса «QForm», который позволяет в диалоговом режиме оперативно проводить многовариантные расчеты с последующей, если необходимо, корректировкой технологических параметров прессования и геометрии инструмента. Созданы алгоритм и процедуры проектирования, которые дают возможность выполнить чертеж полого профиля, осуществить технологические расчеты параметров прессования и выбор горизонтального гидравлического пресса, спроектировать матрицу и рассекатель, провести прочностные расчеты, определить силовую загрузку оборудования и подготовить рабочие чертежи прессового инструмента. Для проверки работоспособности разработанной методики проектирования приведен пример ее реализации для одного из типовых полых профилей, изготавливаемого в промышленном производстве. Рассмотрено проектирование двух вариантов прессового инструмента. С помощью моделирования с использованием программы «QForm Extrusion», предназначенной для анализа процессов прессования, установлено, что первый вариант конструкции инструмента при заданных технологических параметрах и геометрии каналов рассекателя и матрицы приводит к неравномерности истечения различных элементов профиля и температур. В результате проведенной корректировки параметров инструмента удалось добиться прямолинейности выхода профиля из матрицы и равномерности распределения температур по его сечению. Промышленное опробование спроектированного инструмента на гидравлическом горизонтальном прессе с усилием 33 МН для прессования профиля из сплава 6063 показало, что существенной доработки матрицы и рассекателя не требуется. С применением предложенной конструкции прессового инструмента получены партии продукции, соответствующей требованиям действующих технических условий, при этом сроки проектирования прессового инструмента сокращены практически в 2 раза.

Ключевые слова: алюминиевые сплавы, полые профили, прессование, горизонтальный гидравлический пресс, комбинированный инструмент, технологические расчеты, методика и процедуры проектирования.

Благодарности: Работа выполнена в рамках государственного задания на науку ФГАОУ ВО «Сибирский федеральный университет», номер проекта FSRZ-2020-0013.

Для цитирования: Сидельников С.Б., Колосков С.С., Довженко Н.Н., Горбунов Ю.А., Ворошилов Д.С. Применение моделирования при проектировании инструмента для прессования полых профилей из алюминиевых сплавов. *Известия вузов. Цветная металлургия*. 2023;29(3):67–78. https://doi.org/10.17073/0021-3438-2023-3-67-78

Introduction

Currently, the primary approach for manufacturing hollow aluminum profiles involves the utilization of a semi-continuous pressing method with a combined tool [1—7]. This method entails pressing profiles with a welding process at the center of deformation, using a combined tool consisting of a matrix and a splitter. The matrix shapes the outer contour of the profile, while the splitter forms its inner contour. During the pressing operation, a workpiece is inserted into a container and divided into multiple metal flows by the splitter. These metal flows are then directed into the welding chamber, where they are fused together under high temperatures and pressure to form a hollow profile with the desired cross-section.

Ensuring uniform outflow velocities of different profile elements from the matrix is crucial for producing high-quality pressed items during the pressing process. Significant variations in element velocities can lead to various defects such as twisting, waves, deflections, and barrels. These defects may persist even after subsequent corrective measures such as tensioning. Thus, achieving the correct positioning of the profile on the matrix mirror and implementing effective working braking bands on different segments of the tool are important considerations in pressing tool design. In addition to improving the quality of aluminum alloy profiles, it is necessary to enhance production efficiency.

To increase efficiency, reducing order fulfillment time by minimizing idle time and optimizing operations at all stages of production is a promising approach. Rapid adjustment and quick initiation of repeated precoders are key factors in achieving this goal.

Extensive research has been conducted on pressing techniques, as evidenced by numerous studies [8—20]. However, to date, there is a lack of an established procedure and software specifically designed for the design of tools and the technology of semi-continuous pressing for hollow profiles made from aluminum alloys using a combined tool.

Scientific and technical publications indicate that the most suitable software for practical application in this area is INPRESS CAD [21]. This software consists of four subsystems, each equipped with calculation and design procedures that facilitate the preparation of documentation for the implementation of specific technological processes. One of these subsystems focuses on the design of solid profiles from aluminum alloys. It enables the calculation of calibrating bands, the creation of drawings for matrices, prechambers, substrates, and other types of pressing tools, as well as the determination of force conditions and the selection of equipment for semi-continuous pressing of aluminum alloys. Additionally, there exists a subsystem dedicated to the design of pressing tools and the fabrication technology of hollow profiles. However, despite its potential, the use of this software is limited due to the complexity of the procedures involved in designing matrices and splitters. These procedures cannot be easily formalized or automated. As a result, combined tools are currently designed using an interactive approach, relying on the expertise and experience of professionals in the field, such as designers and technologists [22—25].

Furthermore, the simulation of pressing processes is currently carried out using the QForm Extrusion software [26] developed by Kvantorform company, Moscow, Russia. This software is based on the finite element method and offers several advantages. It enables the simulation of metal flow during pressing operation and provides an estimation of profile quality [27; 28]. Moreover, it takes into account for the influence of tool deformation on the pattern of profile outflow. One of the notable benefits of QForm Extrusion is its ability to rapidly calculate these processes, surpassing other comparable software such as DEFORM 3D. This allows the quick execution several of multiple calculations and significantly reduces the time required for tool design and implementation.

The objective of the conducted studies was to enhance the quality of aluminum alloy profiles and reduce the design intervals for pressing tools in industrial manufacturing conditions using QForm software.

Experimental

In general, the design procedure and calculation of pressing technology for hollow profiles follows a similar process to that of solid profiles [21]. The procedure can be broken down into the following steps:

1) formation of the profile's normal drawing:
   - — creation of a normal drawing of the profile;
   - — perform typical calculations such as perimeter, surface area, circumcircle diameter, etc;
   - — coordinate the drawing with the customer;

2) technological calculations and selection of main pressing parameters:
   - — determine the extrusion process settings;
   - — conduct preliminary calculation for pressing force and select the appropriate hydraulic press and number of channels;
   - — calculate the workpiece length;

3) design of matrix set:
   - — determine the allowances for profile sizes;
   - — position the profile on the matrix mirror;

4) design of the splitter (boxes, tab, input region on the splitter, and other relevant components);

5) design of the matrix (welding chamber, prechamber, presetting of fillet and angle of output zone, and other necessary elements);

6) verification of strength calculations and assessment of console elements of the tool;

7) adjustment of calibrating bands on the matrix and the splitter;

8) design of the substrate, special substrate, and any other required components;

9) preparation of the working drawing for the pressing tool;

10) calculation of the pressing force and selection of an appropriate press.

By applying this design procedure, significant reductions in production preparation time and metal consumption for tool adjustment can be achieved (see Fig. 1). Ultimately, this leads to a reduction in the overall production costs of the final products.

Results and discussion

Let us illustrate the application of the proposed design procedure through a practical example involving a standard profile made from aluminum alloy 6063, as depicted in Fig. 2. The profile comprises two distinct planes: square *1* (representing the first part) and rectangle *2* (representing the second part). The wall thickness remains consistent at 1.25 mm along the entire perimeter, while the surface area of the transverse cross-section measures 450 mm^2.

Upon completion of the normal drawing, a 33 MN hydraulic press was chosen for the pressing operation, with an extrusion coefficient of 106. The initial geometrical parameters and technological conditions for simulating the pressing process were then set as follows:

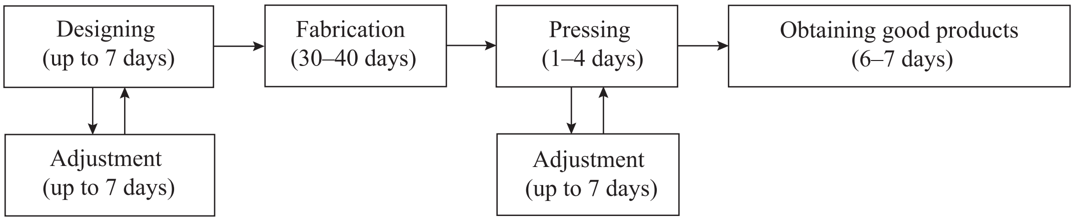

Fig. 1. Sequence of design procedures of the tool using QForm Extrusion simulation software

Рис. 1. Схема последовательности процедур проектирования инструмента
с применением программы компьютерного моделирования «QForm Extrusion»

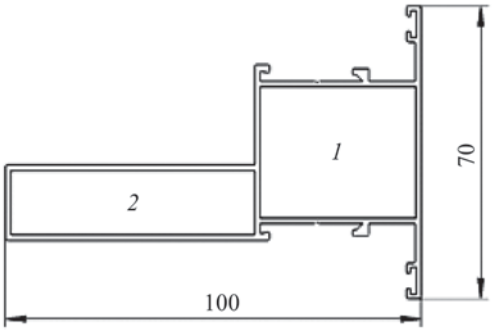

Fig. 2. General view of profile from alloy 6063

Рис. 2. Общий вид профиля из сплава 6063

a container diameter of 247 mm, a workpiece (ingot) diameter of 242 mm, a length of 1000 mm for the workpiece, a workpiece temperature of 450 °C, a matrix set temperature of 480 °C, a container temperature of 430 °C, and a pressing velocity of 2 mm/s.

The boundary conditions for calculating friction stresses at the contact between the metal and the tool were determined using the Levanov equation [26; 27]. The rheological and thermal technical properties of alloy 6063 were obtained from the library within the QForm Extrusion software.

The pressing tool material used was Grade 4Kh5MFS steel, chosen for its superior heat resistance in compliance with the specifications for hot pressing. The material hardness was measured at $HRC = 55 \div 58$.

Figure 3 presents the 3D models of the tool for the selected profile. The first model (Fig. 3, *a*), represents the initial configuration used for simulation, while the second model (Fig. 3, *b*) shows the adjusted configuration based on the results obtained from the simulation.

The diameter of the sets used in the pressing process was 340 mm. Each splitter was equipped with 6 boxes, which effectively divided the continuous workpiece into 6 metal flows. These individual flows were subsequently combined within the welding chamber, resulting in the formation of 7 joints along the entire profile length. In the second design iteration, specific adjustments were made to ensure an equal amount of metal flowed through each box per unit of time. This was achieved by increasing the total surface area of the splitter boxes at the input to 11416 mm^2. Furthermore, the extrusion at the input of the splitter was reduced to 4.2 units. As a consequence, these modifications improved the overall strength of the tool and led to a decrease in the required pressing force.

Following the development of the 3D model using QExDD software, a grid was generated for the calculation region and the tool using QShape software, as depicted in Fig. 4. The models were represented by triangles, with the initial design consisting of approximately 825 000 elements, and the second design consisting of around 900 000 elements. Once the grid was generated, the models were imported into QForm Extrusion software. Within the QForm Extrusion software, the main process parameters, rheological and thermal technical properties of alloy 6063, and boundary friction conditions were defined. Subsequently, the necessary calculations were performed using these predefined parameters and conditions.

Figure 5 presents the velocity distribution at different elements of the profile obtained using QForm Extrusion software with the first design of the tool. It is observed that the velocity of the square part of the profile (part 1) is measured at 220 mm/s, and there is no deviation from straightness. However, the velocity of the rectangular segment of the profile (part 2) is actually approximately half of that, resulting in the occurrence of defects.

During the analysis of the metal temperature across the profile elements (Fig. 6), it was determined that when utilizing the initial design of the pressing tool, the temperature distribution is non-uniform and ranges from 520 to 570 °C. Such variation in temperature can result in thermal deformation of the profile, as well as potential overheating and the formation of thermal cracks in specific segments of the profile, particularly at higher temperatures.

The calculations of the stress-strain state revealed that the elastic deformation of the pressing tool reaches 1 mm along the pressing axis, with deflection of the working bands reaching up to ±0.5 degrees. These factors can contribute to the accelerated deterioration of the matrix component, including wear of the working bands and the potential development of cracks. Attempts to enhance the initial design of the tool such as adjusting the

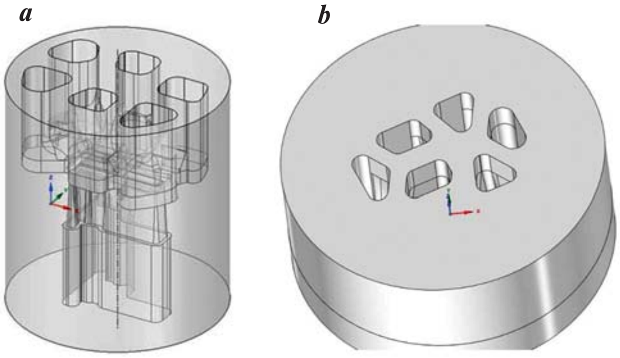

Fig. 3. 3D models of pressing tool
a – the initial variant; ***b*** – the second variant

Рис. 3. 3D-модели прессового инструмента
a – первый вариант; ***b*** – второй вариант

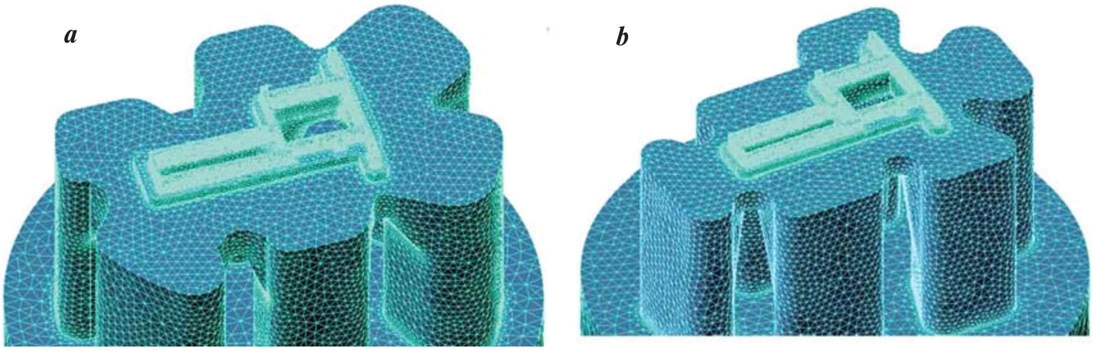

Fig. 4. Subdivision of calculated region into finite elements
a – for the initial design of the tool; ***b*** – for the second design of the tool

Рис. 4. Разбиение расчетной области на конечные элементы
а – для первого варианта конструкции инструмента; ***б*** – для второго варианта

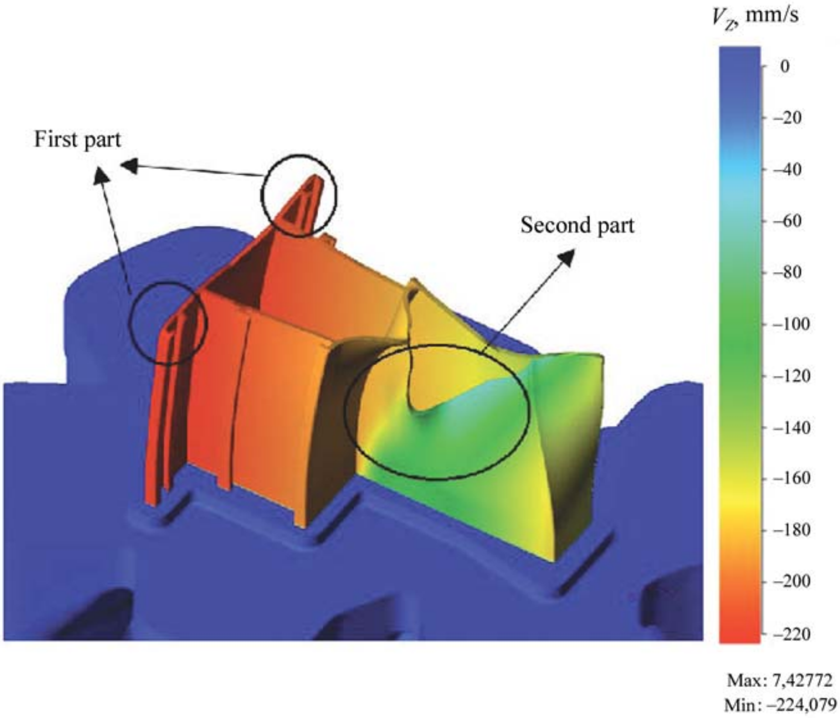

Fig. 5. Velocity distribution over the profile cross section for the initial tool design

Рис. 5. Распределение скоростей по сечению профиля для первого варианта конструкции инструмента

height of the working band or creating additional metal inflows, were unsuccessful in addressing these issues. Consequently, the decision was made to utilize the second design variant of the tool for further simulations, as depicted in Fig. 3, *b*.

The radius of the circumcircle across input boxes of the splitter remained at 210 mm, while the container diameter was set at 247 mm. As a result, defects and variations in chemical composition [29; 30] observed in the peripheral layers of the ingot were positioned outside the profile and remained in the inactive areas of the container (Fig. 7). The height of the splitter tab was reduced to 16.5 mm, thereby increasing the design rigidity and decreasing the torque due to a shorter lever arm. The difference in thickness between the working bands of the matrix and the splitter was 0.5 mm. The welding chamber and prechamber were designed using the same algorithm as in the initial tool design, with a height of 12 mm for the welding chamber and 5 mm for the prechamber. As the redesigned welding chamber had a

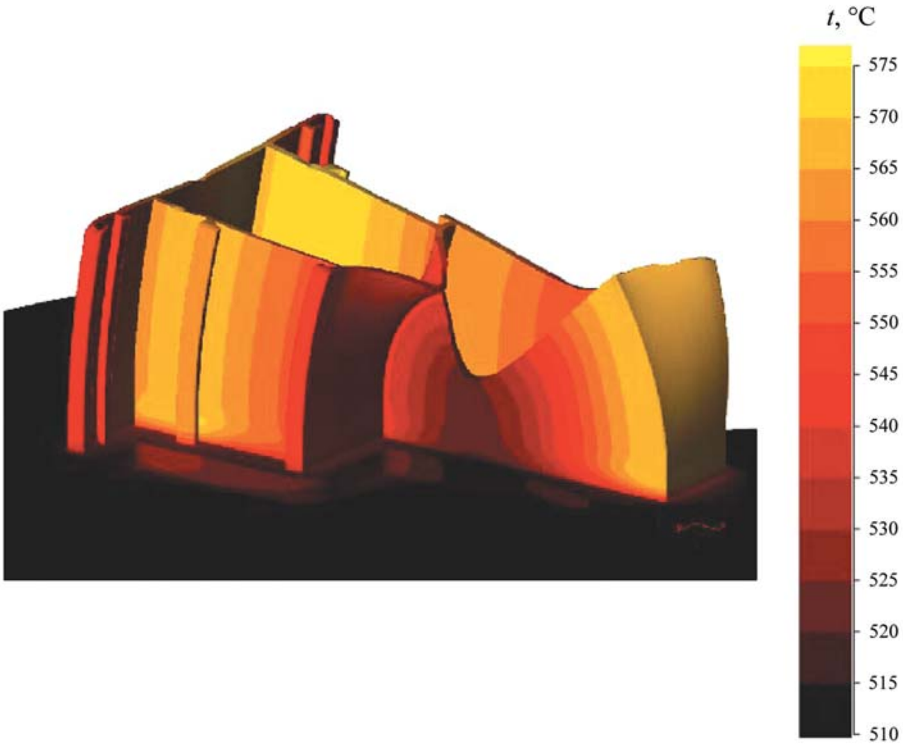

Fig. 6. Temperature distribution over profile elements for the initial variant of the tool design

Рис. 6. Распределение температур по элементам профиля для первого варианта конструкции инструмента

smaller surface area, it was expected that the changes in the shape of the splitter boxes would increase the strength of the tool. The fillet and output section of the matrix remained unchanged from the initial design. The working bands of the matrix and splitter (Fig. 8) were adjusted, taking into account the new design of the splitter boxes and the actual geometry of the profile obtained from the initial tool design.

Figures 9, 10 present the simulation results of the pressing process using the second variant of the pressing tool design, with the same technological parameters as before.

The analysis of the simulation results demonstrates that the new tool design greatly improves the homogeneity of profile outflow. However, it is observed that the metal velocity in the first part of the profile is slightly higher than the average velocity of the profile (Fig. 9). To address this, the surface area of the square box was reduced by 10 % and the height of the working band was adjusted in the subsequent simulation. The simulation results using the latest tool design (see Fig. 10) show a homogeneous velocity distribution across the entire profile cross section, with a velocity of 212 mm/s. This efficiency is further confirmed by the temperature distribution (see Fig. 11), where the temperature fluc-

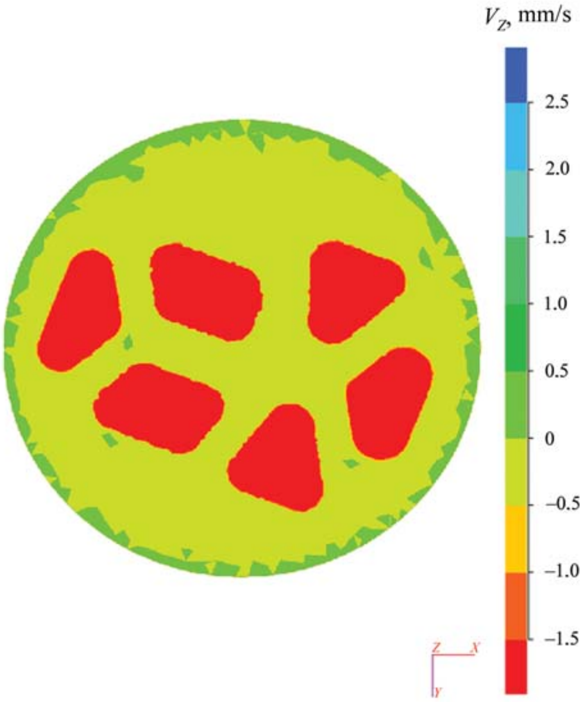

Fig. 7. Schematic view of formation of dead zones in container in front of input to splitter boxes

Рис. 7. Схема формирования мертвых зон в контейнере перед входом в карманы рассекателя

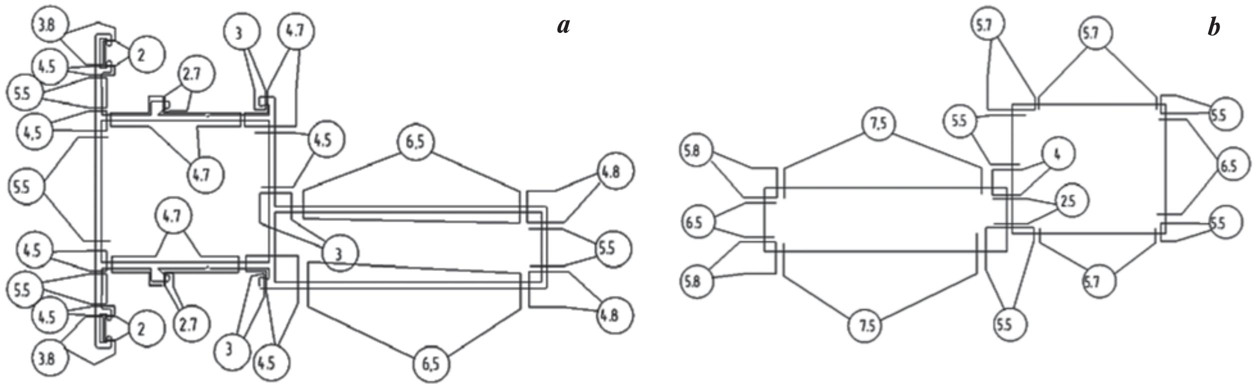

Fig. 8. Working bands of matrix (***a***) and splitter (***b***)

Рис. 8. Рабочие пояски матрицы (***a***) и рассекателя (***b***)

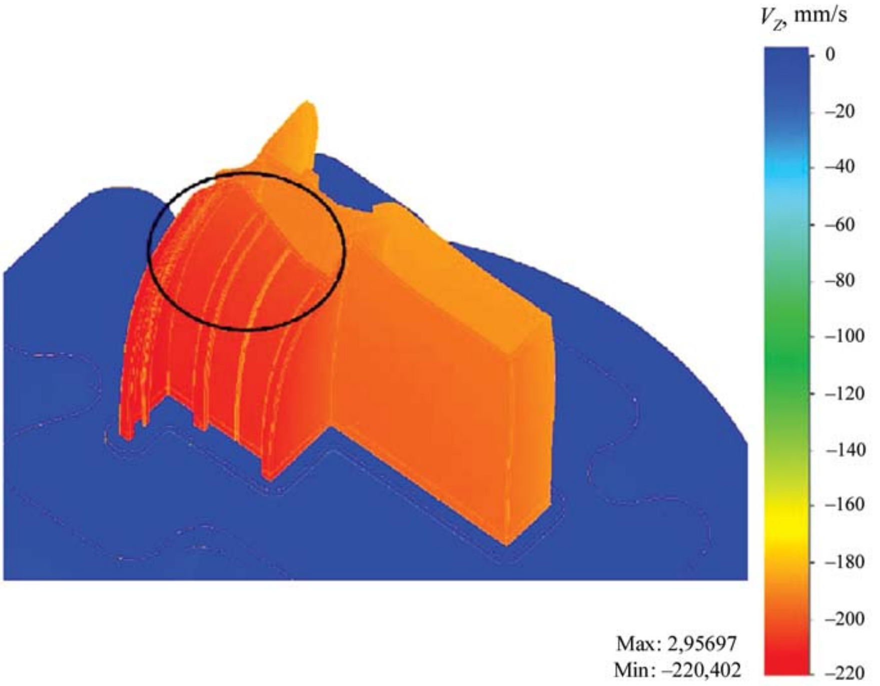

Fig. 9. Velocity distribution over the profile cross section for the second variant of the tool design

Рис. 9. Распределение скоростей по сечению профиля для второго варианта конструкции инструмента

tuation does not exceed 10 °C and the average profile temperature is 550 °C, in line with the technological specifications for semicontinuous pressing of hollow profiles from alloy 6063. In order to validate the simulation results in an industrial setting, pilot pressing of hollow profiles with the specified dimensions and alloy 6063 was conducted using a 33 MN horizontal hydraulic press at a Russian metallurgical plant. It was found that the design intervals of the combined pressing tool were effectively reduced by half, and the proposed tool design successfully produced profiles of the desired quality.

The calculated results of elastic deformation and stress intensity, obtained using QForm Extrusion software, are presented in Fig. 12. is evident that the tool undergoes significant elastic deformation during pressing, with a deflection of 1 mm along the pressing axis. Consequently, due to high stress intensity, there is a possibility of defects such as cracks.

Based on the simulation data, a decision was made to redesign the chamber at the splitter input and increase the rounding radii of the splitter. This modification led to a reduction in the loads on the tool and the required pressing force.

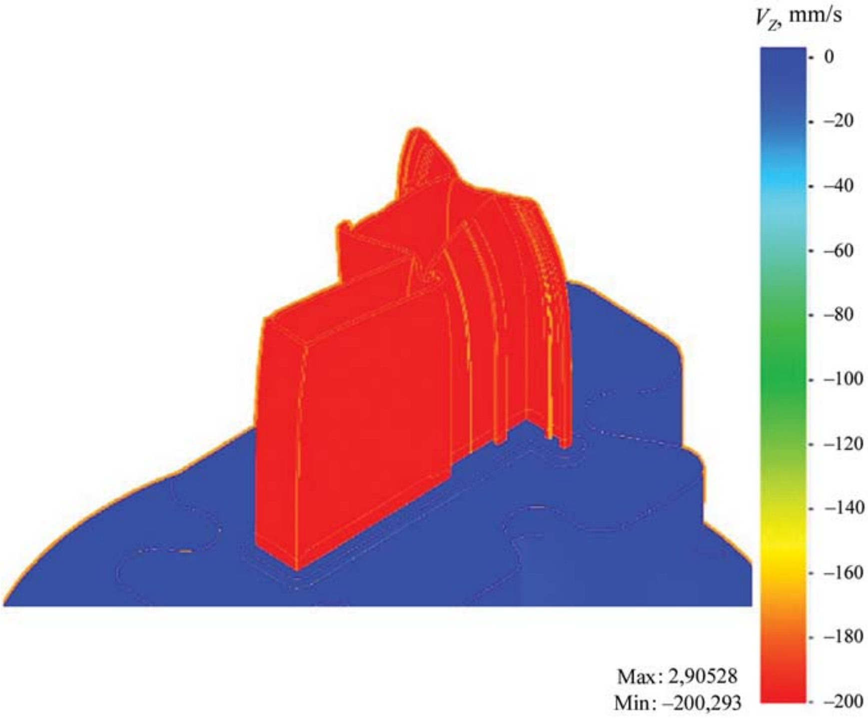

Fig. 10. Velocity distribution over the profile cross section for the second variant of the tool design after its modification

Рис. 10. Распределение скоростей по сечению профиля для второго варианта конструкции инструмента после ее доработки

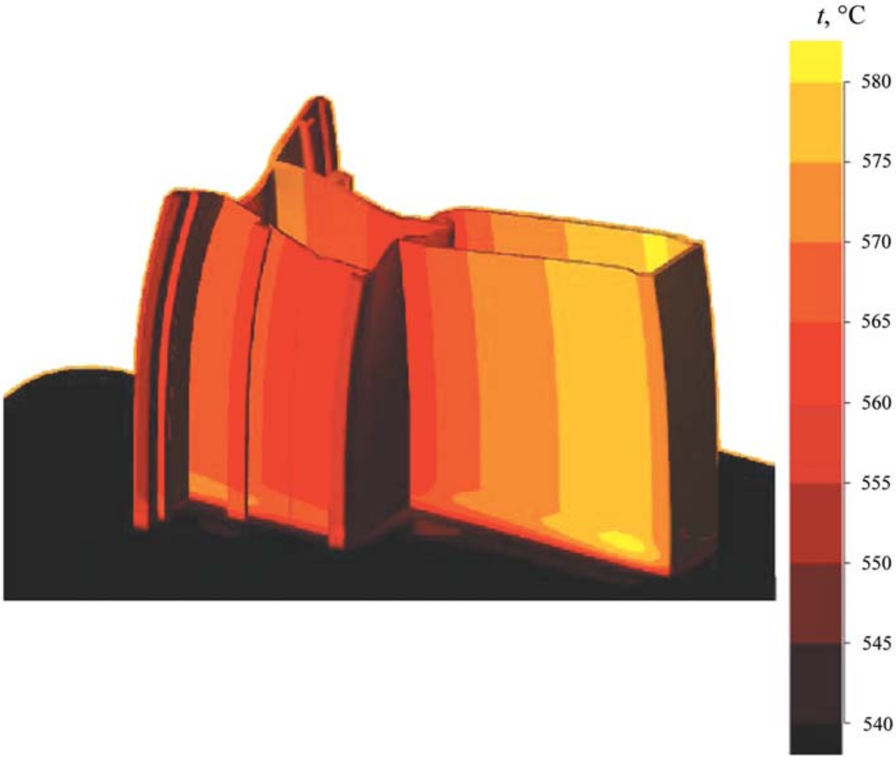

Fig. 11. Temperature distribution over the profile elements for the second variant of the tool design

Рис. 11. Распределение температуры по элементам профиля для второго варианта конструкции инструмента

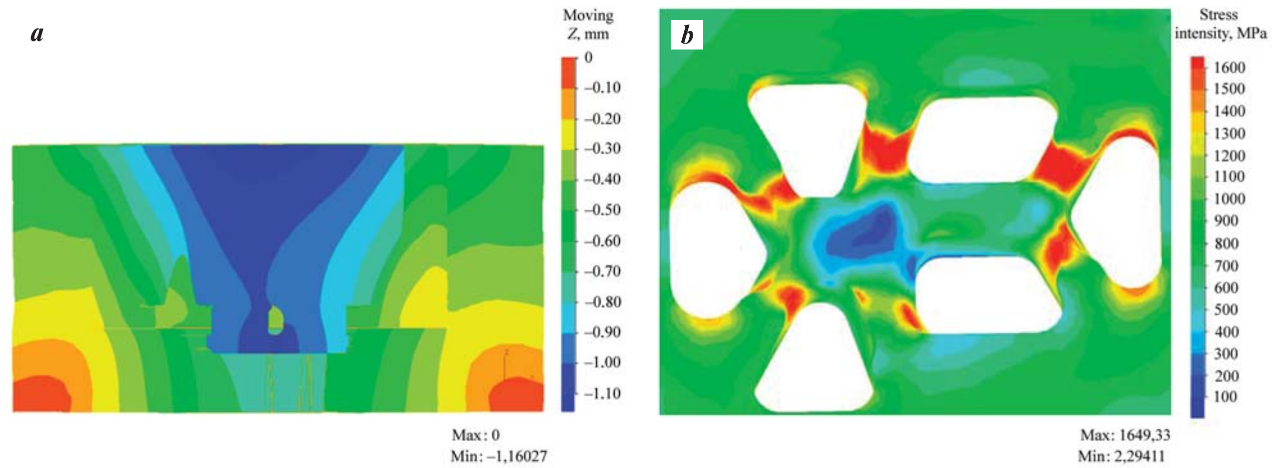

Fig. 12. Tool deformation (***a***) and stress intensity (***b***)

Рис. 12. Деформация инструмента (***a***) и интенсивность напряжений (***b***)

Conclusions

The proposed design procedure, combined with the utilization of QForm Extrusion software, successfully simulated the pressing of hollow profiles from aluminum alloys. This approach eliminated the need for repeated adjustments of newly fabricated matrix sets through trial pressing, thereby reducing the time required for the production of new profile ranges. In order to validate the simulation results in an industrial setting (Russian metallurgical plant), pilot pressing of hollow profiles made from alloy 6063 was conducted using a 33 MN horizontal hydraulic press (see Fig. 2). The results confirmed that no major modifications to the matrix and splitter were necessary, and the proposed design of the pressing tool enabled the production of industrial-grade products that met the requirements specified in the technical specifications.

References

1. Sakha P.K. Aluminum pressing technology. Moscow: NP APRAL, 2015. 352 p. (In Russ.).
   Саха П.К. Технология прессования алюминия. М.: НП АПРАЛ, 2015. 352 с.
2. Bowser M., Sauer K., Siegert G. Pressing: Reference guide. Translation from German under license from the publishing house «Aluminum Verlag Marketing & Kommunikation GmbH». Moscow: Alusil MV i T, 2009. 922 p. (In Russ.).
   Баузер М., Зауер К., Зигерт Г. Прессование: Справ. руководство. Пер. с нем. по лицензии издательства «Aluminium Verlag Marketing & Kommunikation GmbH». М.: Алюсил МВ и Т, 2009. 922 с.
3. Loginov Yu.N., Inatovich Yu.V. Tool for pressing metals: A tutorial. 2nd ed. Ekaterinburg: Izdatel'stvo Ural'skogo Universiteta, 2014. 224 p. (In Russ.).
   Логинов Ю.Н., Инатович Ю.В. Инструмент для прессования металлов: Учеб. пособие. 2-е изд., испр. и доп. Екатеринбург: Изд-во Уральского ун-та, 2014. 224 с.
4. Shcherba V.N. Pressing of aluminum alloys. Moscow: Intermet Engineering, 2001. 768 p. (In Russ.).
   Щерба В.Н. Прессование алюминиевых сплавов. М.: Интермет Инжиниринг, 2001. 768 с.
5. Qiang Li, Chris Harris, Mark R. Jolly. Finite element modelling simulation of transverse welding phenomenon in aluminium extrusion process. *Materials & Design*. 2003;24(7):493—496.
   https://doi.org/10.1016/S0261-3069(03)00123-7
6. Barbara Reggiani, Antonio Segatori, Lorenzo Donati, Luca Tomesani. Prediction of charge welds in hollow profiles extrusion by FEM simulations and experimental validation. *The International Journal of Advanced Manufacturing Technology*. 2013;(69):1855—1872.
   https://doi.org/10.1007/s00170-013-5143-2
7. Longchang Tong, Christoph Becker, Pavel Hora. High efficiency in the simulation of complex extrusion processes using an advanced simulation method. *Materials Today: Proceedings*. 2015;2(10):4726—4731.
   https://doi.org/10.1016/j.matpr.2015.10.005
8. Kim K.J., Lee C.H., Yang D.Y. Investigation into the improvement of welding strength in three dimensional extrusion of tubes using porthole dies. *Journal of Materials Processing Technology*. 2002;(130):426—431.
   https://doi.org/10.1016/S0924-0136(02)00717-3
9. Xiaochen Lu, Junquan Yu, Jianguo Lin, Zhusheng Shi. Investigation of material flow behaviour and microstruc-

ture during differential velocity sideway extrusion. *Procedia Manufacturing.* 2020;(50):226—230.
https://doi.org/10.1016/j.promfg.2020.08.042

10. Koloskov S.S., Sidelnikov S.B., Bersenev A.S., Lopatina E.S., Voroshilov D.S., Katryuk V.P. Technology study of aluminum alloys pipe pressing with use of computer simulation programs. *Proizvodstvo Prokata.* 2019;(12):23—28. (In Russ.).
https://doi.org/10.31044/1814-4632-2019-0-12-23-28
Колосков С.С., Сидельников С.Б., Берсенев А.С., Лопатина Е.С., Ворошилов Д.С., Катрюк В.П. Исследование технологии прессования труб из алюминиевых сплавов с применением программ компьютерного моделирования. *Производство проката.* 2019;(12):23—28.
https://doi.org/10.31044/1814-4632-2019-0-12-23-28
11. Junquan Yu, Guoqun Zhao. Interfacial structure and bonding mechanism of weld seams during porthole die extrusion of aluminum alloy profiles. *Materials Characterization.* 2018;(138):56—66.
https://doi.org/10.1016/j.matchar.2018.01.052
12. Crosio Michele, Hora David, Becker Christoph, Hora Pavel. Realistic representation and investigation of charge weld evolution during direct porthole die extrusion processes through FE-analysis. *Procedia Manufacturing.* 2018;(15):232—239.
https://doi.org/10.1016/j.promfg.2018.07.214
13. Junquan Yu, Guoqun Zhao. Study on welding quality in the porthole die extrusion process of aluminum alloy profiles. *Procedia Engineering.* 2017;(207): 401—406.
https://doi.org/10.1016/j.proeng.2017.10.795
14. Junquan Yu, Guoqun Zhaoa, Weichao Cuib, Cunsheng Zhanga, Liang Chen. Microstructural evolution and mechanical properties of welding seams in aluminum alloy profiles extruded by a porthole die under different billet heating temperatures and extrusion speeds. *Journal of Materials Processing Technology.* 2017;(247):214—222. https://doi.org/10.1016/j.jmatprotec.2017.04.030
15. Bakker A.J.D., Katgerman L., Zwaag S.V.D. Analysis of the structure and resulting mechanical properties of aluminium extrusions containing a charge weld interface. *Journal of Materials Processing Technology.* 2016;(229): 9—21.
https://doi.org/10.1016/j.jmatprotec.2015.09.013
16. Bingol Sedat, Bozaci Atilla. Experimental and numerical study on the strength of aluminum extrusion welding. *Materials.* 2015;8(7):4389—4399.
https://doi.org/10.3390/ma8074389
17. Mahmoodkhani Y., Wells M., Parson N., Poole W.J. Numerical modelling of the material flow during extrusion of aluminium alloys and transverse weld formation. *Journal of Material Processing Technology.* 2014;(214):688—700.
https://doi.org/10.1016/j.jmatprotec.2013.09.028
18. Stebunov S., Biba N., Lishny A., Jiao L. Practical implementation of numerical modeling to optimization of extrusion die design for production of complex shape profiles. *Aluminium Extrusion and Finishing.* 2013;(4):20—24.
http://www.qform3d.co.uk/files_uk/2013_0002_0.pdf
19. Libura W., Rękas A. Numerical modelling in designing aluminium extrusion in: aluminium alloys: New trends in fabrication and applicationsed. Ed. by Zaki Ahmad. INTECH, 2012. P. 137—157. https://doi.org/10.5772/51239
20. Koloskov S., Sidelnikov S., Voroshilov D. Modeling process of semi-continuous extrusion of hollow 6063 aluminum alloy profiles using QForm extrusion. *Solid State Phenomena.* 2021;(316):288—294.
https://doi.org/10.4028/www.scientific.net/SSP.316.288
21. Dovzhenko N.N., Sidelnikov S.B., Vasina G.I. Computer-aided design for metal pressing technology. Scientific methodological support. Krasnoyarsk: GATsMiZ, 2000. 194 p. (In Russ.).
Довженко Н.Н, Сидельников С.Б, Васина Г.И. Система автоматизированного проектирования технологии прессования металлов. Научное методическое обеспечение. Красноярск: ГАЦМиЗ, 2000. 194 с.
22. Aleshin V.P. Calculation of working bands of press dies. *Tekhnologiya legkikh splavov.* 1990;(1):30—33. (In Russ.).
Алешин В.П. Расчет рабочих поясков прессовых матриц. *Технология легких сплавов.* 1990;(1):30—33.
23. Gun G.Ya., Averchenko A.F., Stebunov S.A. On the method of computer-aided design of press dies. *Izvestiya. Ferrous Metallurgy.* 1985;(7):92—95. (In Russ.).
Гун Г.Я., Аверченко А.Ф., Стебунов С.А. К методике автоматизированного проектирования прессовых матриц. *Известия вузов. Черная металлургия.* 1985;(7):92—95.
24. Eidelnant S.B., Korpakov B.P., Maizlin Ya.L. Designing with the help of a computer matrices for pressing profiles. *Tsvetnye Metally.* 1982;(3):81—82. (In Russ.).
Эйдельнант С.Б, Корпаков Б.П, Майзлин Я.Л. Проектирование с помощью ЭВМ матриц для прессования профилей. *Цветные металлы.*1982;(3):81—82.
25. Stepanskiy L.G. Estimated estimates of press matrix calibrations. *Kuznechno-shtampovochnoe proizvodstvo.* 1983;(5):25—27. (In Russ.).
Степанский Л.Г. Расчетные оценки калибровок пресс-матриц. *Кузнечно-штамповочное производство.* 1983;(5):25—27.
26. QForm-Extrusion (электронный ресурс). Моделирование прессования профилей. URL: https://qform3d.ru/products/extrusion (дата обращения: 20.04.2023).
QForm-Extrusion (electronic resource). Modeling of

extrusion of profiles. URL: https://qform3d.ru/products/extrusion (accessed: 20.04.2023). (In Russ.).

27. Knyaz'kin I.S., Dyuzhev A.M., Vlasov A.V., Gladkov Yu.A., Lishniy A.I. Technique for computer-aided design of matrix tooling for pressing aluminum alloys. *Science and Education. MSTU im. N.E. Bauman* (Electron. Magazine). 2015;(8):1—13. (In Russ.).
Князькин И.С., Дюжев А.М., Власов А.В., Гладков Ю.А., Лишний А.И. Методика автоматизированного проектирования матричной оснастки для прессования алюминиевых сплавов. *Наука и образование. МГТУ им. Н.Э. Баумана* (Электрон. журнал). 2015;(8):1—13.
28. Dyuzhev A.M., Knyazkin I.S., Lishnii A.I., Solov'yov D.A., Stebunov D.A. QForm Extrusion Die Designer (QExDD) program for automated element-by-element parametric design of matrix equipment for extrusion of profiles: Certificate 2015613466 (RF). 2015. (In Russ.).
Дюжев А.М., Князькин И.С., Лишний А.И., Соловьев Д.А., Стебунов Д.А. Программа для автоматизированного поэлементного параметрического проектирования матричной оснастки для прессования профилей QForm Extrusion Die Designer (QExDD): Св-во 2015613466 (РФ). 2015.
29. Levanov A.N., Kolmogorov V.L., Burkin S.P., Kartak B.R., Ashpur Yu.V., Spasskii Yu.I. Contact friction in metal forming processes. Moscow: Metallurgiya, 1976. 352 p. (In Russ.).
Леванов А.Н., Колмогоров В.Л., Буркин С.П., Картак Б.Р., Ашпур Ю.В., Спасский Ю.И. Контактное трение в процессах обработки металлов давлением. М.: Металлургия. 1975. 352 с.
30. Laptev A.M., Tkachenko Ya.Yu., Zhabin V.I. Construction of a diagram for determining the coefficient of friction in the Levanov formula using the ring upset method. *Obrabotka materialov davleniem.* 2011;3(28):129—132. (In Russ.).
Лаптев А.М., Ткаченко Я.Ю., Жабин В.И. Построение диаграммы для определения коэффициента трения в формуле Леванова по методу осадки кольца. *Обработка материалов давлением*. 2011;3(28):129—132.

Information about the authors

Sergei B. Sidelnikov – Dr. Sci. (Eng.), Professor of the Department of Metal Forming (MF) of the School of Non-Ferrous Metals (SNFM) of Siberian Federal University (SFU).
https://orcid.org/0000-0002-5611-2808
E-mail: sbs270359@yandex.ru

Sergei S. Koloskov – Postgraduate Student of the Department of MF of SNFM, SFU.
https://orcid.org/0000-0002-4076-7295
E-mail: kelos36@mail.ru

Nikolai N. Dovzhenko – Dr. Sci. (Eng.), Professor of the Department of Mechanical Engineering of the Polytechnic School, SFU.
https://orcid.org/0000-0001-7608-0615
E-mail: n.dovzhenko@bk.ru

Yurii A. Gorbunov – Dr. Sci. (Eng.), Professor of the Department of MF of SNFM, SFU.
https://orcid.org/0000-0001-9835-7881
E-mail: j.a.gorbunov@gmail.com

Denis S. Voroshilov – Cand. Sci. (Eng.), Associate Professor, Head of the Department of MF of SNFM, SFU.
https://orcid.org/0000-0002-1406-3665
E-mail: sibdrug@mail.ru

Информация об авторах

Сергей Борисович Сидельников – д.т.н., профессор кафедры обработки металлов давлением (ОМД) Института цветных металлов (ИЦМ) Сибирского федерального университета (СФУ).
https://orcid.org/0000-0002-5611-2808
E-mail: sbs270359@yandex.ru

Сергей Сергеевич Колосков – аспирант кафедры ОМД, ИЦМ СФУ.
https://orcid.org/0000-0002-4076-7295
E-mail: kelos36@mail.ru

Николай Николаевич Довженко – д.т.н., профессор кафедры машиностроения Политехнического института СФУ.
https://orcid.org/0000-0001-7608-0615
E-mail: n.dovzhenko@bk.ru

Юрий Александрович Горбунов – д.т.н., профессор кафедры ОМД, ИЦМ СФУ.
https://orcid.org/0000-0001-9835-7881
E-mail: j.a.gorbunov@gmail.com

Денис Сергеевич Ворошилов – к.т.н., доцент, заведующий кафедрой ОМД, ИЦМ СФУ.
https://orcid.org/0000-0002-1406-3665
E-mail: sibdrug@mail.ru

Contribution of the authors

S.B. Sidel'nikov – formulated main concept, formulated purpose of the study, wrote the manuscript, formulated conclusions.

S.S. Koloskov – performed calculations, performed simulation, wrote the manuscript.

N.N. Dovzhenko – developed methods of tool design, substantiated its application, analyzed the research results.

Yu.A. Gorbunov – scientific advising, revised the manuscript and conclusions.

D.S. Voroshilov – prepared and performed experiments, wrote the experimental section of the manuscript.

Вклад авторов

С.Б. Сидельников – формирование основной концепции, постановка цели исследования, подготовка текста статьи, формулировка выводов.

С.С. Колосков – осуществление расчетов, проведение моделирования, подготовка текста статьи.

Н.Н. Довженко – разработка методики проектирования инструмента и обоснование ее применения, анализ результатов исследований.

Ю.А. Горбунов – научное руководство, корректировка текста и выводов.

Д.С. Ворошилов – подготовка и проведение экспериментов, подготовка текста по экспериментальной части.

The article was submitted 07.02.2023, revised 12.04.2023, accepted for publication 20.04.2023

Статья поступила в редакцию 07.02.2023, доработана 12.04.2023, подписана в печать 20.04.2023

UDC 620.172.2.087.45
https://doi.org/10.17073/0021-3438-2023-3-79-88

Research article
Научная статья

Using the method of correlation of digital images for plotting stress–strain curves in true coordinates

A.D. Monakhov[1], **M.M. Gulyaev**[2], **N.E. Gladysheva**[2], **O.Yu. Kopteltseva**[2], **V.V. Avtaev**[1], **N.O. Yakovlev**[1], **I.V. Gulina**[1]

[1] **All-Russian Research Institute of Aviation Materials of the National Research Center "Kurchatov Institute"**
17 Radio str., Moscow, 105005, Russia

[2] **Joint Stock Company "Design Bureau of Instrument Engineering named after Academician A.G. Shipunov"**
59 Shcheglovskaya Zaseka str., Tula, 300004, Russia

✉ Anton D. Monakhov (ant.monakhov@gmail.com)

Abstract: This article describes the features of determining strain curves in true stress–true strain coordinates, using samples of circular cross section from Al–Cu–Mg–Zn aluminum alloy. The calculation and experimental methods of determining true stresses and strains were compared. Calculation methods based on the condition of volume constancy may not reflect actual regularities of deformation at the stage of strain localization in the considered material. Nevertheless, the use of systems of digital image correlation (DIC) allows measurements of both the geometrical sizes of deformed sample and strain fields on its surface to be performed, including on the sample neck. It was demonstrated that the measurement error of the sample diameter by the coordinate field was 0.02 mm at the instance of destruction. In order to improve the measurement precision, an increase in the recording frequency in proportion to increase in strain rate was proposed, as well as measuring the surface coordinates from both sides of the sample. It is also possible to supplement the strain curves obtained by DIC optical systems with the measurements of true fracture stress, and the true fracture strain determined by calculations on the destructed sample. The presented methods of analysis of plastic flow by direct measurement of field displacements and strains allow actual regularities between true stresses and strains at the interval of irregular plastic strain to be established. This cannot be achieved by analytical conversion of conventional curve. The obtained hardening coefficients and strain curves can be used for simulation and design of machinery structures and parts.

Keywords: true stress, true strain, plastic strain, strain field, correlation of digital images, strain hardening.

For citation: Monakhov A.D., Gulyaev M.M., Gladysheva N.E., Kopteltseva O.Yu., Avtaev V.V., Yakovlev N.O., Gulina I.V. Using the method of correlation of digital images for plotting stress–strain curves in true coordinates. *Izvestiya. Non-Ferrous Metallurgy.* 2023;29(3):79–88. https://doi.org/10.17073/0021-3438-2023-3-79-88

Применение метода корреляции цифровых изображений для построения диаграмм деформирования в истинных координатах

А.Д. Монахов[1], **М.М. Гуляев**[2], **Н.Е. Гладышева**[2], **О.Ю. Коптельцева**[2], **В.В. Автаев**[1], **Н.О. Яковлев**[1], **И.В. Гулина**[1]

[1] **Всероссийский научно-исследовательский институт авиационных материалов Национального исследовательского центра «Курчатовский институт»**
105005, Россия, г. Москва, ул. Радио, 17

[2] **АО «Конструкторское бюро приборостроения им. академика А.Г. Шипунова»**
300004, Россия, г. Тула, ул. Щегловская Засека, 59

✉ Антон Дмитриевич Монахов (ant.monakhov@gmail.com)

Аннотация: Приведены особенности определения диаграмм деформирования в координатах «истинное напряжение – истинная деформация» на образцах круглого сечения из алюминиевого сплава системы Al–Cu–Mg–Zn. Выполнено сравнение расчетных и экспериментальных методов определения истинных напряжений и деформаций. Расчетные методы, основанные на применении условия постоянства объема, могут не отражать действительных закономерностей деформирования на этапе локализации деформации в материале исследуемого образца, в то время как использование систем корреляции цифровых изображений (КЦИ) позволяет проводить измерения как геометрических размеров деформируемого образца, так и полей деформаций на его поверхности, в том числе непосредственно в шейке образца. Показано, что ошибка измерения диаметра образца по полю координат в момент разрушения составила 0,02 мм. С целью повышения точности измерения предложено увеличение частоты съемки пропорционально возрастанию скорости деформирования, а также проведение измерения координат поверхности с двух сторон образца. Также возможно дополнять полученные с помощью оптических систем КЦИ кривые деформирования результатами измерения истинного разрушающего напряжения и истинной разрушающей деформацией, определенными расчетным способом по разрушенному образцу. Представленные способы исследования пластического течения материала непосредственным измерением полей перемещений и деформаций позволяют устанавливать действительные закономерности между истинными напряжениями и деформациями на участке неравномерного пластического деформирования, чего достичь аналитическим пересчетом условной диаграммы невозможно. Полученные коэффициенты упрочнения и кривые деформирования могут быть использованы при моделировании и проектировании конструкций и деталей машин.

Ключевые слова: истинное напряжение, истинная деформация, пластическая деформация, поле деформации, корреляция цифровых изображений, деформационное упрочнение.

Для цитирования: Монахов А.Д., Гуляев М.М., Гладышева Н.Е., Коптельцева О.Ю., Автаев В.В., Яковлев Н.О., Гулина И.В. Применение метода корреляции цифровых изображений для построения диаграмм деформирования в истинных координатах. *Известия вузов. Цветная металлургия*. 2023;29(3):79–88.
https://doi.org/10.17073/0021-3438-2023-3-79-88

Introduction

Machinery structures and parts should be designed with consideration for provision of their safe operation. Permissible operation stresses are determined by criteria of ultimate stress state [1; 2]. This in their turn are compared with the results obtained upon uniaxial strain [3—6]. Standard tension or compression state allow strain curve in stress—strain coordinates to be established (curve *1* in Fig. 1) [7]. Stress strain curves can also be referred to as conditional, since the surface area of transversal cross section and strain measurement base are assumed to be constant throughput the test. In order to establish true regularities between stress and strain [8], as well as during simulation of plasticity problems by finite element method [9; 10], true stresses and true strains (curve *2* in Fig. 1) need to be applied in operations. These are calculated by correlating the load and the absolute elongation of the sample to the actual area of true surface area of transversal cross section and the length of working part, respectively.

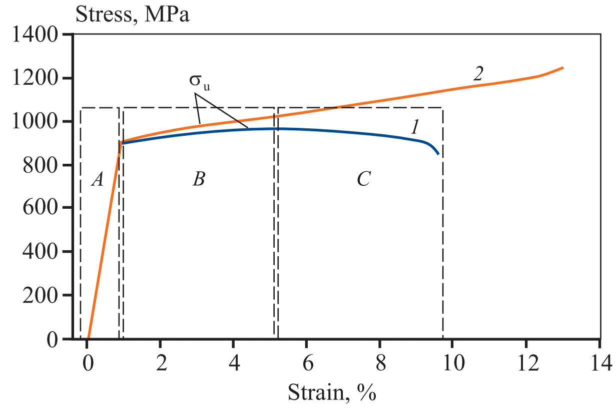

Fig. 1. Conditional (*1*) and true (*2*) strain curves

Рис. 1. Условная (*1*) и истинная (*2*) диаграммы деформирования

The development of computation devices has allowed the regularities of material flow to be studied not only by analytical methods [8; 11], but also by direct measurements of displacements, strains or geometry of the object in the region of local stability loss. This work considers the use of optical contactless tensometry systems in determining strain curves in true coordinates. The calculations of true stresses by analytical and experimental methods of direct recording of strain and surface area of transversal cross section in the region of plastic flow were compared for isotropic materials.

Calculation method of determination of strain curves in true coordinates

Three characteristic segments in conditional strain curve of plastic material can be highlighted. The segment of elastic plastic strain (region *A* in Fig. 1) is characterized by an insignificant difference in the conditional and true curves due to moderate strains. The hardening segment (region *B* in Fig. 1) is characterized by a monotonous increase in stress both in true and in conditional coordinates, due to a the limitation of ultimate strength (σ_u). In the segment of localization of plastic strain (region *C* in Fig. 1) neck formation can be observed. This can be seen in the transfer from uniform strain, acting along the entire length of working part, to a localized one resulting in load drop upon strain growth. The region of neck formation is also characterized by the transfer from a uniaxial (simple) stressed state to complex stress strain state. This exerts significant influence on strain [12; 13].

Using the calculation method, the surface area of transversal cross section during test for the segments of elastic plastic strain and hardening can be determined from the condition of volume constancy [11]:

$$F_0 dz = F(1 + \varepsilon)dz, \tag{1}$$

where F_0 is the surface area of transversal cross section at initial test time; F is the surface area of transversal cross section during strain; ε is the relative strain; dz is the absolute change of length during strain.

The surface area of transversal cross section can be expressed using Eq. (1):

$$F = F_0/(1 + \varepsilon). \tag{2}$$

True stresses upon uniform strain equal to the ratio of load upon strain to the surface area of transversal cross section can be determined by Eq. (2):

$$s = P/F = \sigma(1 + \varepsilon), \tag{3}$$

where s is the true stress; P is the load during strain; σ is the conditional stress.

True strains can be determined as the ratio of absolute elongation to total length of canulated zone [11]:

$$\varphi = \int_{l_0}^{l} dl/l = \ln(l/l_0) = \ln(1 + \varepsilon), \tag{4}$$

where φ is the true strain; l is the total length of calculated zone; l_0 is the initial length of working zone.

The strain curve in true coordinates for uniform strain is plotted by Eqs. (3), (4). True fracture strain and true fracture stress are applied to the strain curve and calculated as follows [11; 12]:

$$s_f = \sigma_r / (1 - \psi), \tag{5}$$

where s_f are the true fracture stresses; σ_r are the conditional stresses upon rupture; ψ is the relative reduction of area after rupture;

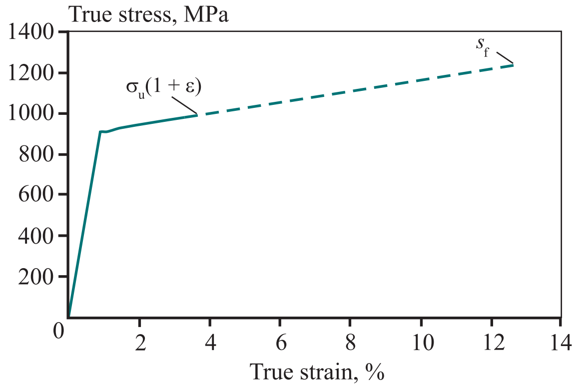

Fig. 2. Schematic strain curve in true coordinates obtained by calculations

Рис. 2. Схематичная диаграмма деформирования в истинных координатах, полученная расчетным способом

$$\varphi_f = \ln(1 - \psi)^{-1}, \tag{6}$$

where φ_f is the true fracture strain.

The calculation method of plotting strain curves in true coordinates (Fig. 2) does not require special equipment, and can be characterized by its simplicity. However, the curve may not reflect actual regularities of strain at the segment of localization of plastic strain. This method is recommended for brittle materials.

Determining strain curves in true coordinates using strain fields

Observation of the fields of strains and displacements allows the true stresses and strains for all strain segments to be calculated. Several methods are available to determine the fields of strains and displacements [14; 15]. For reasons of precision [16] and simplicity, the method of digital image correlation (DIC) was selected.

The DIC method is based on video recording the sample during the test and alternate comparison of frames before and after strain, The aim was to determine displacements of uniformly subdivided field segments (subregions). A chaotic spotted structure (speckle pattern) is applied beforehand onto a sample so that each sub-region differs from the others. The fields of displacements and strains are calculated using the displacement of sub-regions. Two cameras allow the position of points to be determined and their displacement in three coordinates to be calculated.

The DIC systems allow local strain fields to be formed over the entire analyzed surface, including the neck zone, while extensometers perform measurements between two predefined points. Thus, the strain determined by extensometers at the segment of neck formation is the arithmetic mean between localized and uniform plastic strain according to measurements. A uniform or localized deformation cannot be distinguished from a general deformation.

Substituting the mean arithmetic value of longitudinal strain ($\varepsilon_{yy}^{\max}$) along the transversal section of sample neck (Fig. 3) into Eqs. (3) and (4) in place of the relative strain (ε), we can obtain equations for determining true stresses and strains along longitudinal component of strain tensor for any strain stage [17]:

$$s = \sigma(1 + \varepsilon_{yy}^{\max}), \tag{7}$$

$$\varphi = \ln(1 + \varepsilon_{yy}^{\max}). \tag{8}$$

This method allows analysis at all strain stages to be performed. However, Eqs. (7) and (8) were derived assuming the volume constancy for isotropic materials. Therefore, the possibility of applying these interrelations for orthotropic and anisotropic materials should be studied in more detail.

When observing the positions of sub-regions in the calculation of the fields of displacements and strains, the sample diameter at any time of tests along the entire length of the considered region can be measured. A circle was inscribed using the least square method into the coordinates of transversal section in the plane of the maximum reduction of sample area. The sample diameter in the course of strain was determined by Eq. (9):

$$d_i = 2[(x - a)^2 + (y - b)^2]^{1/2}, \tag{9}$$

where x, y are the coordinates of circumference point along the respective axes; a, b are the coordinates of circumference center along the axes X, Y, respectively.

Experimental

Strain curves in true coordinates were determined on a sample of circle cross section from aluminum alloy Al—Cu—Mg—Zn. The sample diameter was 5.92 mm, and the length of working part: 30 mm.

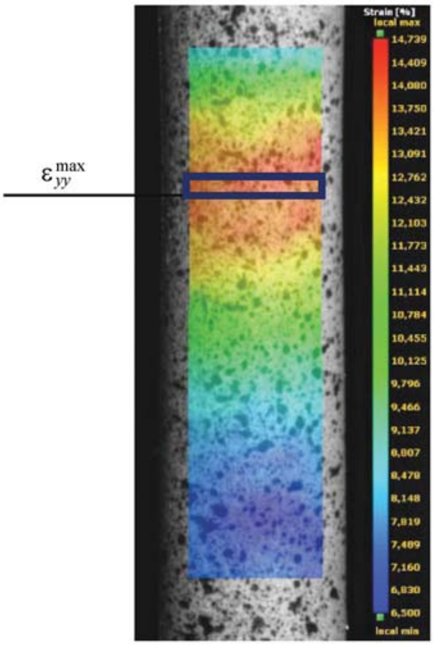

Fig. 3. Field of longitudinal component of strain tensor ε_{yy}

Рис. 3. Поле продольной компоненты тензора деформации ε_{yy}

The tests were carried out using an electromechanical test machine with a rated load of 100 kN at constant speed of active clamp, equal to 2 mm/min. Throughout the test, the longitudinal strain (ε) was recorded using a contactless extensometer. The strain fields were determined using a DIC system comprising of two cameras with a resolution of 3 megapixels, providing a pixel density of 31 dot/mm. The subregion step was 8 dots, and the subregion size: 25×25 dots. The recording frequency was 5 Hz. The physicomechanical properties determined by conditional strain curve (Fig. 4) are summarized in Table 1, the relative elongation (δ_5) and the relative reduction of area (ψ) were determined in accordance with the State standard GOST 1497-84.

In Fig. 5, numbers *1* and *2* denote the coordinates of points of section in initial state and preceding the sample destruction, respectively. The diameter of inscribed circle for a sample before strain (line *1* in Fig. 5) was equal to 5.92 mm, and for a sample before destruction (*2* in Fig. 5) to 5.24 mm.

The actual sample diameter after rupture was assumed to be higher than that measured along inscribed circle by the elastic constituent of ε_{xx}. It was also assumed to be equal to 5.25 mm, since during measuring of diameter the sample was still in stressed state. However, the actual sample diameter after rup-

Table 1. **Physicomechanical properties**

Таблица 1. Физико-механические характеристики исследуемого образца

Poisson ratio μ	Elasticity modulus *E*, GPa	Yield stress $\sigma_{0,2}$, MPa	Ultimate tensile strength σ_u, MPa	Rupture stress σ_r, MPa	Relative elongation δ_5, %	Relative reduction of area ψ, %
0.32	72	600	640	593	10.0	20.0

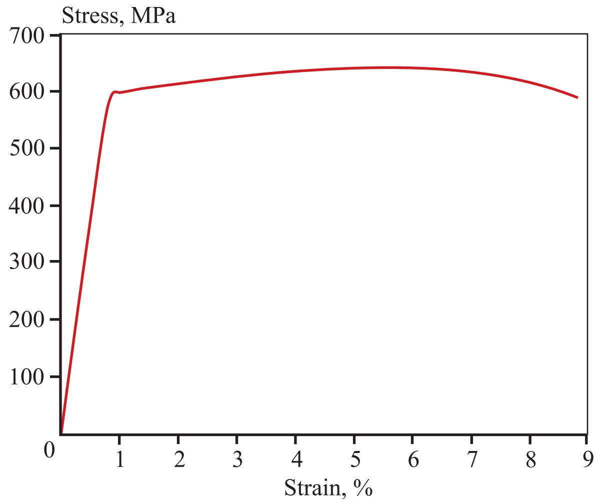

Fig. 4. Strain curve in conditional coordinates

Рис. 4. Диаграмма деформирования в условных координатах

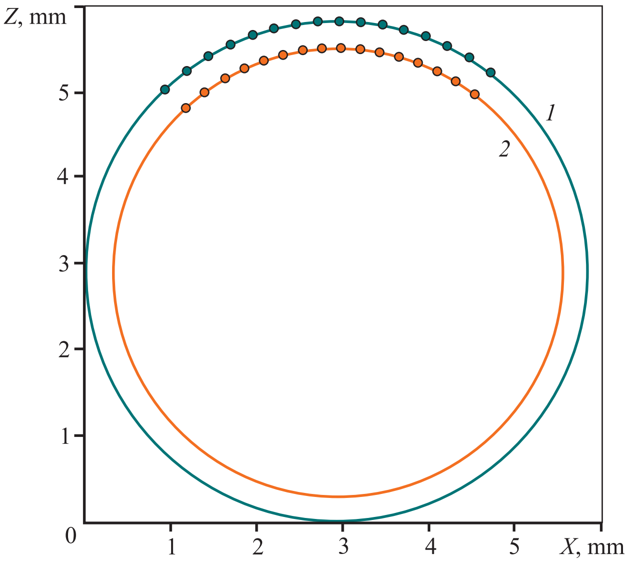

Fig. 5. Diameter measurement by inscribed circle

Рис. 5. Измерение диаметра образца по вписанной окружности

ture was lower than that measured along the inscribed circle and was equal to 5.23 mm. This can be attributed to the fact that the test was carried out at a constant active clamp speed and constant recording frequency. Thus, as a consequence of strain localization the strain rate was increased from 0.0002 s^{-1} at the elastic segment to 0.018 s^{-1} at the instance preceding destruction. Thus, Fig. 6 illustrated true strain as a function of test time (curve *1*) and its derivative of time: strain rate (curve *2*) for segments of elastic plastic strain (*A*), hardening (*B*) and localization of plastic flow (*C*). Respectively, the recording at the frequency of 5 Hz allowed true strain to be resolved with a precision of 0.0036 m/m per frame at the instance preceding destruction.

The true stresses were calculated using the determined diameters:

$$S = P/F = 4P/(\pi d_i^2), \qquad (10)$$

where *P* is the load during strain, d_i is the sample diameter during strain.

As a consequence of complicated and heterogeneous stress strain state, occurring in the region of strain localization [12; 13], the strain can be heterogeneous. Therefore, the profile of transversal cross section will differ from a circle. In order to account for eccentricity when calculating the surface area of transversal cross section during strain, it is recommended that the fields of displacement and strain on two opposite sides be studied by four cameras calibrated as a single system [18].

Based on test results, the strain curves in true coordinates were plotted Fig. 7 shows Curve *1*, based on calculations, curve segment (dashed line), linearly interpolated up to the points determined by Eqs. (5), (6), as well as Curve *2*, plotted on the basis of longitudinal Lagrange strain, ε_{yy}, as well as curve *3*, calculated by actual change in diameter during strain.

The elastic segments of loading in the strain curves in true coordinates coincide for all calculation methods. Differences are observed in the hardening segment.

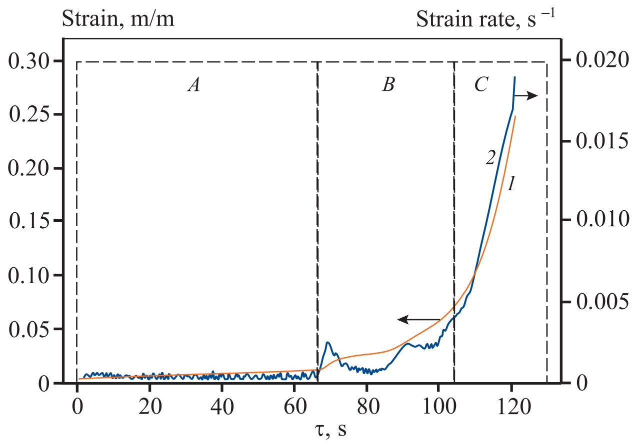

Fig. 6. Relative strain as a function of test duration

Рис. 6. Диаграмма зависимости относительной деформации от времени испытания

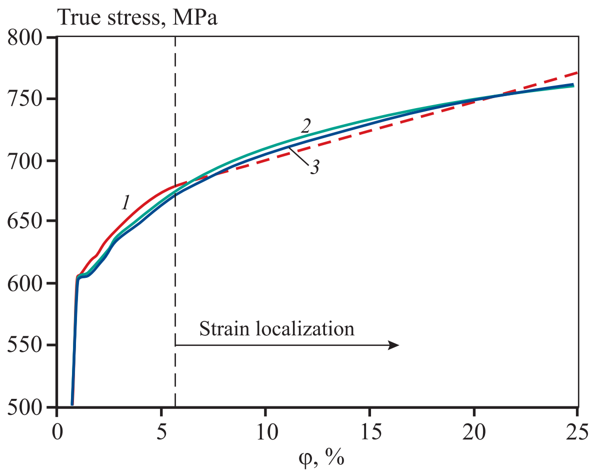

Fig. 7. Strain curves in in true coordinates

Рис. 7. Диаграммы деформирования в истинных координатах

The most common and simplest approximation method of plastic behavior is the strain hardening exponent [19—21], Its coefficients can be also used to describe strain hardening of material in the course of finite element simulation:

$$S = Kp^n, \tag{11}$$

where K is the strength coefficient determined by the least square method, MPa; n is the coefficient of strain hardening determined by the least square method; p is the true plastic strain; S is the true stress, MPa.

Figure 8 illustrates the hardening segments in true stress—true plastic strain coordinates for strain curves in true coordinates. This is obtained by calculations (Fig. 8, *a*): by the field of longitudinal strains in the region of strain localization (Fig. 8, *b*), as well as calculating the sample diameter by means of an inscribed circle in the coordinates of points of the highest longitudinal strains (Fig. 8, *c*). The dashed line in Fig. 8 shows their exponential model of approximation obtained by the least square method on the basis of data of logarithmically linearized hardening curve. The calculated results are summarized in Table 2.

The approximation model was determined for the hardening segment obtained by means of calculation, but only to ultimate strength. This indicates that it cannot be used for strains exceeding the ultimate strength. At the same time, the methods based on DIC systems allow true stresses to be determined as a function of true strain up to sample destruction. However, for the more uniform control of strain in the sample neck by optical system, the test machine needs to be controlled by true strains or for the recoding frequency of DIC system to be increased in proportion to strain rate. Otherwise, the strain curves obtained by DIC systems must be supplemented by true fracture stress and

Table 2. **Calculations of strain curves in true coordinates**

Таблица 2. Результаты расчетов диаграмм деформирования в истинных координатах

Method of determination	K, MPa	n	True fracture stress (S_f), MPa	True fracture strain (φ_f), %
Calculations	792	0.0518	771	25.1
By longitudinal component of strain tensor	834	0.0685	761	24.9
By change in diameter	831	0.0687	762	24.9

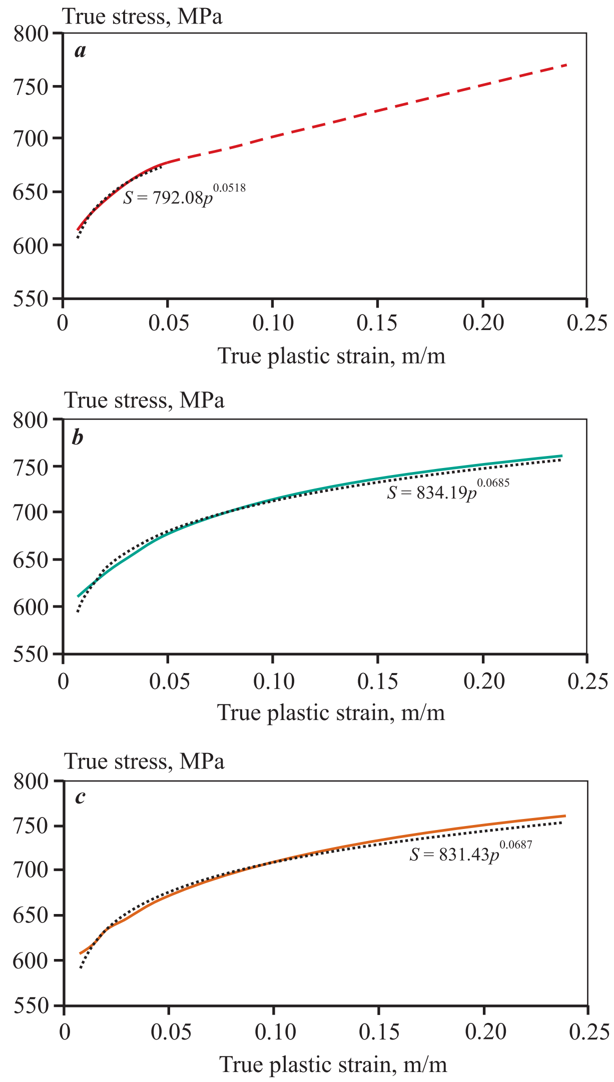

Fig. 8. Hardening segments of strain curves in true coordinates obtained by calculations (***a***), by field of longitudinal strain in sample neck (***b***) and by change in diameter (***c***)

Рис. 8. Участки упрочнения диаграмм деформирования в истинных координатах, полученные расчетным методом (***a***), по полю продольных деформаций в шейке образца (***b***) и по изменению диаметра образца (***c***)

true fracture strain determined by calculations using destructed sample.

Conclusions

The strain curves in true coordinates provide data on the strain hardening of material and can be used in the simulation and design of parts and structures [9; 22].

The research methods of plastic flow by direct measurement of fields of displacement and strain allow actual regularities between true stresses and strains at the interval of irregular plastic strain to be established. This cannot be achieved by the analytical conversion of a conventional curve. In addition, it should be taken into account that after neck formation, the strain rate increases. This results in additional errors in the calculation of true stresses and strains, which at the instance of sample destruction can reach 1.3 % with respect to the values obtained by actual measurement of sample after destruction. However, the calculation method of curve determination in true coordinates is simple. It does not require additional hard- or software. True fracture stress and true strain upon breakage determined by means of this method can supplement the results of actual measurements.

The selection of calculation methods of strain curves in true coordinates is stipulated by the requirement for the completeness of results, as well as the material type. It should also be mentioned that both methods based on the use of DIC systems provide equal amount of data, and the difference between the results obtained in this work can be neglected (the difference between true fracture stresses is less than 0.2 %). However, the use of the longitudinal component of strain tensor upon analysis of anisotropic material can lead to calculation errors. Therefore, the preferred method is based on measurement of actual sample diameter in the course of deformation by using DIC systems on two sides.

References

1. Oreshko E.I., Erasov V.S., Grinevich D.V., Shershak P.V. Review of criteria of durability of materials. *Trudy VIAM*. 2019;(9(81)):108—126. (In Russ.). https://doi.org/10.18577/2307-6046-2019-0-9-108-126
Орешко Е.И., Ерасов В.С., Гриневич Д.В., Шершак П.В. Обзор критериев прочности материалов. *Труды ВИАМ*. 2019;(9(81)):108—126.
2. Yakovlev N.O., Grinevich D.V., Mazalov P.B. Mathematical simulation of the stress-strain state manifesting during compression of a lattice structure manufactured by means of selective laser melting. *Vestnik Moskovskogo gosudarstvennogo tekhnicheskogo universiteta im. N.E. Baumana. Seriya Estestvennye nauki*. 2018;(6(81)):113—127. (In Russ.). https://doi.org/10.18698/1812-3368-2018-6-113-127
Яковлев Н.О., Гриневич Д.В., Мазалов П.Б. Математическое моделирование напряженно-де-

формированного состояния при сжатии сетчатой конструкции, синтезированной методом селективного лазерного сплавления. *Вестник Московского государственного технического университета им. Н.Э. Баумана. Серия Естественные науки*. 2018;(6(81)): 113—127.

3. Kablov E.N., Podzhivotov N.Yu., Lutsenko A.N. About need for creation of uniform information and analysis centerof aviation materials of the Russian Federation. *Problemy mashinostroeniya i avtomatizatsii*. 2019;(3): 28—34. (In Russ.).
Каблов Е.Н., Подживотов Н.Ю., Луценко А.Н. О необходимости создания единого информационно-аналитического центра авиационных материалов РФ. *Проблемы машиностроения и автоматизации*. 2019;(3):28—34.
4. Grinevich A.V., Slavin A.V., Yakovlev N.O., Monakhov A.D., Gulina I.V. On problem of spalling fracture of high-strength steel under quasi-static tension. *Deformatsiya i razrushenie materialov*. 2021;(8):2—7. (In Russ.).
https://doi.org/10.31044/1814-4632-2021-8-2-7
Гриневич А.В., Славин А.В., Яковлев Н.О., Монахов А.Д., Гулина И.В. К вопросу откольного разрушения высокопрочной стали при квазистатическом растяжении. *Деформация и разрушение материалов*. 2021;(8): 2—7.
5. Kablov E.N. Formation of domestic space materials science. *Vestnik RFFI*. 2017;(3):97—105. (In Russ.).
https://doi.org/10.22204/2410-4639-2017-095-03-97-105
Каблов Е.Н. Становление отечественного космического материаловедения. *Вестник РФФИ*. 2017;(3):97—105.
6. Dowling N. Mechanical behavior of materials: Engineering methods for deformation, fracture and fatigue. 4 ed. Essex: Pearson, 2013. 977 p.
7. Oreshko E.I., Erasov V.S., Krylov V.D. Construction of 3d stress-strain diagram for the analysis of mechanical behavior of the material tested at various loading rates. *Aviatsionnye materialy i tekhnologii*. 2018;(2(51)):59—66. (In Russ.).
https://doi.org/10.18577/2071-9140-2018-0-2-59-66
Орешко Е.И., Ерасов В.С., Крылов В.Д. Построение трехмерных диаграмм деформирования для анализа механического поведения материала, испытанного при различных скоростях нагружения. *Авиационные материалы и технологии*. 2018;(2(51)):59—66.
8. Kachanov L.M. Fundamentals of fracture mechanics. Moscow: Nauka, 1974. 311 p. (In Russ.).
Качанов Л.М. Основы механики разрушения. М.: Наука, 1974. 311 с.
9. Petrík A., Ároch R. Usage of true stress-strain curve for FE simulation and the influencing parameters. *IOP Conference Series: Materials Science and Engineering*. 2019;566:012025.
http://dx.doi.org/10.1088/1757-899X/566/1/012025
10. Terhorst M., Ozhoga-Maslovskaja O., Trauth D., Mattfeld P., Klocke F. Finite element-based modeling of strain hardening in metal forming. *Steel Research International*. 2016;87(10):1323—1332.
https://doi.org/10.1002/srin.201500375
11. Birger I.A., Mavlyutov R.R. Strength of materials. Moscow: Nauka, 1986. 561 p. (In Russ.).
Биргер И.А., Мавлютов Р.Р. Сопротивление материалов. М.: Наука, 1986. 561 с.
12. Osintsev A.V., Plotnikov A.S., Morozov E.M., Lubkova E.Yu. On the location of a neck formation during the tension of cylindrical specimens. *Letters on Materials*. 2017;7(3):260—265.
https://doi.org/10.22226/2410-3535-2017-3-260-265
13. Junfu Chen, Zhiping Guan, Pinkui Ma, Zhigang Li, Xiangrui Meng. The improvement of stress correction in post-necking tension of cylindrical specimen. *The Journal of Strain Analysis for Engineering Design*. 2019;54(3): 209—222.
http://dx.doi.org/10.1177/0309324719852875
14. Monakhov A.D., Yakovlev N.O., Avtaev V.V., Kotova E.A. Destructive methods for determining residual stresses (review). *Trudy VIAM*. 2021;(9(103)):95—104. (In Russ.).
http://dx.doi.org/10.18577/2307-6046-2021-0-9-95-104
Монахов А.Д., Яковлев Н.О., Автаев В.В., Котова Е.А. Разрушающие методы определения остаточных напряжений (обзор). *Труды ВИАМ*. 2021;(9(103)): 95—104.
15. Huang L., Korhonen R.K., Turunen M.J., Finnilä M.A.J. Experimental mechanical strain measurement of tissues. *Peer J*. 2019;7:e6545.
https://doi.org/10.7717%2Fpeerj.6545
16. Sutton M.A., Orteu J.-J., Schreier H.W. Image correlation for shape, motion and deformation measurements. Columbia, SC, USA: University of South Carolina, 2009. 322 p.
17. Yang L., Smith L. Measure strain distribution using digital image correlation (DIC) for tensile tests. Final Report. Auto/Steel Partnership. 2010. 26 p.
18. Junrui L., Guobiao Y., Thorsten S. A method of the direct measurement of the true stress—strain curve over a large

strain range using multi-camera digital image correlation. *Optics and Lasers in Engineering*. 2018;(107):194—201. https://doi.org/10.1016/j.optlaseng.2018.03.029

19. Shchetinina N.D., Rudchenko A.S., Selivanov A.A. The approaches that are used for developed of optimal strain modes of aluminum-lithium alloys (review). *Trudy VIAM*. 2019;(8(90)):20—34. (In Russ.). https://doi.org/10.18577/2307-6046-2020-0-8-20-34
Щетинина Н.Д., Рудченко А.С., Селиванов А.А. Применение методов математического моделирования при разработке режимов деформации алюминий-литиевых сплавов (обзор). *Труды ВИАМ*. 2019;(8(90)):20—34.
20. Poole W.J., Embury J.D., Lloyd D.J. Work hardening in aluminium alloys. In: *Fundamentals of aluminium metallurgy*. Ed. Roger Lumley. Woodhead Publishing Limited, 2011. P. 307—344. https://doi.org/10.1533/9780857090256.2.307
21. Den Uijl N.J., Carless L.J. Advanced metal-forming technologies for automotive applications. In: *Advanced materials in Automotive Engineering*. Ed. Jason Rowe. Woodhead Publishing Limited, 2012. P. 28—56. https://doi.org/10.1533/9780857095466.28
22. Faridmehr I., Osman M.H., Adnan A.B., Nejad A.F., Hodjati R., Azimi M. Correlation between engineering stress-strain and true stress-strain curve. *American Journal of Civil Engineering and Architecture*. 2014;2(1):53—59. http://dx.doi.org/10.12691/ajcea-2-1-6

Information about the authors

Anton D. Monakhov – Engineer of the Laboratory of Strength and Reliability of Aircraft Materials, All-Russian Research Institute of Aviation Materials (VIAM) of the National Research Center (NRC) “Kurchatov Institute”.
https://orcid.org/0000-0002-8249-5814
E-mail: ant.monakhov@gmail.com

Maksim M. Gulyaev – Head of the Department of the Joint Stock Company (JSC) “Design Bureau of Instrument Engineering (KBP) named after Academician A.G. Shipunov”.
https://orcid.org/0000-0003-0058-4694
E-mail: guliaevmay@mail.ru

Natalya E. Gladysheva – Head of the Sector of the JSC “KBP named after Academician A.G. Shipunov”.
https://orcid.org/0000-0001-9423-1683
E-mail: naeglad@mail.ru

Olga Yu. Kopteltseva – Leading Research Engineer of the JSC “KBP named after Academician A.G. Shipunov”.
https://orcid.org/0000-0002-7736-0480
E-mail: olya_moshkina@mail.ru

Vitaliy V. Avtaev – Leading Engineer of the Laboratory of Strength and Reliability of Aircraft Materials, NRC “Kurchatov Institute” – VIAM.
https://orcid.org/0000-0001-6825-0602
E-mail: darkee@mail.ru

Информация об авторах

Антон Дмитриевич Монахов – инженер лаборатории прочности и надежности материалов воздушного судна Всероссийского научно-исследовательского института авиационных материалов (ВИАМ) Национального исследовательского центра (НИЦ) «Курчатовский институт».
https://orcid.org/0000-0002-8249-5814
E-mail: ant.monakhov@gmail.com

Максим Михайлович Гуляев – начальник отдела АО «Конструкторское бюро приборостроения (КБП) им. академика А.Г. Шипунова».
https://orcid.org/0000-0003-0058-4694
E-mail: guliaevmay@mail.ru

Наталья Евгеньевна Гладышева – начальник сектора АО «КБП им. А.Г. Шипунова».
https://orcid.org/0000-0001-9423-1683
E-mail: naeglad@mail.ru

Ольга Юрьевна Коптельцева – ведущий инженер-исследователь АО «КБП им. А.Г. Шипунова».
https://orcid.org/0000-0002-7736-0480
E-mail: olya_moshkina@mail.ru

Виталий Васильевич Автаев – ведущий инженер лаборатории прочности и надежности материалов воздушного судна НИЦ «Курчатовский институт» – ВИАМ.
https://orcid.org/0000-0001-6825-0602
E-mail: darkee@mail.ru

Nikolai O. Yakovlev – Cand. Sci. (Eng.), Head of the Laboratory of Strength and Reliability of Aircraft Materials, NRC “Kurchatov Institute” – VIAM.
https://orcid.org/0000-0002-3663-8239
E-mail: nick_62@mail.ru

Irina V. Gulina – Deputy Head of the Laboratory of Strength and Reliability of Aircraft Materials, NRC “Kurchatov Institute” – VIAM.
https://orcid.org/0000-0001-5934-2249.
E-mail: iragoolina@gmail.com

Николай Олегович Яковлев – к.т.н., начальник лаборатории прочности и надежности материалов воздушного судна НИЦ «Курчатовский институт» – ВИАМ.
https://orcid.org/0000-0002-3663-8239
E-mail: nick_62@mail.ru

Ирина Владимировна Гулина – заместитель начальника лаборатории прочности и надежности материалов воздушного судна НИЦ «Курчатовский институт» – ВИАМ.
https://orcid.org/0000-0001-5934-2249
E-mail: iragoolina@gmail.com

Contribution of the authors

A.D. Monakhov – conducted experiments, conducted the calculations, processed the research results, wrote the manuscript, analyzed the research results, formulated the conclusions of the article.

M.M. Gulyaev – prepared the experiment, formulated the main concept, defined the goal and objectives of the study, revised the manuscript, revised the conclusions, provided resources.

N.E. Gladysheva – prepared the experiment, formulated the main concept, defined the goal and objectives of the study, revised the manuscript, revised the conclusions, provided resources.

O.Yu. Kopteltseva – prepared the experiment, formulated the main concept, defined the goal and objectives of the study, revised the manuscript, revised the conclusions, provided resources

V.V. Avtaev – conducted calculations, processed the research results, revised the manuscript, managed the experiment, formulated the conclusions.

N.O. Yakovlev – scientific advising, formulated the main concept, revised the manuscript, revised the conclusions.

I.V. Gulina – conducted the calculations revised the manuscript, revised the conclusions, provided resources, managed the experiment.

Вклад авторов

А.Д. Монахов – проведение экспериментов, проведение расчетов, обработка результатов исследований, подготовка текста статьи, анализ результатов исследований, формулировка выводов статьи.

М.М. Гуляев – подготовка эксперимента, формирование основной концепции, постановка цели и задачи исследования, корректировка текста статьи, корректировка выводов статьи, обеспечение ресурсами.

Н.Е. Гладышева – подготовка эксперимента, формирование основной концепции, постановка цели и задачи исследования, корректировка текста статьи, корректировка выводов статьи, обеспечение ресурсами.

О.Ю. Коптельцева – подготовка эксперимента, формирование основной концепции, постановка цели и задачи исследования, корректировка текста статьи, корректировка выводов статьи, обеспечение ресурсами.

В.В. Автаев – проведение расчетов, обработка результатов исследований, корректировка текста статьи, руководство проведением эксперимента, формулировка выводов статьи.

Н.О. Яковлев – научное руководство, формирование основной концепции, корректировка текста статьи, корректировка выводов статьи.

И.В. Гулина – проведение расчетов, корректировка текста статьи, корректировка выводов статьи, руководство проведением эксперимента.

The article was submitted 28.12.2022, revised 20.04.2023, accepted for publication 24.04.2023

Статья поступила в редакцию 28.12.2022, доработана 20.04.2023, подписана в печать 24.04.2023